The Institute of Paper Chemistry

Appleton, Wisconsin

Doctor's Dissertation

An Investigation of Fiber Consistency Distributions in Turbulent Tube Flow

H. T. Sanders, Jr.

June, 1970

AN INVESTIGATION OF FIBER CONSISTENCY DISTRIBUTIONS IN TURBULENT TUBE FLOW

A thesis submitted by

H. T. Sanders, Jr.

B.S. 1965, North Carolina State University

M.S. 1967, Lawrence University

in partial fulfillment of the requirements
of The Institute of Paper Chemistry
for the degree of Doctor of Philosophy
from Lawrence University,
Appleton, Wisconsin

June, 1970

"Ideas won't keep, something must be done about them."

- Cooley.

TABLE OF CONTENTS

	Page
SUMMARY	1
INTRODUCTION AND LITERATURE	2
Flow of Fiber Suspensions	2
Laminar Plug Flow	3
Plug Turbulence	3
Damped Turbulence	3
Flow of Other Fluids and Suspensions	8
STATEMENT OF THE PROBLEM	11
ANALYSIS OF TWO-PHASE TURBULENT FLOW OF FIBER SUSPENSIONS	13
Equation for Consistency Distribution	20
Equation for Velocity Distribution	23
EXPERIMENTAL	29
Equipment — The Pipe Loop	29
Velocity Profile Measurements	33
Consistency Distribution Measurements	42
Annular-Purge Consistency Probe	42
Testing and Calibration of Consistency Probe	46
PROCEDURES	56
Fiber Properties	56
Pressure Losses	57
Velocity Profiles	57
Consistency Profiles	58
RESULTS AND DISCUSSION	59
Reynolds Number-Friction Factor Correlations	59
Velocity Profiles	59

Page

Consistency Profiles 70

SUMMARY OF RESULTS AND CONCLUSIONS 84

SUGGESTIONS FOR FUTURE WORK 88

NOMENCLATURE 89

ACKNOWLEDGMENTS 92

LITERATURE CITED 93

APPENDIX I. LIGHT SOURCE AND POWER SUPPLY 95

APPENDIX II. VELOCITY PROFILE DATA 98

APPENDIX III. CONSISTENCY PROFILE DATA 115

SUMMARY

An experimental investigation of dilute wood fiber suspensions (0.05 to 0.50%) in turbulent tube flow is described along with a mathematical description of suspension flow. The experimental investigation includes the measurement of time-mean velocity and consistency profiles in the damped turbulence and Newtonian flow regimes of fiber suspension flow. A special light-guide probe was developed for local consistency measurements in a flowing suspension. The mathematical description of fiber suspension flow is based on equations of continuity and motion which were developed for the case of two-phase flow. Equations which describe the consistency and velocity profiles were derived using Prandtl's mixing length concept and were found to be consistent with the experimental data.

The time-mean consistency distribution for turbulent suspensions was found to be strongly dependent on both the average consistency and flow rate. In general, the consistency increased from the wall to the center line of the pipe. The consistency distribution became more uniform with increasing flow rate and decreasing average consistency.

The velocity distributions indicated that the apparent von Karman constant is a function of both average consistency and flow rate. The apparent von Karman constant decreases with increasing consistency and increases with increasing flow rate. The velocity distributions approach the Newtonian line at very high flow rates.

The experimental investigation indicated some important factors in the proper design of experimental flow systems. Long, smooth-radius bends create stable secondary flow patterns which are undesirable for achieving fully developed velocity profiles. Sharp-angled entrances to a flow section allow rapid attainment of fully developed profiles.

INTRODUCTION AND LITERATURE

The study of the flow properties of fiber suspensions is interesting from both scientific and technological considerations. The practical significance of such studies is due to the fact that the flow characteristics of fiber suspensions and the state of dispersion of the fibers in suspension play important roles in almost every facet of pulp and paper manufacture. For a scientist, the flow of a fiber suspension is an interesting example of general two-phase flow in which the solid phase, because of its geometric shape, modifies the flow properties of the system to a large extent, even at very low concentrations.

FLOW OF FIBER SUSPENSIONS

Pipe flow of fiber suspensions has been widely investigated, and the data are quite extensive (1-19). A comprehensive review of the earlier literature has been presented by Daily and Bugliarello (11). Much of the work concerning fiber suspensions has dealt with laminar plug flow and the transition to turbulent plug flow, an area which has been recently reviewed by Wrist (20).

Probably the most extensive investigations of the flow characteristics of fiber suspensions have been carried out by the M.I.T. Hydrodynamic Laboratory under TAPPI sponsorship (11). The M.I.T. report contains a large number of friction factor-Reynolds number correlations for both synthetic and wood fibers. Attempts to measure velocity distributions using an impact probe with a wide, flat face to prevent clogging by fibers are also reported. Unfortunately, the velocity profiles are not believed to be quantitatively reliable because of fiber-probe interactions. The friction factor-Reynolds number correlations indicated the existence of two turbulent flow regimes as previously reported by Robertson and Mason (5) and Forgacs, et al. (6). The friction loss behavior

found by these investigators, which is typical for a large number of fiber suspensions, is shown in Fig. 1 illustrating three separate flow regimes:

LAMINAR PLUG FLOW

At low flow rates (AB, Fig. 1) a plug-flow region exists in which the core is a coherent plug of fiber networks, and the velocity gradient is confined to an essentially fiber-free water annulus near the wall. The water annulus thickness increases with flow rate and varies with fiber properties and consistency. In this flow regime, pressure losses in pipe flow are greater than for water flow at comparable flow rates.

PLUG TURBULENCE

At the transition point (B), flow in the water annulus becomes unstable and an increasingly turbulent water layer forms around the plug. Further increases in flow rate produce turbulent stresses in excess of the yield stress of the fiber networks, which cause progressive disintegration of the plug until it apparently disappears at (C). The pressure loss in pipe flow becomes less than for water flow in this flow regime.

DAMPED TURBULENCE

At velocities above the second transition (C), the flow is turbulent across the entire cross section except for the boundary layer, and the friction factor is practically constant over a considerable range of velocities. The degree to which the fiber suspensions deviate from Newtonian behavior and the flow rates at which the different flow regimes are encountered depend, for example, on the consistency, fiber properties, and pipe diameter. Wood pulp and nylon fiber suspensions behave in a similar manner in departing from Newtonian behavior (11,13,16). The departure from Newtonian behavior increases with increasing fiber length-to-diameter ratios, flexibility, and consistency (5,11,13,16).

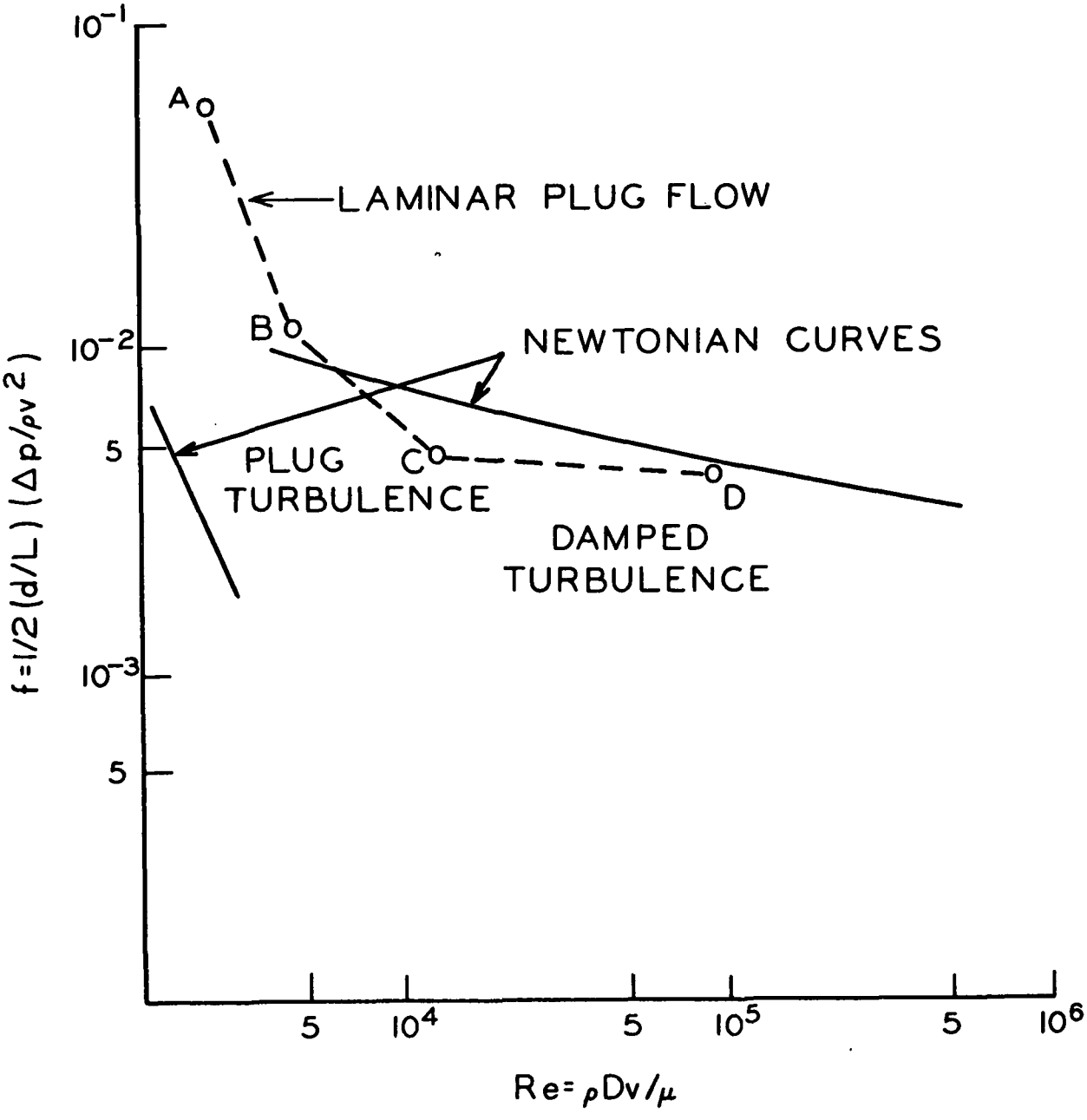

Figure 1. Typical Friction-Factor vs. Reynolds Number Curve for Fiber Suspensions

The non-Newtonian behavior becomes more distinct with increasing pipe diameter for a given suspension (4,11,16,18). The effect of the fiber properties and consistency on the flow properties of suspensions is thought to be related to the influence these variables have on the tendency of the suspension to form coherent networks (5,6,12). The lower head losses for turbulent flow of fiber suspensions as compared to water alone have been attributed to a modification of the turbulent momentum transfer mechanism by the fibers or fiber networks (1,5,21). This explanation has not been experimentally verified, however. Daily, et al. (22) attempted turbulence measurements using a wide, blunt-faced probe and reported a depression of the intensity of turbulence for fiber suspensions. However, the measurements are not thought to be quantitatively reliable because of particle-probe interactions. Bobkowicz and Gauvin (13,14) have reported turbulence measurements based on a dispersion technique. They reported an increase in eddy diffusivity, radial turbulence intensity, and Lagrangian length scale for fiber suspensions as compared to water. These results appear to be inconsistent with the generally accepted belief that the fibers damp turbulence. Possible reasons for this apparent discrepancy may be that, at the flow rate and consistencies reported for this investigation, the flow was not fully turbulent and that there may have been particle interference with the sensing probe. Robertson and Mason (5) have measured the flocculation or degree of heterogeneity of flowing suspensions using an optical transmission technique. The flocculation measurements varied with flow rate and showed transitions in heterogeneity which were in close agreement with the observed transitions in the friction factor data. This was taken as evidence that there are real changes in the suspension structure with changes in flow rate. Although these measurements were macroscopic averages across a pipe diameter, they do indicate that the degree of dispersion of the fibers in suspension is related to the hydrodynamic behavior of the suspension.

More recently, Mih and Parker (16) have described a special impact probe for measuring local velocities in fiber suspensions and presented velocity profiles for turbulent fiber suspensions. These profiles provide conclusive evidence that at low turbulent flow rates a central plug flow region is present. The diameter of the plug decreases with increasing velocity and increases with increasing consistency. Presumably, the existence of the plug in pipe flow is a consequence of the fiber suspension having a finite yield stress (4-6,10,12). Calculations of the shear stress at the plug boundary for various fiber suspensions did indicate a correlation with the inherent network strength of the suspension. Mih and Parker also found that the shear stress at the plug surface increases with increasing velocity and decreasing plug radius. The reason for this behavior was not known, but it was suggested that a concentration gradient might exist in suspension pipe flows. This possibility has been suggested previously (1,23). The turbulent shear portions of these velocity profiles obeyed a logarithmic distribution law as do the velocity profiles for turbulent Newtonian fluids. For Newtonian flow of fluids, turbulent velocity profiles can be correlated by Prandtl's logarithmic distribution law as follows (24):

$$v^+ = \frac{1}{\kappa} \ln s^+ + B \qquad (1)$$

where

$$v^+ = \bar{v}/\sqrt{\tau_o/\rho}$$

$$s^+ = s\rho\sqrt{\tau_o/\rho} \; / \; \mu$$

in which the slope, $1/\kappa$, and the intercept, B, are constant for all Newtonian fluids[a]. The reciprocal of this slope is the well-known von Karman constant.

---

[a]Definitions of all symbols may be found in the Nomenclature Section.

Mih and Parker found that the apparent von Karman constant for fiber suspensions was lower than for Newtonian fluids and varied with fiber type and concentration, but was independent of flow velocity. The apparent von Karman constant was assumed to be characteristic of the suspension in turbulent flow. Mih and Parker developed a phenomenological description of turbulent fiber suspension flow based on the supposition that turbulent fiber suspension flow is analogous to the turbulent flow of Newtonian fluids in rough pipes. This analogy was based on their observations that both the friction factor and velocity profiles for fiber suspensions were very nearly constant at high flow rates, and that the same is true of Newtonian flow in rough pipes. However, there appear to be several anomalies in this analogy. The pressure loss behavior of the two systems deviates in opposite directions from the Newtonian curve for smooth pipes. Also, Seely (18) has reported that velocity profiles in turbulent suspension flow are not independent of flow rate and in fact vary in a systematic manner with increasing flow rate.

One of the most recent investigations of the turbulent flow of fiber suspensions was that of Seely (18). He measured velocity profiles using the annular-purge impact probe described by Mih and Parker (16). A number of friction factor-Reynolds number correlations were also presented. Seely found that at high flow rates depending on consistency the friction loss behavior of fiber suspensions approached and followed Newtonian behavior. This type of behavior had been suggested previously (11) but had not been experimentally verified. This flow regime was termed Newtonian turbulence to differentiate it from the two previously noted turbulent flow regimes. He also noted that the velocity profiles in the Newtonian turbulent flow regime coincided with those for water flow, further supporting the concept of a Newtonian flow regime for fiber suspensions

at high flow rates. The velocity profiles at the lower flow rates, when correlated according to the familiar logarithmic distribution law, indicated that the apparent von Karman constant was lower for fiber suspensions than for water, as observed by Mih and Parker. However, as mentioned previously, Seely found that the apparent von Karman constant increased in a systematic manner throughout the damped turbulent regime and approached the Newtonian value at very high flow rates. The reason for the discrepancy between these two investigations concerning the effect of flow rate on the velocity profiles is not obvious at this time.

FLOW OF OTHER FLUIDS AND SUSPENSIONS

It is interesting to note that certain polymer solutions exhibit some similarities to the flow of fiber suspensions. Dilute solutions of long-chained, linear polymers also show a depressed friction loss behavior in turbulent flow (25-30). In spite of this similarity, polymer flow is basically different from fiber suspension flow in several important respects. These polymer solutions are single-phase systems and do not exhibit plug flow at any flow rate. In fact, many of the polymer solutions which show depressed pressure drops in turbulent flow behave in a Newtonian manner at laminar flow rates (25). Fiber suspensions, on the other hand, are characterized by the presence of two distinct phases: one phase consisting of solid fibers which have dimensions much greater than the molecular dimensions of the suspending medium. Perhaps the similar behavior of certain dilute polymer solutions in turbulent flow is due to the presence of a molecular species which is much larger than the solvent. Virk, et al. (25) have suggested that these large polymer chains damp turbulence in much the same manner as long fibers damp turbulence in suspension flow.

There are reports of certain other slurries which suppress the momentum transfer properties in turbulent flow (31,32). Thomas (31) has shown that water slurries of kaolin, titanium dioxide, and thorium oxide also depress the friction loss below the Newtonian value. This suppression was intuitively attributed to a damping of the turbulence by the suspended solids and appeared to be related to the ability of the solids to form flocs which could support a yield stress. Kaolin-water suspensions are characterized by a lower apparent von Karman constant for turbulent flow (32). These features appear to be quite similar to those of fiber suspensions in the damped turbulence flow regime. However, these slurries could be described by a Bingham plastic model in laminar flow. This observation is contrary to fiber suspension flow in pipes.

The effect of solid particles in turbulent suspension flow is dependent on the particle characteristics. For instance, Daily and Roberts (33) have found that dilute suspensions of neutrally buoyant rigid spheres have a friction loss which is greater than water. The friction factor increased with increasing concentration and decreasing particle size. All of this behavior is contrary to the behavior of fiber suspensions. They also found that the velocity profiles were sharper than those of water for small-diameter particles and fuller than those of water for larger particle diameters. The velocity profiles for the larger particles are questionable, however, because of apparent particle-probe interactions. Bobkowicz and Gauvin (13,14) have found that fiber suspension behavior is highly dependent on the fiber length-to-diameter ratio. For low values of this ratio, the pressure drop behavior was essentially Newtonian. Hino (34) has presented a theory for two-phase flow based on energy and inertial considerations for turbulent flow of suspensions. Equations relating various statistical turbulence parameters and the von Karman constant to concentration, sediment velocity, and

specific weight gave reasonable agreement with data for suspensions of rigid particles. The theory predicts that the von Karman constant decreases with increasing concentration of solid particles for all suspensions. The theory apparently does not account for the higher friction factor and the fuller velocity profiles for some suspensions of spherical particles reported by Daily and Roberts (33). This theory appears to be readily applicable only to suspensions of rigid, spherical particles.

STATEMENT OF THE PROBLEM

From the discussion in the previous section, it is evident that fibers significantly alter the momentum transport properties in suspension pipe flow. Also, the nature of fiber-suspension flow appears to have some unique features, although other slurries or solutions have some behavior in common with suspension flow.

The flow of fiber suspensions cannot be represented by modified Newtonian or non-Newtonian equations which are applicable to single-phase systems or homogeneous suspensions. Past attempts to use these types of correlations have failed to explain fiber suspension behavior because fiber suspensions are two-phase systems and are capable of phase segregation. Therefore, momentum is transferred by both fiber and water phases and may vary depending on the distribution and behavior of the fiber phase. The properties of fiber suspensions which differentiate their behavior from most other suspensions [such as those of spherical particles (33)] appear to be related to the ability of fibers to form a "network structure."

The flow of fiber suspensions in the laminar plug flow and turbulent plug flow regimes has been recognized as a two-phase system by previous investigators (5,6,10-12,16,18,19) and has been described using a peripheral annulus model. This model is still incomplete, and fiber suspensions in fully developed turbulent flow have not been analyzed at all. The flow behavior has simply been observed and the data correlated using techniques for Newtonian fluids.

The application of single-phase Newtonian or non-Newtonian approaches to turbulent suspension flow is not likely to provide an adequate description of

suspension behavior. It is believed that a knowledge of the coupled behavior of the water and the solid fiber phases is necessary in order to develop a quantitative understanding of turbulent suspension flow.

This investigation approaches the problem of describing turbulent, fiber-suspension flow by treating suspension flow as a two-phase system. Equations which describe the time-mean consistency and velocity distributions are derived from the basic equations of continuity and motion considering the effect of each phase on the other. These equations were developed for the case of fully developed turbulent pipe flow of dilute suspensions. Consistency and velocity profiles are measured in an experimental pipe loop over a range of consistencies and flow rates. A new experimental technique for consistency measurements was developed and allows the measurement of local average consistencies for the first time. Some of the theoretical equations are solved and compared with the experimental results. An important aspect of this investigation is that it emphasizes the necessity of treating suspension flow as a two-phase system. Also, the experimental techniques developed in this study might be extended to other suspensions and flow systems, especially with regard to the investigation of the time-dependent behavior of suspended particles or conglomerates.

ANALYSIS OF TWO-PHASE TURBULENT FLOW OF FIBER SUSPENSIONS

The flow of fiber suspensions is treated on the basis of a two-phase system. The equations of continuity and motion for two-phase turbulent flow are derived with the basic assumption that both water and fibers can be treated as quasi continua and that, in general, the fibers and water move at different velocities. The drag forces between the two phases are assumed to be purely viscous in nature and are described in terms of Darcy's equation. The time-smoothed equations of continuity and motion are then simplified for the case of steady-state, two-dimensional channel flow. These equations are solved using Prandtl's mixing length concept to obtain equations which describe the consistency and velocity distributions for fiber suspension flow.

Fluid flow is governed by the laws of conservation of mass and momentum and is usually represented in the form of the equations of continuity,

$$\frac{\partial \rho}{\partial t} + \frac{\partial \rho v_i}{\partial x_i} = 0 \qquad (2),$$

and motion,

$$\frac{\partial \rho v_i}{\partial t} + \frac{\partial \rho v_i v_j}{\partial x_j} = -\frac{\partial p}{\partial x_i} - \frac{\partial \tau_{ij}}{\partial x_j} + F_i \qquad (3).$$

For convenience, the equations are written in tensor form using Cartesian coordinates: i, j = 1, 2, 3; and the summation convention applies. Equations (2) and (3) are completely general and accurate whenever the fluid is a continuum.

For a fiber suspension, neither the water nor the fiber phase is continuous. However, by defining a volume element of the suspension of such dimensions that many fibers are present but still very small compared with the dimensions of the

channel, the water and fibers may each be treated as quasi continua and equations similar to (2) and (3) apply approximately to each phase.

The true densities, $\rho_{\underline{W}}$ and $\rho_{\underline{F}}$, of the water and fibers, respectively, are related to their apparent densities in the mixture by

$$\rho_W \varepsilon = \rho_w \tag{4}$$

and

$$\rho_F (1-\varepsilon) = \rho_f \tag{5}$$

where ε is the fraction of the volume element occupied by water. The true density of the mixture is given by

$$\rho = \rho_w + \rho_f \tag{6}.$$

Allowing that the velocities of the two phases will, in general, be different, the continuity equations for the two phases may be expressed as follows:

$$\frac{\partial \varepsilon}{\partial t} + \frac{\partial \varepsilon \, v_{wi}}{\partial x_i} = 0 \tag{7}$$

and

$$-\frac{\partial \varepsilon}{\partial t} + \frac{\partial (1-\varepsilon) \, v_{fi}}{\partial x_i} = 0 \tag{8}.$$

Incompressible flow has been assumed; hence $\rho_{\underline{F}}$ and $\rho_{\underline{W}}$ are constant and drop out of the equations. The velocity components, $v_{\underline{wi}}$ and $v_{\underline{fi}}$, are the true average velocities of the water and fiber phases within the volume element.

Similarly, the equations of motion may be set up for their apparent masses and forces in the volume element. Expressions analogous to Equations (4) and (5)

also hold for apparent pressures, $\underline{p_w}$ and $\underline{p_f}$, and stresses, $\underline{\tau_{wij}}$ and $\underline{\tau_{fij}}$.

The body force is defined as the force of the water on the fibers, i.e., as

$$F_i = F_{wi} \tag{9}.$$

The force of gravity is accounted for separately so that the equations of motion for the suspension may be written in the following form:

$$\rho_W \left(\frac{\partial \varepsilon v_{wi}}{\partial t} + \frac{\partial \varepsilon v_{wi} v_{wj}}{\partial x_j} \right) = -\frac{\partial p_w}{\partial x_i} - \frac{\partial \tau_{wij}}{\partial x_j} + \rho_w \varepsilon g_i - F_i \tag{10}$$

$$\rho_F \left(\frac{\partial (1-\varepsilon) v_{fi}}{\partial t} + \frac{\partial (1-\varepsilon) v_{fi} v_{fj}}{\partial x_j} \right) = -\frac{\partial p_f}{\partial x_i} - \frac{\partial \tau_{fij}}{\partial x_j} + \rho_F (1-\varepsilon) g_i + F_i \tag{11}.$$

As defined by these equations, the forces available for the acceleration of the water phase are reduced by the amount $\underline{F_i}$ used to contribute to the acceleration of the fiber phase. The body forces may now be further defined. In general, the water provides a buoyancy force, $-\underline{\rho_W}(1-\varepsilon)\underline{g_i}$. A term is also needed which accounts for forces arising from relative flow between the fibers and water. As a simple case which can be mathematically treated, it will be assumed that the relative flow between phases is in the range of the Darcy equation. The viscous drag between the phases therefore becomes $\underline{\mu a \varepsilon}(\underline{v_{wi}} - \underline{v_{wf}})$, where $\underline{a}$ is the reciprocal of the permeability. When the above buoyancy force is corrected for the absence of pressure forces on cut fiber ends the body force is defined as

$$F_i = -\rho_W (1-\varepsilon) g_i + \mu a \varepsilon (v_{wi} - v_{fi}) + \frac{\partial \left[(1-\varepsilon) p_w \right]}{\partial x_i} \tag{12}.$$

Equations (7), (8), (10), and (11) represent the equations of continuity and motion for two-phase, incompressible flow. The only deviations from rigorous

treatment have been the formulation of the drag term between the phases. This force has been assumed to be purely viscous in nature, for convenience.

The description of turbulent flow in terms of continuity and momentum requires allowance for variations of all quantities in terms of space and time coordinates. The solution of these equations is considered an almost impossible task even for Newtonian fluids. Therefore, in past investigations of steady-state turbulent flow, the time-smoothed equations of continuity and motion have provided the additional Reynolds stresses and thus the basis for classical engineering approaches such as Prandtl's mixing length concept (24,35).

The time-smoothed form of the equations of motion and continuity for suspension flow will be developed. The resulting equations will then be reduced for the case of steady-state, two-dimensional flow. The instantaneous variables are replaced by the sum of a space-dependent, time-averaged quantity and a space- and time-dependent fluctuation as follows:

$$
\begin{aligned}
v_{wi} &= \bar{v}_{wi} + v'_{wi} \\
v_{fi} &= \bar{v}_{fi} + v'_{fi} \\
p_W &= \bar{p}_W + p'_W \\
p_f &= \bar{p}_f + p'_f \\
\varepsilon &= \bar{\varepsilon} + \varepsilon'
\end{aligned}
\qquad (13)
$$

where the bar represents the time-mean value and the prime a time-dependent fluctuation.

The continuity equations, (7) and (8), after time smoothing, become:

$$\frac{\partial \bar{\varepsilon}}{\partial t} + \frac{\partial\left(\bar{\varepsilon}\bar{v}_{wi} + \underline{\overline{\varepsilon' v'_{wi}}}\right)}{\partial x_i} = 0 \tag{14}$$

$$-\frac{\partial \bar{\varepsilon}}{\partial t} + \frac{\partial\left[(1-\bar{\varepsilon})\bar{v}_{fi} - \underline{\overline{\varepsilon' v'_{fi}}}\right]}{\partial x_i} = 0 \tag{15}.$$

A similar operation transforms the equations of motion, (10) and (11), into

$$\rho_W \left\{\frac{\partial}{\partial t}\left(\bar{\varepsilon}\bar{v}_{wi} + \underline{\overline{\varepsilon' v'_{wi}}}\right) + \frac{\partial}{\partial x_j}\left[\bar{\varepsilon}\left(\bar{v}_{wi}\bar{v}_{wj} + \underline{\overline{v'_{wi} v'_{wj}}}\right)\right.\right.$$

$$\left.\left. + \underline{\bar{v}_{wi}\overline{v'_{wj}\varepsilon'}} + \underline{\bar{v}_{wj}\overline{v'_{wi}\varepsilon'}}\right]\right\}$$

$$= -\frac{\partial \bar{p}_w}{\partial x_i} - \frac{\partial \bar{\tau}_{wij}}{\partial x_j} + \bar{\rho}_w \bar{\varepsilon} g_i - \bar{F}_i \tag{16}$$

$$\rho_F \left\{\frac{\partial}{\partial t}\left[(1-\bar{\varepsilon})\bar{v}_{fi} - \underline{\overline{\varepsilon' v'_{fi}}}\right] + \frac{\partial}{\partial x_j}\left[(1-\bar{\varepsilon})\left(\bar{v}_{fi}\bar{v}_{fj} + \underline{\overline{v'_{fi} v'_{fj}}}\right)\right.\right.$$

$$\left.\left. - \underline{\bar{v}_{fi}\overline{v'_{fj}\varepsilon'}} - \underline{\bar{v}_{fj}\overline{v'_{fi}\varepsilon'}}\right]\right\}$$

$$= -\frac{\partial \bar{p}_f}{\partial x_i} - \frac{\partial \bar{\tau}_{fij}}{\partial x_j} + \bar{\rho}_F(1-\bar{\varepsilon})g_i + \bar{F}_i \tag{17}.$$

The underlined terms evolve in the time-smoothing process and are generally referred to as the Reynolds stresses. For the case of steady-state, incompressible flow in a flat channel, the equations may be reduced using the coordinate system shown in Fig. 2.

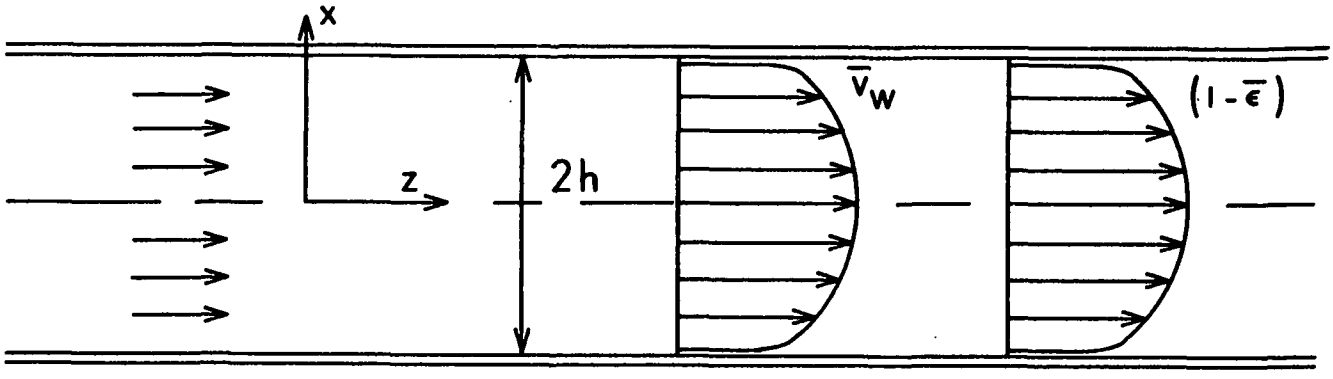

Figure 2. Coordinate System for Flow in a Flat Channel

Equations (14) and (15) may now be written as

$$\frac{\partial \overline{\epsilon' v'}_{wx}}{\partial x} = 0 \qquad (18)$$

$$-\frac{\partial \overline{\epsilon' v'}_{fx}}{\partial x} = 0 \qquad (19).$$

Note that there is no flow in the x-direction and no change of flow conditions in the z-direction. Therefore,

$$\bar{v}_{wx} = \bar{v}_{fx} = \frac{\partial \bar{v}_{wz}}{\partial z} = \frac{\partial \bar{v}_{fz}}{\partial z} = \frac{\partial \bar{\epsilon}}{\partial z} = 0 \qquad (20).$$

The equations of motion, (16) and (17), can be reduced into a more manageable form by making a few additional assumptions. It is assumed: (1) that the pressure, p, includes the gravity term, ρg_i [so that the pressure term is in the form of actual measurements, i.e., a pressure difference]; (2) that the suspension is in a state of buoyancy so that the term $(\rho-\rho_w)g_i$ vanishes; (3) that the Reynolds stresses exceed the yield stresses (tensile and shear) of network structures. Therefore,

$\tau_{\underline{fij}} = 0$. With these simplifications and making use of Equation (20), the equations of motion reduce to the following form:

$$\rho_W \frac{\partial}{\partial x}\left(\bar{\varepsilon}\overline{v'_{wz}v'_{wx}} + \bar{v}_{wz}\overline{v'_{wx}\varepsilon'}\right)$$

$$= -\frac{\partial \bar{p}_w}{\partial z} - \frac{\partial \bar{\tau}_{wxz}}{\partial x} - \bar{D}_z \tag{21}$$

$$\rho_W \frac{\partial}{\partial x}\left(\bar{\varepsilon}\overline{v'^2_{wx}}\right) = -\frac{\partial \bar{p}_w}{\partial x} - \bar{D}_x \tag{22}$$

$$\rho_F \frac{\partial}{\partial x}\left[(1-\bar{\varepsilon})\overline{v'_{fz}v'_{fx}} - \bar{v}_{fz}\overline{v'_{fx}\varepsilon'}\right] = \bar{D}_z \tag{23}$$

where $d(\underline{p}-\underline{p_w})/d\underline{z} = 0$.

$$\rho_F \frac{\partial}{\partial x}\left[(1-\bar{\varepsilon})\overline{v'^2_{fx}}\right] = -\frac{\partial\left(\bar{p}-\bar{p}_w\right)}{\partial x} + \bar{D}_x \tag{24}$$

The viscous drag term, $\underline{D_i}$, is retained in the time-smoothed form to provide for a time-mean effect of viscous damping on the mean turbulent motion.

$$D_i = \mu\bar{a}\bar{\varepsilon}\left(\overline{v_{wi}-v_{fi}}\right) = \mu\bar{a}\bar{\varepsilon}\bar{v}_{ri} \tag{25}$$

Equations (21) through (24) are significantly different from the equations of motion for Newtonian fluids because of the drag term, $\underline{D_i}$, and because of the additional Reynolds stresses arising from the mass exchange terms. However, they reduce to the Newtonian form of the equations if the time-mean relative velocities, $\underline{v_{ri}}$, between the phases and the solid fraction exchange terms, $\overline{\varepsilon'\underline{v'_{wx}}}$, vanish.

In order to make the time-smoothed equations of continuity and motion useful, it is necessary to express the Reynolds stresses and mass exchange in terms of the time-mean fluid velocity and solids concentration. Therefore, Prandtl's mixing length concept has been extended to include two-phase suspension flow in order to gain some insight into the fiber and velocity distributions.

EQUATION FOR CONSISTENCY DISTRIBUTION

An expression for the consistency distribution may be derived from the equation of continuity for the water phase, Equation (18). Integrating this equation yields:

$$\overline{\varepsilon' v'_{wz}} = C_w \qquad (26a).$$

This equation indicates that the correlation between the fluctuations in solid fraction, ε', and the fluctuations in velocity, $\underline{v'}_{\underline{wx}}$, are constant across the channel. Introducing Prandtl's mixing length concept for the solid fraction exchange term:

$$l_\varepsilon l_w \frac{d\bar{\varepsilon}}{dx} \frac{d\bar{v}_{wz}}{dx} = -C_w \qquad (26b)$$

where $\underline{l}_{\underline{\varepsilon}}$ and $\underline{l}_{\underline{w}}$ are the mixing lengths for the solid fraction exchange and water velocity distributions, respectively, and where the negative sign anticipates the solid fraction gradient being negative. Equation (26b) expresses the fluctuating quantities in terms of their respective mixing lengths and gradients across the channel. Since the solid fraction exchange term, $\overline{\varepsilon' \underline{v'}_{\underline{wz}}}$, is constant across the channel, a change in the velocity gradient will be accompanied by a change

in the consistency gradient, thus giving rise to a consistency distribution which is dependent on the velocity distribution. However, the velocity of the water phase should be expressed in terms of the superficial water velocity, $\bar{V}_{wz} = \bar{\varepsilon}\bar{v}_{wz}$, since the superficial velocity is the quantity actually measured with an impact probe. The velocity gradient then becomes

$$\frac{d\bar{v}_{wz}}{dx} = \frac{1}{\bar{\varepsilon}} \frac{d\bar{V}_{wz}}{dx} - \frac{\bar{V}_{wz}}{\bar{\varepsilon}^2} \frac{d\bar{\varepsilon}}{dx} \tag{27}.$$

Also, it is assumed that in the neighborhood of the wall the mixing length is proportional to the wall distance, $s = h-x$,

$$l_\varepsilon = \kappa_\varepsilon s$$

$$l_w = \kappa_w s \tag{28}.$$

Equation (26) may then be represented as follows:

$$\frac{d\bar{\varepsilon}}{\bar{\varepsilon}} = \frac{C_w}{\kappa_\varepsilon \kappa_w} \frac{ds}{s^2 \left(d\bar{V}_{wz}/ds\right)} \tag{29}$$

where for mathematical convenience the term $V_{wz}/\bar{\varepsilon}^2 d\bar{\varepsilon}/ds$ has been assumed small compared to the velocity gradient, $(1/\bar{\varepsilon})d\bar{V}_{wz}/ds$. The significance of this assumption will become clear in the discussion of results. Introducing the friction velocity, $v_* = \sqrt{\tau_o/\rho}$, a nondimensional water velocity, $\left(\bar{v}^+\right) = V_{wz}/v_*$, and a nondimensional position parameter, $s^+ = s\rho v_*/\mu$, Equation (29) reduces to a form which may be easily integrated:

$$\frac{d\bar{\varepsilon}}{\bar{\varepsilon}} = -\frac{C_w}{\kappa_\varepsilon \kappa_w} \frac{1}{v_*} \frac{1}{dv^+/dlns^+} \frac{ds}{s} \tag{30}.$$

Inspection of this equation reveals that the term $d\underline{v}^+/d \ln \underline{s}^+$ is the differential form of the familiar logarithmic velocity distribution law. Seely (18) has shown that fully turbulent fiber suspensions fit the logarithmic velocity distribution law, but that the apparent von Karman constant is a function of the average flow velocity and the average consistency of the suspension. For a given suspension and flow velocity, the velocity profile can be represented as

$$\frac{dv^+}{d\ln s^+} = \frac{1}{\kappa_*} \tag{31}$$

where κ_* is the apparent von Karman constant for the turbulent suspension. Introducing Equation (31) into Equation (30) and integrating over the entire channel,

$$\ln \frac{\bar{\varepsilon}}{\bar{\varepsilon}_o} = - \frac{C_w}{\kappa_\varepsilon \kappa_w} \frac{\kappa_*}{v_*} \left(\ln s - \ln s_o\right) \tag{32}.$$

Solving for the solid fraction,

$$\ln\left(\frac{1-\bar{c}}{1-\bar{c}_o}\right) = - \frac{C_w}{\kappa_\varepsilon \kappa_w} \frac{\kappa_*}{v_*} \left(\ln s - \ln s_o\right) \tag{33}.$$

Note that the mixing length distributions (28) have been extended to the entire turbulent core of the suspension. The distance $\underline{s}_o$ is assumed to be of the order of magnitude of the thickness of the laminar sublayer. $\underline{c}_o$ is the volume fraction of fibers at the boundary layer, $\underline{s}_o$.

Equation (33) cannot be utilized without a knowledge of the velocity distribution and the constant $\underline{C}_w/\kappa_\varepsilon \underline{\kappa}_w$. The volume fraction of the fibers at the boundary layer is needed also. However, it is interesting to note that the solid fraction distribution is a function of the velocity distribution, as denoted

by the apparent von Karman constant, κ_*. Also, the equation predicts a logarithmic distribution for the solid fraction. Therefore, the solid fraction distribution should change significantly with changes in the velocity distribution.

EQUATION FOR VELOCITY DISTRIBUTION

The equations of motion can be solved in a similar manner as above in order to describe the velocity distribution of fiber suspensions. The equations of motion for the z-direction, Equations (21) and (23), contain expressions for the unknown velocities $\overline{\underline{v}_{\underline{\underline{wz}}}}$ and $\overline{\underline{v}_{\underline{\underline{fz}}}}$. By considering only the turbulent core of the suspension, the term for viscous friction will be insignificant. Equations (21) and (23) then reduce to

$$\rho_W \frac{\partial}{\partial x}\left(\overline{\bar{\varepsilon} v'_{wz} v'_{wx}} + \bar{v}_{wz}\overline{\varepsilon' v'_{wx}}\right) = -\frac{\partial \bar{p}_W}{\partial z} - \bar{D}_z \tag{34}$$

$$\rho_F \frac{\partial}{\partial x}\left[(1-\bar{\varepsilon})\overline{v'_{fz} v'_{fx}} - v_{fz}\overline{\varepsilon' v'_{fx}}\right] = \bar{D}_z \tag{35}.$$

Introducing the mixing length concept in a similar fashion as was done in Equation (27), the Reynolds stresses may be expressed in the following form:

$$\overline{\bar{\varepsilon} v'_{wz} v'_{wx}} = l_w^2 \frac{1}{\bar{\varepsilon}}\left|\frac{d\bar{V}_w}{dx}\right| \frac{d\bar{V}_w}{dx} \tag{36a}.$$

$$(1-\bar{\varepsilon})\overline{v'_{fz} v'_{fx}} = l_f^2 \frac{1}{1-\bar{\varepsilon}}\left|\frac{d\bar{V}_f}{dx}\right| \frac{d\bar{V}_f}{dx} \tag{36b}$$

$$\overline{\varepsilon' v'_{fx}} = l_\varepsilon l_f \frac{1}{1-\bar{\varepsilon}} \frac{d\bar{\varepsilon}}{dx} \frac{d\bar{V}_f}{dx} = -C_f \tag{36c}$$

Again, the mixing lengths are assumed proportional to the distance from the wall,

$$l_\varepsilon = \kappa_\varepsilon s \tag{37a}$$

$$l_w = \kappa_w s \tag{37b}$$

$$l_f = \kappa_f s \tag{37c}.$$

Substituting these expressions into Equations (34) and (35) and making the assumption used in Equation (30) yields

$$\rho_W \frac{\partial}{\partial x}\left(l_w^2 \frac{1}{\bar{\varepsilon}}\left|\frac{d\bar{V}_w}{dx}\right|^2 - \frac{C_w \bar{V}_w}{\bar{\varepsilon}}\right) = -\frac{\partial p_w}{\partial z} - \mu \bar{a} \bar{\varepsilon} \bar{v}_{rz} \tag{38}$$

$$\rho_F \frac{\partial}{\partial x}\left(l_f^2 \frac{1}{1-\bar{\varepsilon}}\left|\frac{d\bar{V}_f}{dx}\right|^2 + \frac{C_f \bar{V}_f}{1-\bar{\varepsilon}}\right) = \mu \bar{a} \bar{\varepsilon} \bar{v}_r \tag{39}$$

where $\overline{\underline{v}_{rz}}$ is the relative velocity between the water and fiber phases. These equations in conjunction with the equations of continuity can, in principle, be solved for $\bar{\underline{V}}_w$, $\bar{\underline{V}}_f$, and $\bar{\varepsilon}$. The solution of these equations would be a difficult problem requiring numerical treatment which, however, cannot be attempted without a knowledge of several constants and boundary conditions.

However, a useful expression for the velocity distribution of the suspension can be obtained by making some rather far-reaching assumptions. The treatment is similar to that used by Prandtl in developing the velocity distribution for Newtonian fluids (24).

In general, the viscous drag term will depend upon the position in the channel and may be written as

$$\mu\bar{a}\bar{\varepsilon}\bar{v}_{rz} = \mu \frac{\partial}{\partial x} \int_o^x \bar{\varepsilon}\bar{a}\bar{v}_{rz} dx \qquad (40).$$

Introducing this expression into the equation of motion for the water phase yields

$$\rho_W \frac{\partial}{\partial x} \left(l_w^2 \frac{1}{\bar{\varepsilon}} \left| \frac{d\bar{V}_w}{dx} \right|^2 - \frac{C_w \bar{V}_w}{\bar{\varepsilon}} + \mu \int_o^x \bar{\varepsilon}\bar{a}\bar{v}_{rz} dx \right) = -\frac{\partial p_w}{\partial z} \qquad (41)$$

or, since $\partial \underline{p}/\partial \underline{z} = -\partial\tau/\partial \underline{x}$,

$$\rho_W \frac{\partial}{\partial x} \left(l_w^2 \frac{1}{\bar{\varepsilon}} \left| \frac{d\bar{V}_w}{dx} \right|^2 - \frac{C_w \bar{V}_w}{\bar{\varepsilon}} + \mu \int_o^x \bar{\varepsilon}\bar{a}\bar{v}_{rz} dx \right) = \frac{\partial \tau}{\partial x} \qquad (42).$$

After introduction of Equation (37b) and the wall distance, $\underline{s} = \underline{h}-\underline{x}$, this equation may be integrated to give

$$\rho_W \frac{\kappa^2 s^2}{\bar{\varepsilon}} \left(\frac{d\bar{V}_w}{ds} \right)^2 = \tau_o \frac{h-s}{h} + \frac{C_w \bar{V}_w \rho_w}{\bar{\varepsilon}} - \mu \int_s^h \bar{\varepsilon}\bar{a}\bar{v}_{rz} ds \qquad (43).$$

At this point, it is convenient to introduce Prandtl's assumption (24) that the shear stress remains constant, i.e., that $\tau = \tau_o$, where τ_o is the shear stress at the wall. In addition, the integral mean value is substituted for the viscous drag term. Equation (43) then reduces to

$$\left(\frac{d\bar{V}_w}{ds} \right)^2 = \frac{\bar{\varepsilon}}{\kappa^2 s^2} \left(\frac{\tau_o}{\rho_W} + \frac{C_w \bar{V}_w}{\bar{\varepsilon}} - \frac{\mu \bar{a} \bar{\varepsilon} \bar{v}_{rz} h}{\rho_W} \right) \qquad (44).$$

In spite of the fact that Equation (44) is valid only in the neighborhood of the wall, because of the assumption that τ = constant, we will attempt to use it, in Prandtl's fashion, for the whole channel. Introducing the friction velocity, $\underline{v}_* = \sqrt{\tau_o/\rho}$, and the nondimensional velocity, $\bar{v}^+ = \bar{V}_w/\underline{v}_*$, and position,

$\underline{s}^+ = \underline{s}\rho\underline{v}_*/\mu$, yields the following expression for the velocity distribution of the suspension:

$$\frac{dv^+}{d\ln s^+} = \frac{\sqrt{\bar{\varepsilon}}}{\kappa}\sqrt{1 + \frac{C_w v^+}{\bar{\varepsilon} v_*} - \frac{\mu a \overline{\varepsilon v_{rz}} h}{\rho v_*^2}} = \frac{1}{\kappa_*} \qquad (45).$$

Equation (45) predicts a logarithmic velocity distribution for turbulent fiber suspensions. Also, it predicts an apparent von Karman constant for suspensions which is different from the von Karman constant for Newtonian fluids. These observations are in agreement with Seely's results for dilute fiber suspensions (18). He found that turbulent fiber suspensions fit a logarithmic distribution law, but that the apparent von Karman constant is a function of the average flow rate and consistency for a given fiber type and pipe diameter. A closer inspection of Equation (45) indicates that the second term under the radical predicts that the slope increases with the nondimensional velocity. Seely, however, found that slope was fairly constant over the turbulent core. It is, therefore, assumed that the constant C_w is small so that the second term can be neglected. Equation (45) then reduces to

$$\frac{dv^+}{d\ln s^+} = \frac{\sqrt{\bar{\varepsilon}}}{\kappa}\sqrt{1 - \frac{\mu a \overline{\varepsilon v_{rz}} h}{\rho v_*^2}} = \frac{1}{\kappa_*} \qquad (46).$$

The term $\overline{\varepsilon a v_{rz}}$ would be expected to depend strongly on consistency because of the known behavior of the specific resistance coefficient, $\bar{a}$, but only mildly on the flow velocity. Then, according to Equation (46), the apparent von Karman constant, κ_*, would decrease with increasing friction velocity, v_*; just the opposite has been observed by Seely (18). Agreement with experimental evidence is restored if the relative velocity, $\overline{v_{rz}}$, is taken as negative. This

is equivalent to stating that the fiber velocity is greater than the water velocity. Equation (46) then appears to be in at least qualitative agreement with Seely's observations that the apparent von Karman constant decreases with increasing consistency and increases with increasing flow rate. It also appears to account for a channel size effect which has been reported by previous investigators (16,18).

The preceding mathematical treatment for fiber suspension flow was developed in Cartesian coordinates for two-dimensional flow. However, the experimental work of this investigation was performed in a pipe loop. Although cylindrical coordinates are the most appropriate for pipe flow, it may be easily shown that the previously developed equations are directly applicable to the experimental system. Only steady-state, axial flow in a long tube has been considered. Therefore, variations in the angular direction of pipe flow are equal to zero because of axial symmetry. The equation of continuity for one phase of suspension flow in cylindrical coordinates is therefore

$$\frac{\partial r\overline{v'_r \varepsilon'}}{\partial r} = 0 \qquad (47).$$

Integrating and applying Prandtl's mixing length hypothesis gives the result:

$$\overline{v'_r \varepsilon'} = \frac{C_w}{r} = l_\varepsilon l_w \frac{1}{\bar{\varepsilon}} \frac{d\bar{\varepsilon}}{dr} \frac{d\bar{V}_z}{dr} \qquad (48).$$

In processing Equation (48), the only difference between the final equation and the analogous equation in Cartesian coordinates is that the constant becomes different by a factor of $1/R$. The equations for the consistency and velocity distributions may therefore be written in the following form:

$$\ln\left(\frac{1-\bar{c}}{1-\bar{c}_o}\right) = -\frac{C'_w}{\kappa_\varepsilon \kappa_w}\frac{\kappa_*}{v_*}\left(\ln s - \ln s_o\right) \tag{49}$$

and

$$\frac{dv^+}{d\ln s^+} = \sqrt{\frac{\bar{\varepsilon}}{\kappa}}\sqrt{1 - \frac{\mu a \overline{\varepsilon v_{rz}} R}{\rho v_*^2}} \simeq \frac{1}{\kappa} \tag{50}$$

where $\underline{C}'_{\underline{w}} = \underline{C}_{\underline{w}}/\underline{R}$. These equations may now be directly applied to steady-state pipe flow.

EXPERIMENTAL

The experimental program consisted of two principal parts. These were (1) the determination of velocity profiles and pressure-loss behavior in order to characterize the momentum transfer properties of the suspension, and (2) the measurement of time-mean consistency distributions in turbulent suspension flow. The experimental work was limited to one type of wood pulp in the consistency range of 0.05 to 0.50 g./100 ml. Only fully developed turbulent flow at flow rates high enough to preclude the existence of plug flow was investigated. Reynolds numbers based on water density and viscosity ranged from 50,000 to 160,000. The experimental work was performed in a 1.865-inch i.d. vertical pipe loop.

EQUIPMENT — THE PIPE LOOP

The experimental pipe loop used during this thesis was a modification of a pipe loop described by Seely (18). The modifications, however, were rather significant and the considerations leading to these changes indicate some important factors in the design of flow systems. The pipe loop which was initially tested is shown in Fig. 3. The significant feature of the design was the configuration of the approach flow to the test section. The test section was located 55 diameters downstream of a smooth 180-degree bend with a radius of 2.5 ft. The loop was tested using water as a test fluid. Velocity profiles measured across the diameter of the pipe in the plane of the 180-degree bend were found to be skewed toward the outside of the bend, as shown in Fig. 4. Velocity profiles measured at 45 degrees to the plane of the bend after positioning the test section 80 diameters downstream from the bend were also skewed

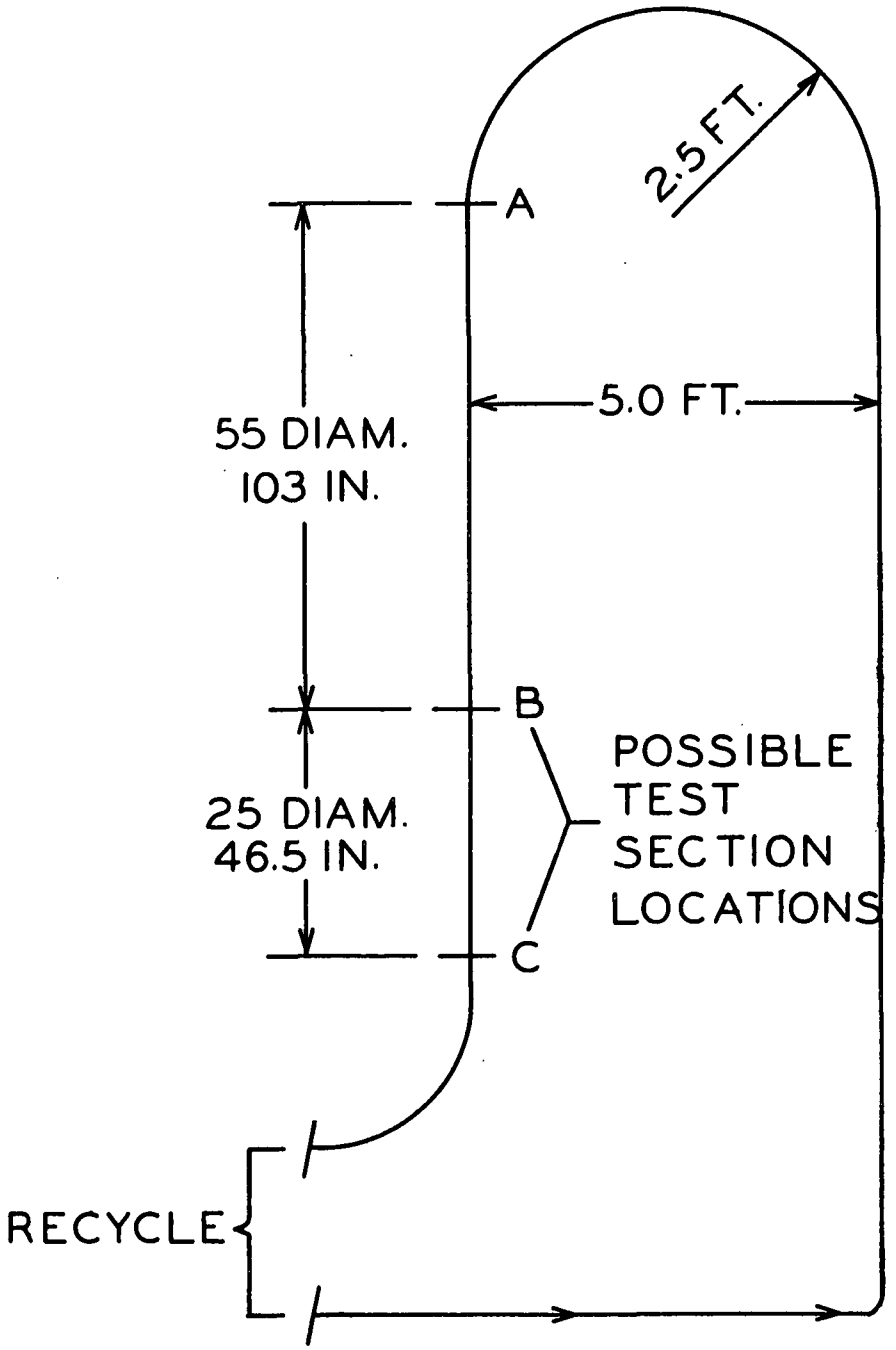

Figure 3. Geometry of Original Pipe Loop

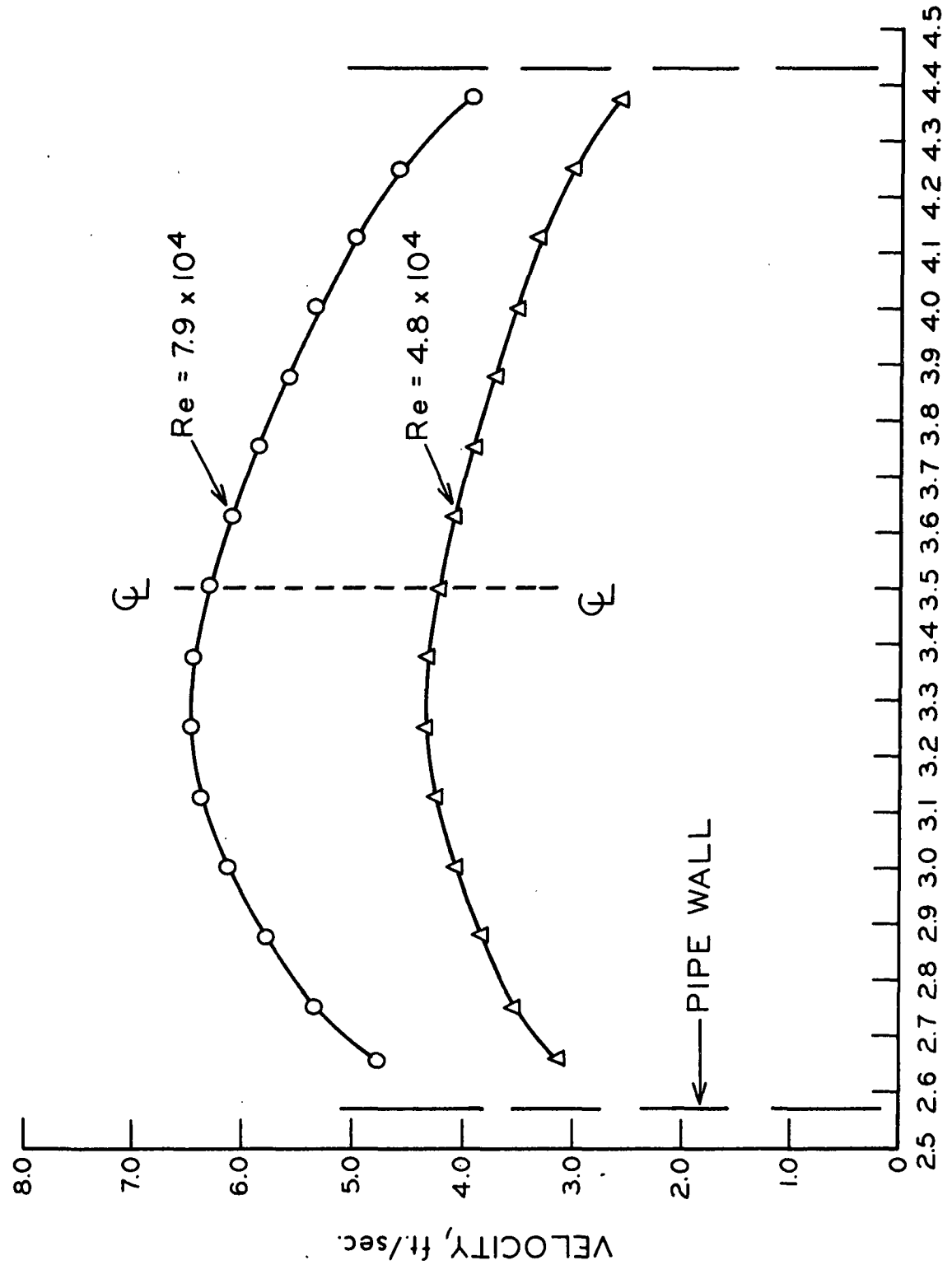

Figure 4. Skewed Velocity Profiles from Original Pipe Loop

toward the outside of the bend, although not so badly as at 55 diameters. The asymmetry of these profiles indicated that a fully developed turbulent flow condition could not be obtained with the existing pipe loop.

This observation was somewhat surprising in view of the literature concerning entrance effects (24,36). Nikuradse (24) reported that a fully developed velocity profile is achieved only 25 to 40 diameters from an inlet. Deissler (36) achieved fully developed profiles 45 tube diameters downstream from a right-angle entrance. However, he found that velocity profiles were still developing slightly at 100 diameters from a rounded entrance. This suggests that the straight length necessary to achieve fully developed velocity profiles depends on the type of entrance to that straight length. The pipe loop was therefore redesigned to eliminate the 180-degree bend. The new pipe loop had the test section 104 diameters downstream of a 90-degree short-radius elbow.

The pipe loop and the pressure instrumentation are shown in Fig. 5 and 6. The flow loop was vertical to minimize gravitational effects and was constructed of seamless, hydraulically smooth stainless steel tubing which had an inside diameter of 1.865 inches. The adjoining sections were carefully aligned to prevent flow disturbances at these points. Auxiliary piping and valves were 2-inch diameter brass. The suspension was pumped by two Jabsco pumps in parallel. Each pump was driven through a Speed Selector variable-speed system by a 3-hp. electric motor. The maximum discharge rate was approximately 150 g.p.m. at 30 ft. of head. The loop was equipped with a 2-inch Foxboro Dynalog magnetic flowmeter and calibrated discharge tank for flow measurement. A jacketed stock tank allowed the temperature to be controlled to within about 0.5°C. by manual control of cooling-water and steam feeds. The stock tank was equipped with an overflow

siphon to allow continuous bleeding of purge water in order to maintain a constant consistency. The siphon was located behind a fine-mesh screen with a large surface area. A diaphragm valve on the discharge side of the loop allowed control of the static pressure level in the system. A 1/4-hp. Lightnin' mixer was used to maintain agitation in the stock chest. Pressure differentials were measured with liquid-liquid manometers.

The modified pipe loop was again tested using water as the test fluid. Figure 7 shows velocity profiles measured at three widely different flow rates. These profiles were symmetrical about the pipe axis whether measured in the plane of the elbow or perpendicular to it. Also, the velocity profiles fit the familiar logarithmic velocity distribution law, as shown in Fig. 8. Pressure drops and flow rates were converted to a friction factor-Reynolds number correlation (Fig. 9). The agreement between these data and the established correlation (35) also indicates that the modified pipe loop functioned properly.

The results of this investigation as well as some of the literature (36) indicate that smooth, curved approaches to a straight pipe are geometrically undesirable for developing steady-state velocity profiles. The reason for this appears to be that long, curved surfaces generate stable secondary flow patterns. Sharp-edged entrances or short-radius bends apparently do not develop stable secondary flows.

VELOCITY PROFILE MEASUREMENTS

Velocity profile measurements were made with an annular-purge impact probe (16). This probe consisted of a conventional impact probe surrounded by an annular jacket. The impact probe was water filled and connected to a manometer.

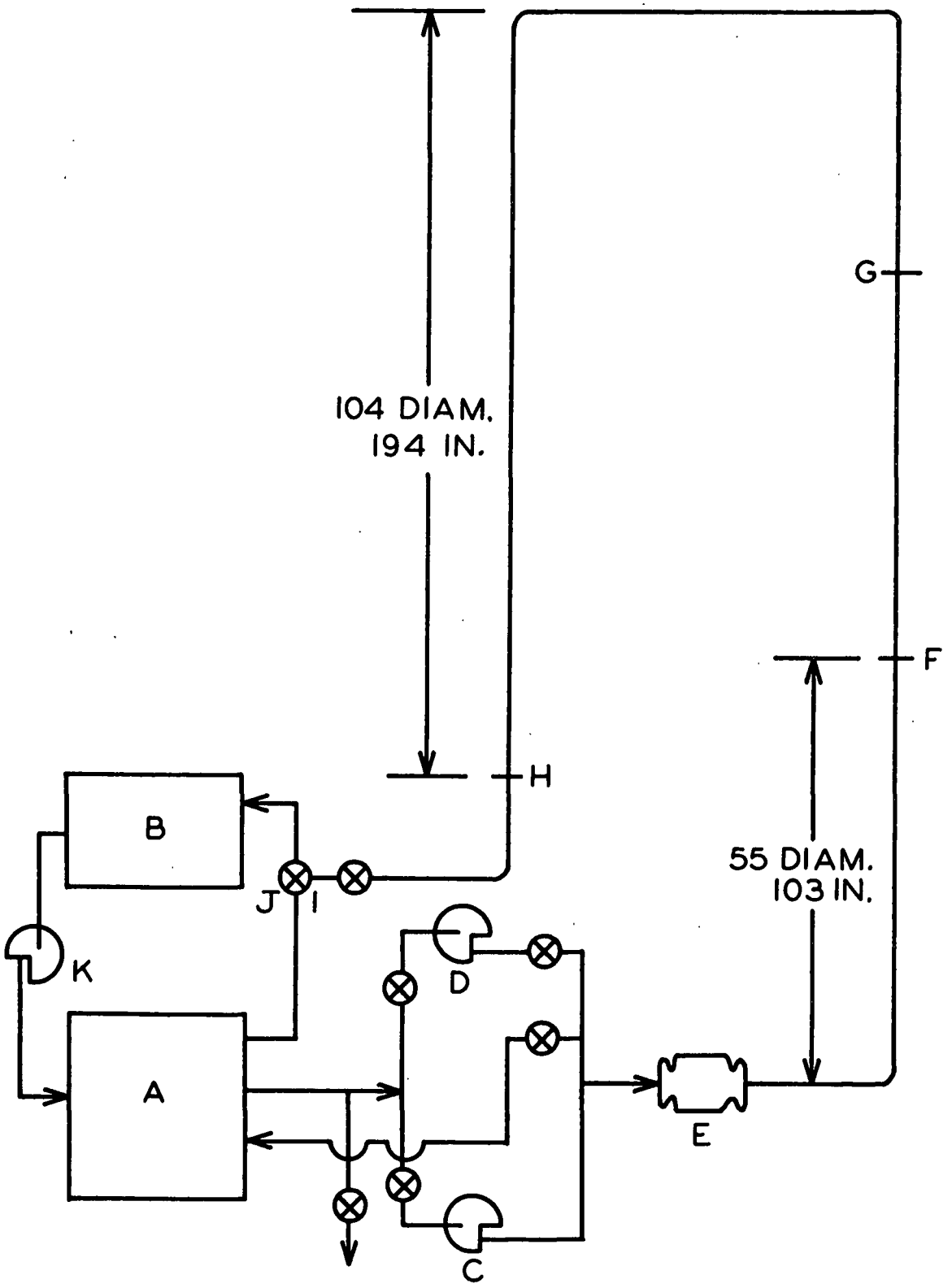

Figure 5. Pipe Loop

Key to Figure 5

A Stock chest. Stainless steel, jacketed, open depth 3 ft., diameter 5 ft.

B Volumetric discharge tank. Stainless steel, open depth 3 ft., diameter 1 ft., 6 in.

C,D Jabsco Model 3200-01. Size 2-in. ball-bearing rotary pumps, each driven through a Speed Selector variable-speed drive no. 409-510; 267-2400 r.p.m. by a 3-hp. 1150-r.p.m. NEMA frame 215; squirrel-cage motor.

E Foxboro Dynalog magnetic flowmeter, 2 inch.

F Upstream static pressure tap, 3 positions.

G Downstream static pressure tap, 3 positions (separation from F = 88 in.).

H Lucite test section for impact probe and consistency probe.

I Diaphragm valve to maintain positive pressure in loop.

J Quick-opening 3-way ball valve.

K Recycle pump.

The loop is constructed of 2-in. o.d., 1.865-in. i.d., stainless steel tubing mounted vertically on unistrut. Other piping is 2-in. brass.

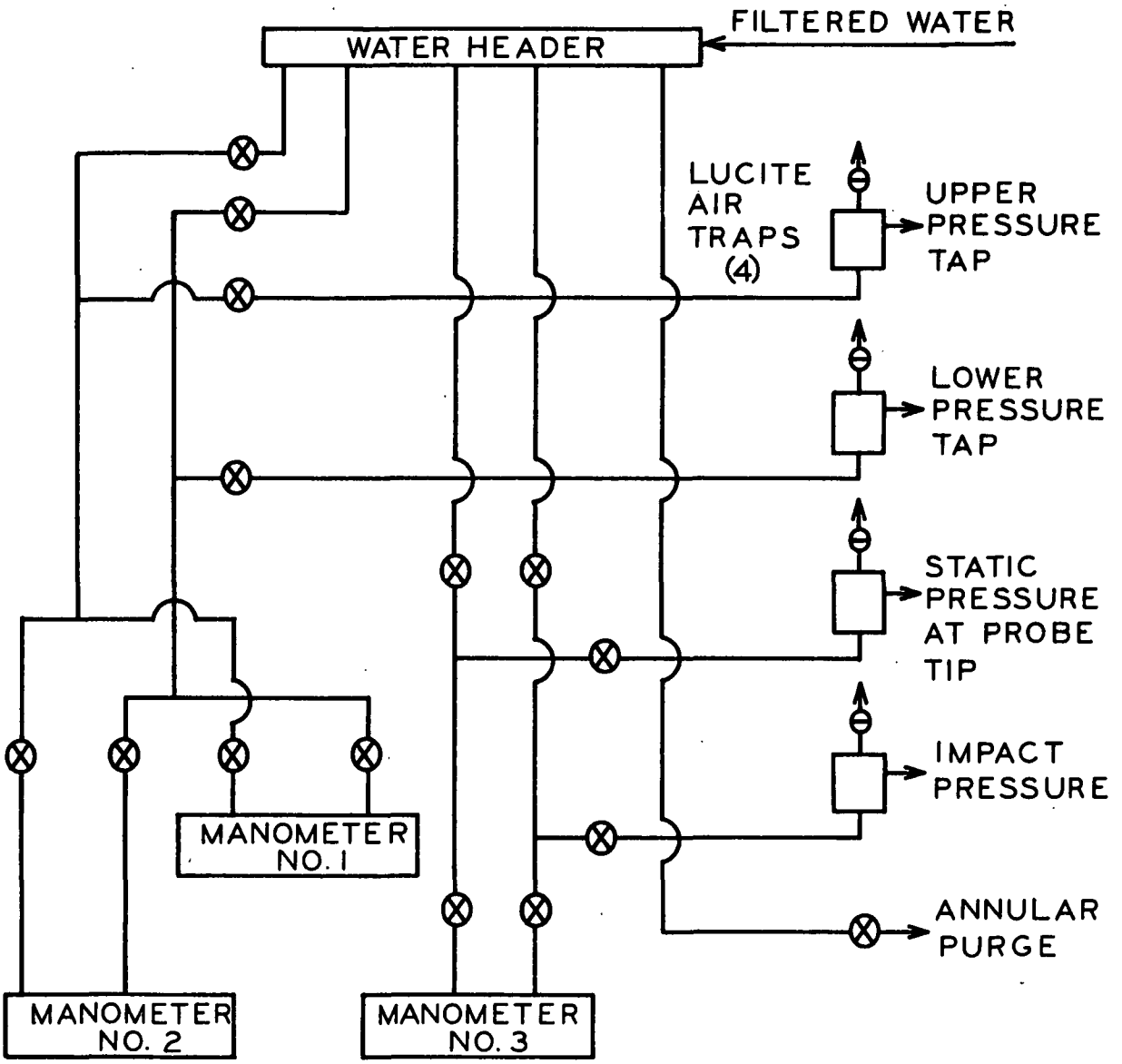

MATERIALS: 1/8" X 1/4" INSTRUMENT TUBING WITH APPROPRIATE POLYFLOW FITTINGS, 1/8" CIRCLE SEAL VALVES

Figure 6. Pressure Instrumentation System for Pipe Loop

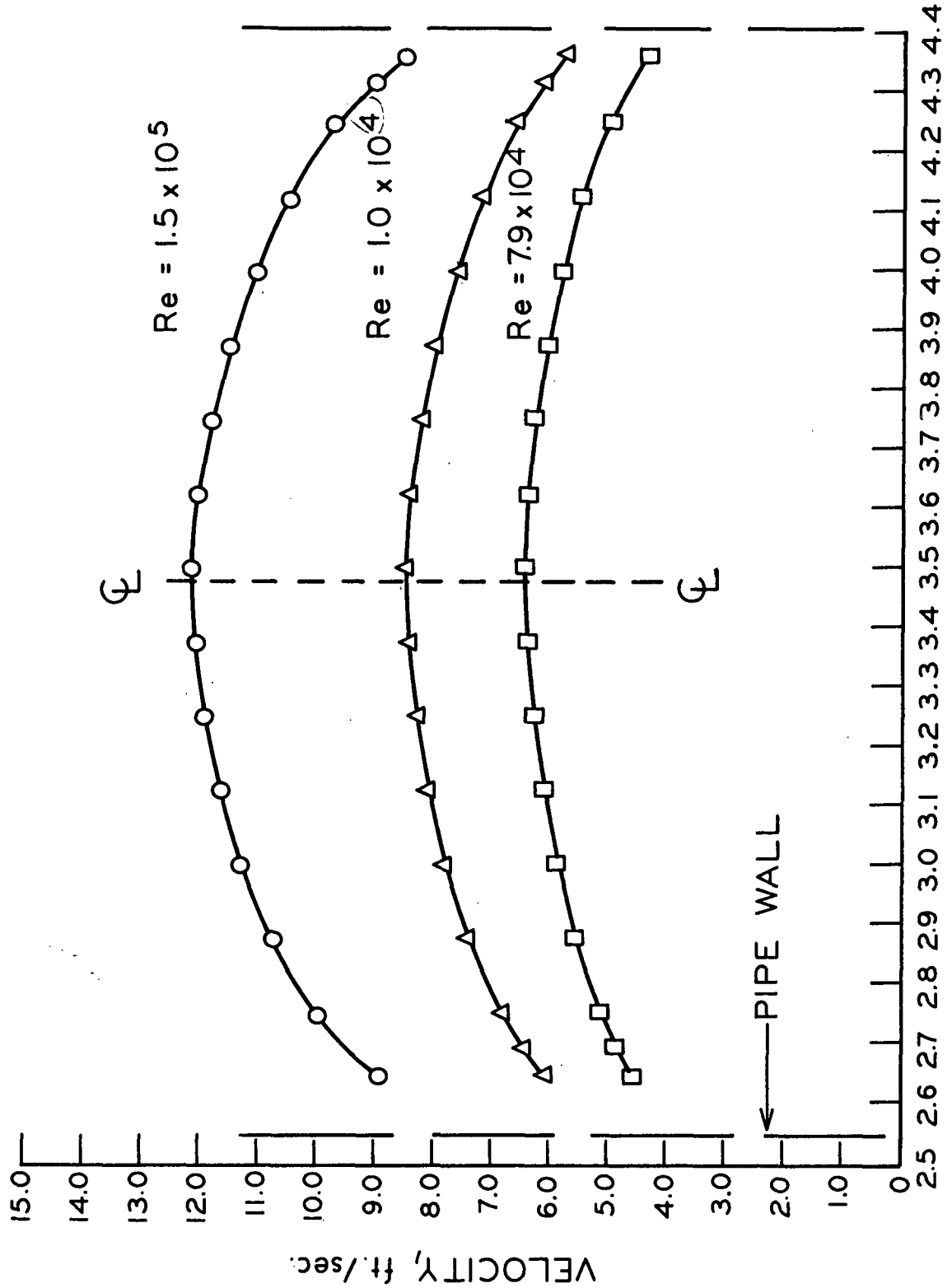

Figure 7. Symmetrical Velocity Profiles from Modified Pipe Loop

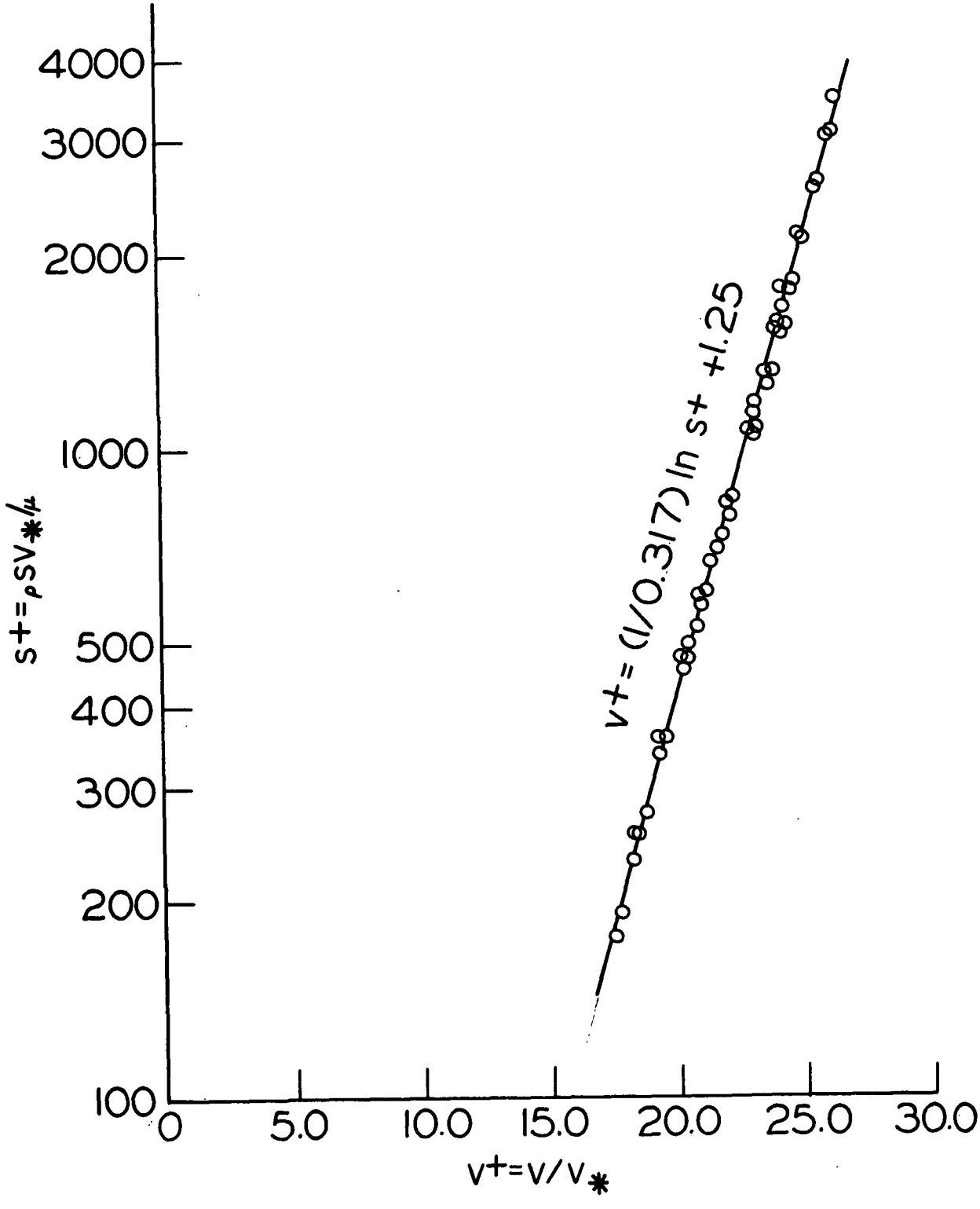

Figure 8. Reduced Velocity Profiles

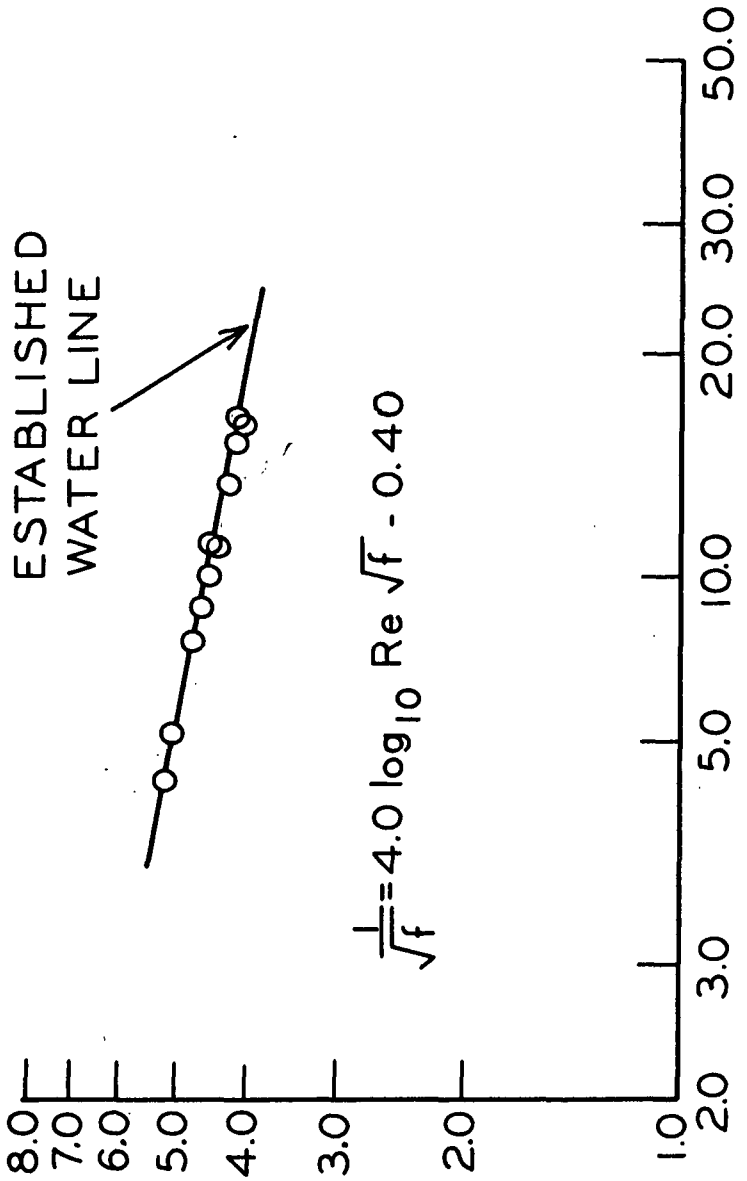

Figure 9. Friction-Factor vs. Reynolds Number, Water at 20°C.

The tip of the impact probe projected slightly beyond the outer tube, and was effectively kept free from fiber stapling by a continuous flow of purge water through the annular space between the two tubes. The outside tube used in this investigation had a 0.094-in. diameter and extended 1-3/4 in. upstream of the diametrical support bar. A sketch of the probe is shown in Fig. 10.

The probe was tested in water flow and found to function as previously described (16,18). The velocity profiles agreed well with the logarithmic velocity distribution law as was shown in Fig. 8. The probe was also checked by comparing the integrated velocity profiles to volumetric discharge rates measured with a calibrated magnetic flowmeter (Table I). The agreement was very good.

TABLE I

COMPARISON OF BULK FLOW RATES

Magnetic Flowmeter, $ft.^3/sec.$	Integrated Velocity Profile, $ft.^3/sec.$	Difference, %
0.068	0.066	2.9
0.068	0.066	2.9
0.089	0.088	1.1
0.090	0.087	3.3
0.090	0.088	2.2
0.090	0.089	1.1
0.107	0.104	2.8
0.113	0.110	2.7
0.134	0.129	3.7
0.135	0.134	0.7
0.138	0.135	2.2
0.190	0.187	1.6

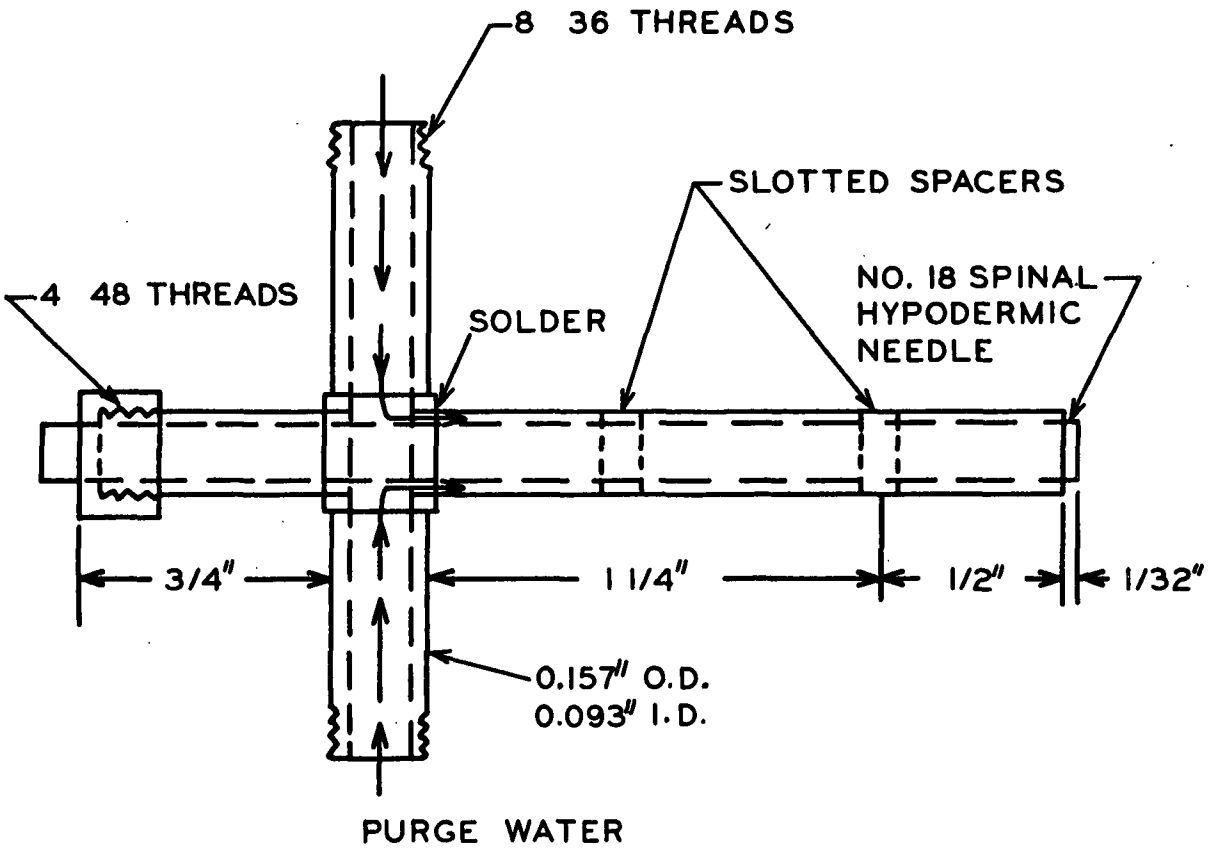

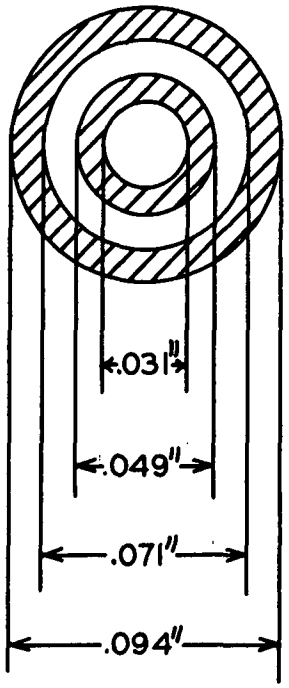

Figure 10. Annular-Purge Impact Probe

CONSISTENCY DISTRIBUTION MEASUREMENTS

The measurement of radial fiber consistency distributions in pipe flow poses many problems. It is desirable to measure local concentrations in a sample volume which is small compared to the pipe diameter. In addition, the apparatus should not alter the flow pattern which is being measured. The two requirements are difficult to satisfy for fiber suspensions.

Techniques for the measurement of concentration distributions have been described in the literature for other somewhat simpler suspensions. Some success has been obtained in measuring concentration distributions for dilute suspensions of rigid spheres in laminar flow by using crossed-beam photoextinction measurements (37,38). However, the technique does not appear readily applicable to turbulent fiber suspensions because of difficulties in cross-correlation analysis for long flexible fibers. Approximate concentration gradients have been obtained for pipeline flow of sand-water suspensions using a gamma radiation technique (39). Accurate radial variations are not possible with this technique, however, because the measurements are average values over a chordal gamma-ray path which itself has a concentration gradient. None of these previously used techniques are considered by the author to be desirable for measuring fiber consistency variations in pipe flow. Also, it is felt that direct physical sampling of the flow stream is impractical.

ANNULAR-PURGE CONSISTENCY PROBE

A new technique for measuring local consistency variations was developed for this investigation. The technique is based on the measurement of light scattered from the particles in suspension.

The consistency probe consisted of a concentric, two-branch light guide enclosed in an annular-purge probe[1], as shown in Fig. 11. In operation, a small area of the approaching suspension was illuminated through the outer branch of the light guide; the back-scattered light was then transmitted through the core of the light guide to a photodetection circuit. The light guide was effectively kept free from fiber stapling by a continuous flow of purge water through the annular space between the light guide and the purge jacket. The outside diameter of the entire probe was 0.142 in. and extended 1.6-in. upstream of the diametrical support bar. The support bar was connected to a traversing mechanism which allowed the position of the probe to be determined to the nearest 1/64 inch. The two-branch light guide was fabricated to specification by the American Optical Company as shown in Fig. 12.

A stable light source was obtained from a 60-watt quartz-iodine lamp powered by a regulated d.c. power supply. The quartz-iodine lamp was mounted in a cylindrical chamber. A cover plate, which contained the connection for the light guide, was spring-loaded against the lamp holder in order to assure a fixed geometry between the lamp and light guide tip. A 10-volt, 7-ampere d.c. power supply was wired directly to the lamp in order to minimize points of variable resistance. A Sorensen voltage regulator was used to control the line voltage to the d.c. power supply. Detailed descriptions of the light source and power supply are given in Appendix I.

---

[1] A prototype of this probe was built by the American Optical Co. according to specifications engineered by the Beloit Corp. who also were first in using this probe in exploratory consistency measurements (40).

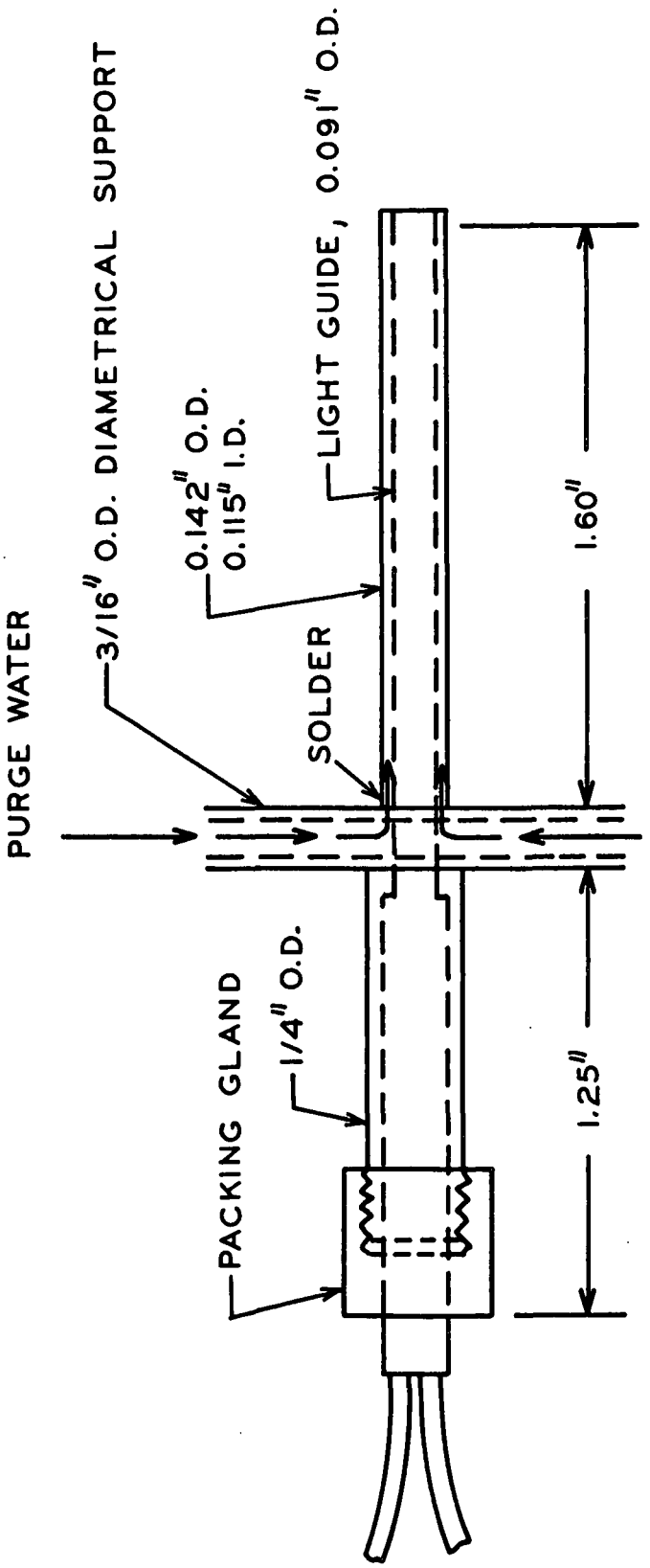

Figure 11. Annular Purge Consistency Probe

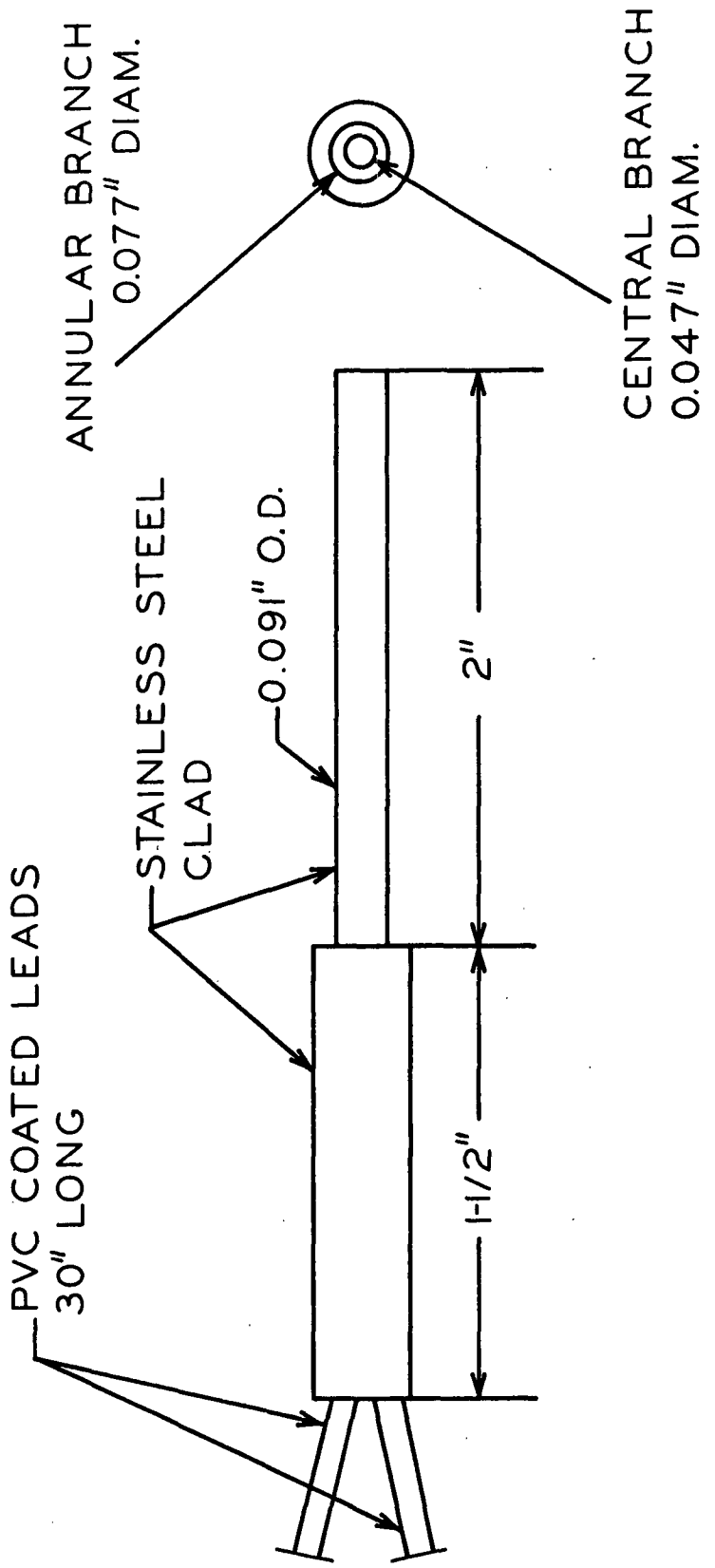

Figure 12. Two Branch Light Guide

The basic elements of the photodetection circuit were an RCA 931A photomultiplier tube and an Eldorado Model 201 photometer. The photometer had a current response of 10 microamperes to 0.001 microampere full scale in 9 ranges and was linear to within 0.5%. The photometer was equipped with monitoring terminals which had an output of 100 millivolts full scale. The actual measurements used in this investigation were taken from a Rubicon galvanometer which was connected to the photometer monitoring jacks as shown in Fig. 13. This circuit provided for damping of the time-dependent fluctuations in order to get a time-smoothed average of the light measurements. A block diagram of the overall consistency measuring system is given in Fig. 14. The reference system which was used to check the stability of the optical and electrical circuit is also included in this figure. This system was an arbitrary reference which allowed detection of any change in either the light source or photodetection circuit. Light was transmitted via a spare two-branch light guide to a diffuse opal glass standard. The geometry between the light guide and reflectance standard was of course fixed. The reflected light was transmitted to the photomultiplier and measured on the photometer. The system was checked before and after each run and exhibited no more than a 1% variation over the entire course of this investigation.

TESTING AND CALIBRATION OF CONSISTENCY PROBE

The consistency probe was calibrated in a small, well-mixed vessel. The two-branch light guide was mounted flush with the wall of the 2.6-liter Lucite mixing chamber, as shown in Fig. 15. The vessel was agitated by a variable-speed impeller which was located approximately one inch from the tip of the light guide.

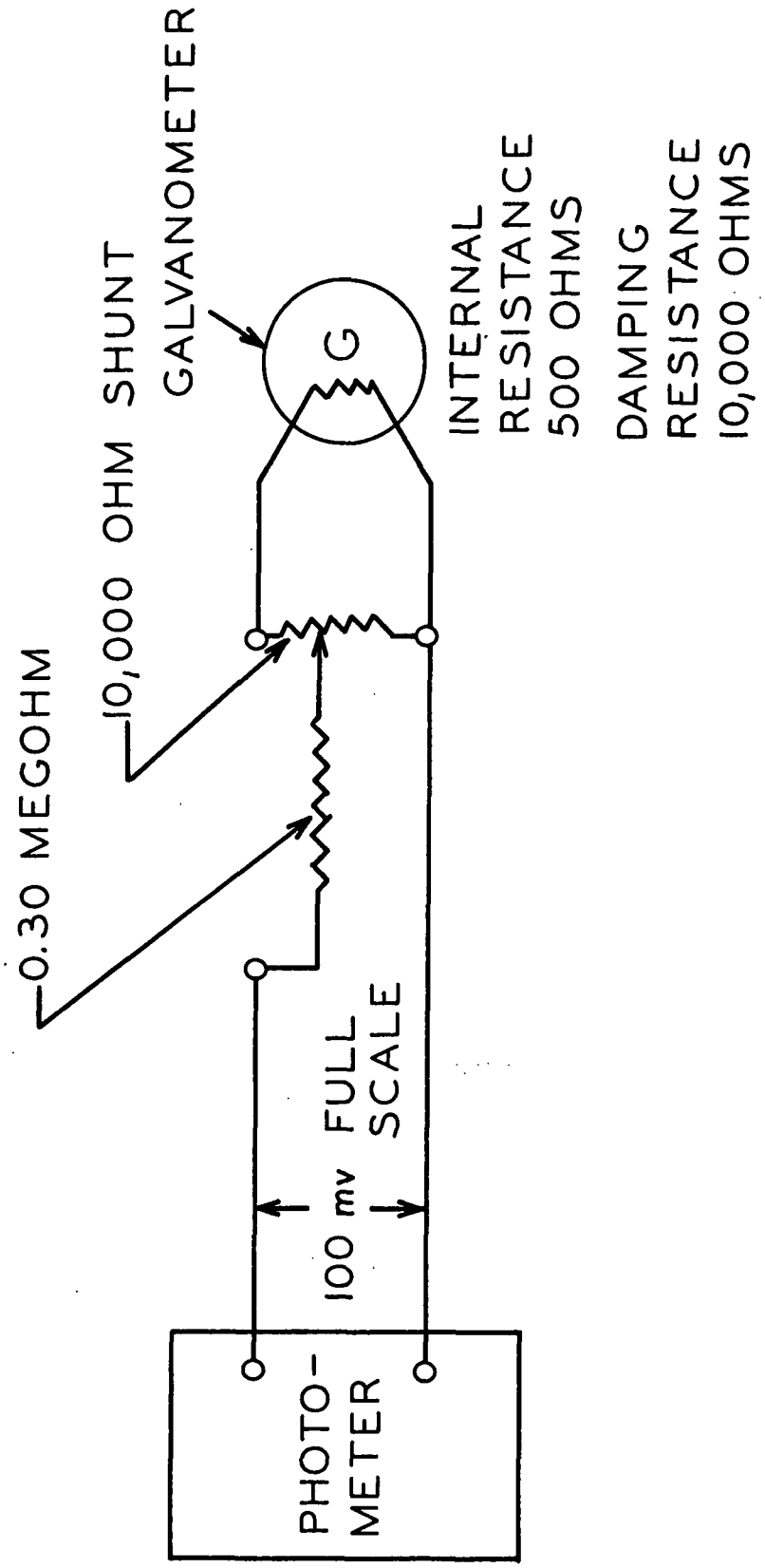

Figure 13. Galvanometer Circuit

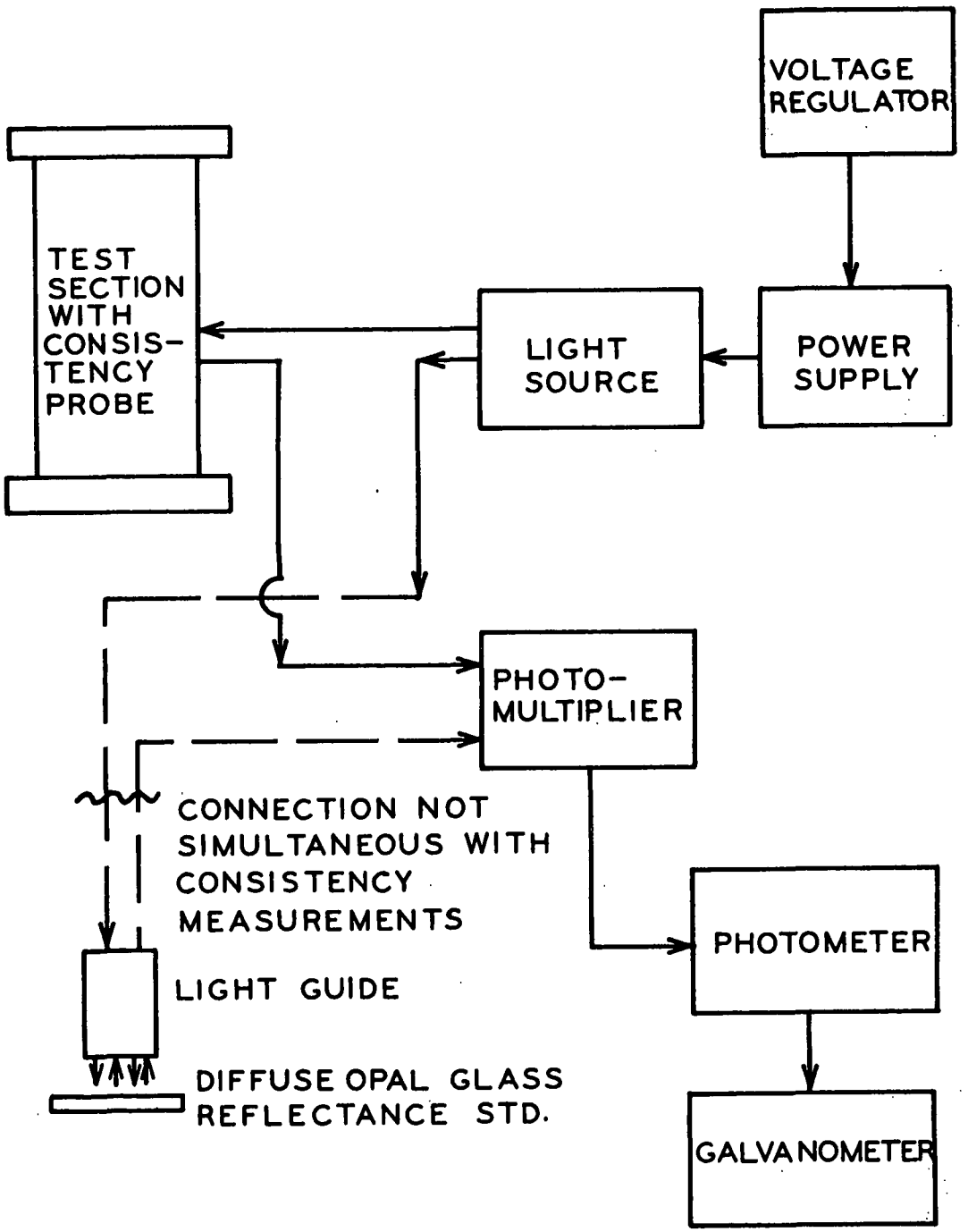

Figure 14. Schematic of Consistency Measuring System

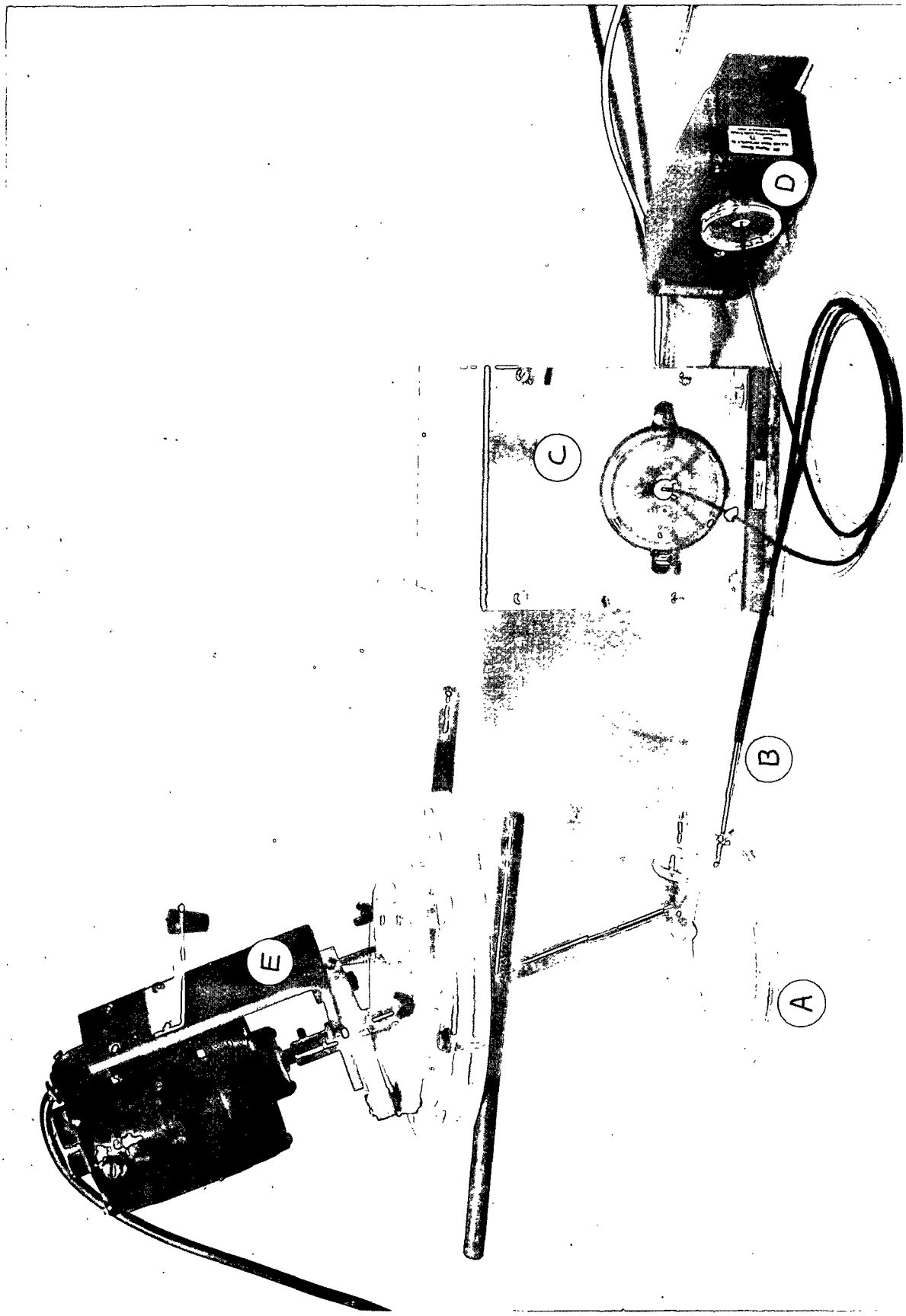

Figure 15. Consistency Calibration Apparatus

A, Mixing Vessel; B, Two-Branch Light Guide; C, Light Source; D, Photomultiplier; E, Variable-Speed Stirrer

The suspension was highly turbulent in the vicinity of the probe tip and the measurements were unaffected by the agitation rate provided the rate was sufficiently high to prevent settling or stratification. It should be noted that the impeller of the mixer was axially aligned with the probe tip and discharged against the probe. This arrangement therefore approximated the average flow pattern which occurred around the probe in pipe flow, as shown in Fig. 16. The calibration data are given in Table II and Fig. 17. It can be seen that the light measurements are a sensitive and smooth function of the consistency.

TABLE II

CALIBRATION OF CONSISTENCY PROBE

Consistency, %	Normalized Light Measurements
0.052	6.50
0.104	12.25
0.155	18.00
0.207	22.75
0.258	27.10
0.310	31.50
0.361	35.75
0.412	39.75
0.463	43.45
0.564	50.00
0.665	56.00
0.755	60.50
0.805	63.00

The validity of the calibration for use in turbulent pipe flow was substantiated by comparison of the integrated consistency profiles with the known mass flow rate of fibers. These results are shown in Table III. The agreement is very good and is strong evidence for the validity of the calibration.

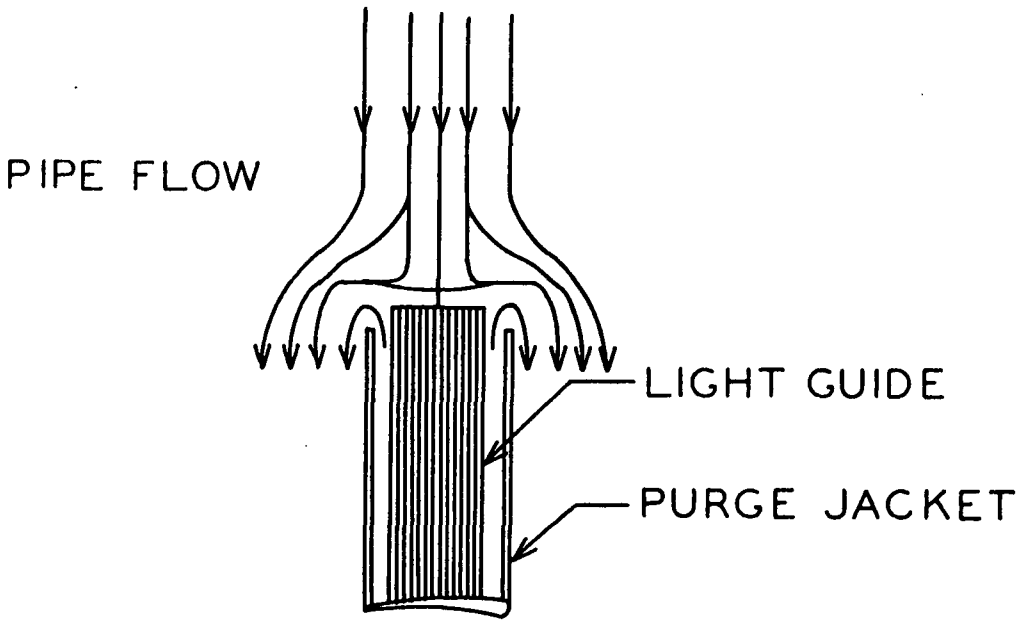

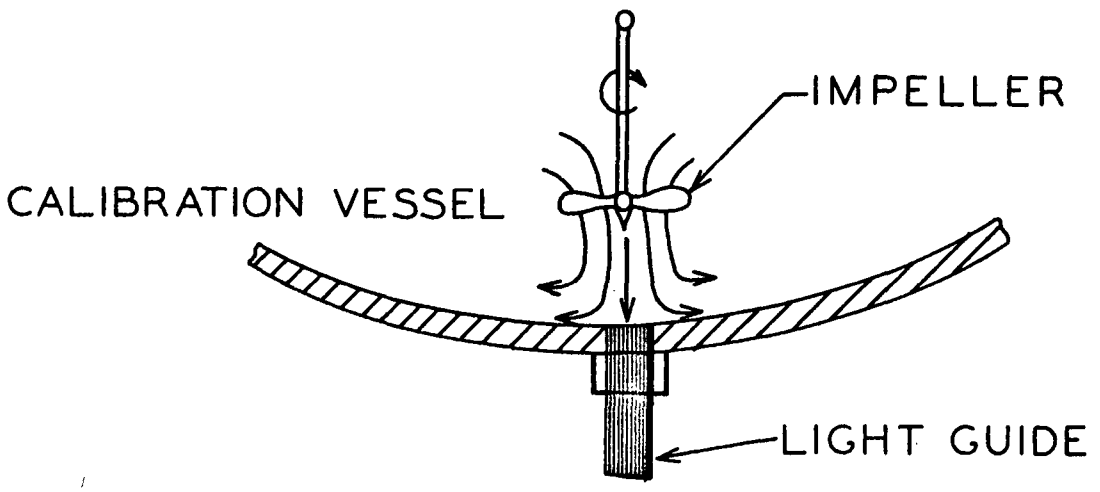

Figure 16. Comparison of Stream Lines in Pipe Flow and Calibration Vessel

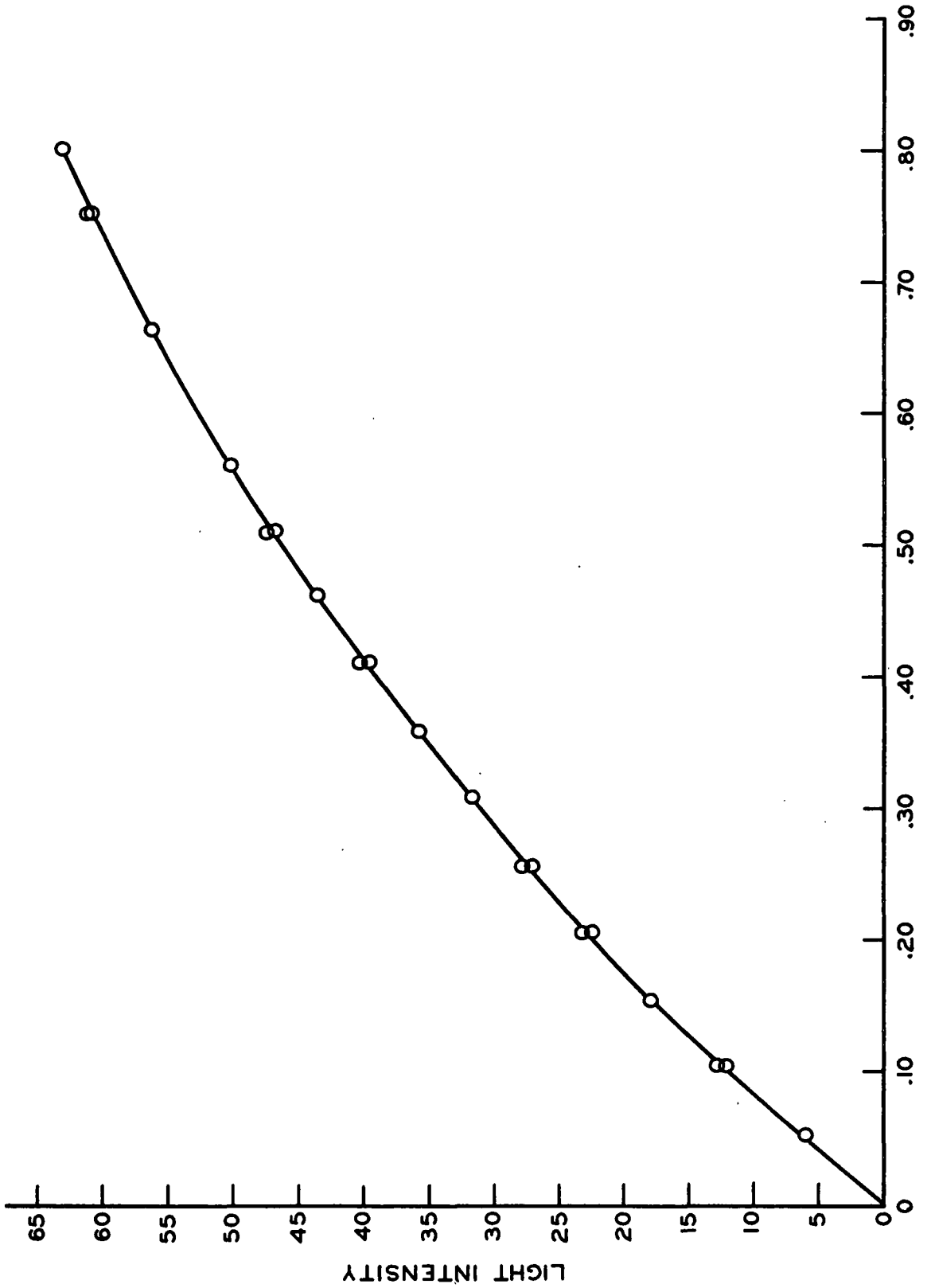

Figure 17. Calibration of Consistency Probe

TABLE III

COMPARISON OF MASS FLOW RATES

$\langle\Gamma\rangle$, g./100 ml.	$\langle\underline{Q}\rangle$, ft.^{3}/sec.	$\langle\underline{Q}\rangle\langle\Gamma\rangle$, lb./sec.	$\int_0^R 2\pi \underline{r}\bar{\Gamma}\bar{v}d\underline{r}$, lb./sec.
0.0425	0.117	3.10×10^{-3}	3.15×10^{-3}
0.0425	0.195	5.18×10^{-3}	5.34×10^{-3}
0.122	0.067	5.10×10^{-3}	4.86×10^{-3}
0.122	0.091	6.93×10^{-3}	6.68×10^{-3}
0.122	0.114	8.68×10^{-3}	8.43×10^{-3}
0.122	0.205	15.61×10^{-3}	15.62×10^{-3}
0.178	0.114	12.68×10^{-3}	12.12×10^{-3}
0.178	0.192	21.36×10^{-3}	21.61×10^{-3}
0.243	0.114	17.30×10^{-3}	17.12×10^{-3}
0.243	0.195	29.61×10^{-3}	30.23×10^{-3}
0.358	0.114	25.49×10^{-3}	23.55×10^{-3}
0.358	0.194	43.35×10^{-3}	39.60×10^{-3}
0.460	0.118	33.73×10^{-3}	31.98×10^{-3}
0.460	0.195	55.97×10^{-3}	54.47×10^{-3}

Profiles measured in water gave a zero reading of reflected light across the entire pipe diameter. This result indicates that changes in the water flow and reflections from the pipe wall did not affect the measurements. The purge flow from the probe had no appreciable effect of the measurements provided the tip of the light guide was mounted flush with the end of the purge jacket. Figure 18 shows a plot of the measured consistency versus purge discharge velocity.

Some preliminary investigations indicated that fiber orientation could have an effect on the consistency measurements. The approximate effect of fiber orientation on light scattering was determined by measuring the differences between the light scattered from fibers which were oriented parallel to the probe

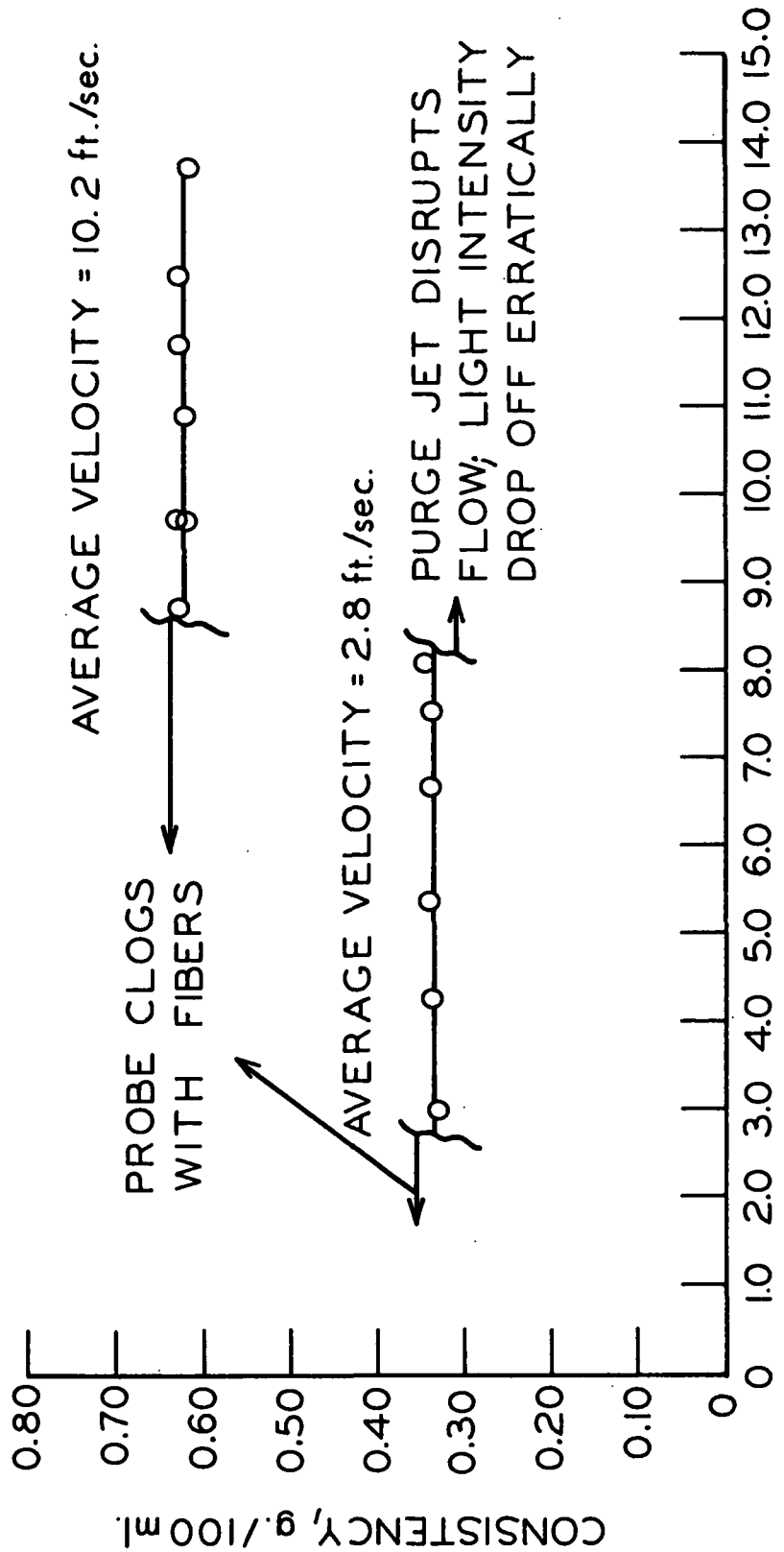

Figure 18. Stability of Annular-Purge Consistency Probe

axis and from fibers which were perpendicular to the probe axis. The different orientations were obtained by suspending the fibers in a viscous polymer solution. The back-scattered light from fibers aligned perpendicular to the probe axis was considerably higher than that for fibers aligned parallel with the probe axis. However, fiber orientation appears to be a negligible factor in the consistency profile measurements as evidenced by the agreement between the integrated consistency profiles and the fiber mass flow rates. Also, changes in the purge flow rate would be expected to have an appreciable effect if fiber orientation were important.

PROCEDURES

FIBER PROPERTIES

The wood fibers used in this thesis were a bleached alpha-grade sulfite pulp. The principal species was true fir with a small percentage of spruce and/or hemlock. The dimensions and hydrodynamic properties of the fibers are shown in Tables IV and V. These properties are presented as a function of circulation time in order to determine the refining effects on the fibers. There was no appreciable change in the fiber properties after a small initial increase in the specific surface during the first two hours of circulation. Since the velocity and consistency distribution measurements were not begun until after two hours of circulation, the changes in fiber properties were considered negligible.

TABLE IV

INDIVIDUAL FIBER DIMENSIONS[a]

Original pulp sample	
Arithmetic average fiber length, mm.	1.38
Weighted average fiber length, mm.	2.07
Arithmetic average fiber width, μm.	37.1
Arithmetic average cell wall thickness, μm.	3.2
After 15 hr. circulation in loop at 0.350 g./100 ml.	
Arithmetic average fiber length, mm.	1.40
Weighted average fiber length, mm.	2.06
Arithmetic average fiber width, μm.	37.2
Arithmetic average cell wall thickness, μm.	3.0

[a]Values supplied by J. Hankey.

TABLE V

HYDRODYNAMIC PULP PROPERTIES[a]

Original pulp sample	
Hydrodynamic specific volume, $cm.^3/g.$	2.30
Hydrodynamic specific surface, $cm.^2/g.$	6000
After 2 hr. circulation in loop at 0.120 g./100 ml.	
Hydrodynamic specific volume, $cm.^3/g.$	2.30
Hydrodynamic specific surface, $cm.^2/g.$	6500
After 15 hr. circulation in loop at 0.120 g./100 ml.	
Hydrodynamic specific volume, $cm.^3/g.$	2.32
Hydrodynamic specific surface, $cm.^2/g.$	6670

[a]Values supplied by B. D. Andrews.

PRESSURE LOSSES

Static pressure measurements were made at two pressure tap connections which were 47 diameters apart. The first pressure tap was preceded by a straight length of 55 diameters to ensure steady-state flow. Each pressure connection contained three pressure taps which were spaced 120 degrees around the circumference of the pipe. Pressure differentials were measured using a CCl_4-water manometer. The pressure taps were occasionally flushed with water to keep them free of fibers.

VELOCITY PROFILES

Velocity profile measurements were taken across virtually the entire turbulent core of the pipe. The pressure differentials between the impact probe and the static pressure tap were measured on either CCl_4-water or Hg-water

manometers. Readings were taken at two different purge rates to ensure that the purge rate was in the region where it did not affect the impact pressure. Entrained air in the pipe loop was minimized by boiling the water prior to beginning a series of runs. A substantial pressure was also maintained in the pipe loop to minimize entrained air.

CONSISTENCY PROFILES

Consistency profiles were also measured across the turbulent core of the pipe. The light intensity measurements at each position were read from the damped galvanometer described previously. The entire electrical circuit was allowed to warm up for at least one hour prior to each run. The electrical and optical systems were checked before and after each run. The system exhibited no more than a 1% variation during the entire experimental program. The Lucite test section was isolated from extraneous outside light by wrapping it in several layers of black cloth.

RESULTS AND DISCUSSION

As indicated earlier, to characterize fiber suspension flow, a knowledge of the coupled behavior of the fibers and water is necessary. This investigation includes velocity and consistency distributions in an attempt to describe this coupled behavior. Reynolds number-friction factor correlations are also included, primarily to define the flow regime which was under investigation.

REYNOLDS NUMBER-FRICTION FACTOR CORRELATIONS

Reynolds number-friction factor correlations proved to be in general agreement with previous investigators (11,16,18) as shown in Fig. 19 through 22. The friction factors in the plug and damped turbulence region are less than for a Newtonian fluid. Also, the friction factors appear to be approaching the Newtonian values at low consistencies and high Reynolds numbers as reported by Seely (18). The high-consistency suspensions exhibit the familiar plug flow and damped turbulence regimes. These data allow definition of the conditions necessary to achieve damped turbulent flow. The friction velocity was also calculated from these data. Essentially all of the results reported hereafter are in the damped turbulent or Newtonian flow regimes of suspension flow.

VELOCITY PROFILES

Velocity profiles were measured for turbulent suspensions at six consistencies ranging from 0.041 to 0.47 g./100 ml. Reynolds number based on the water density and viscosity ranged from 5.1×10^4 to 1.6×10^5. The velocity profiles were plotted in the form of logarithm of dimensionless position vs. dimensionless velocity following the common practice for Newtonian fluids. As

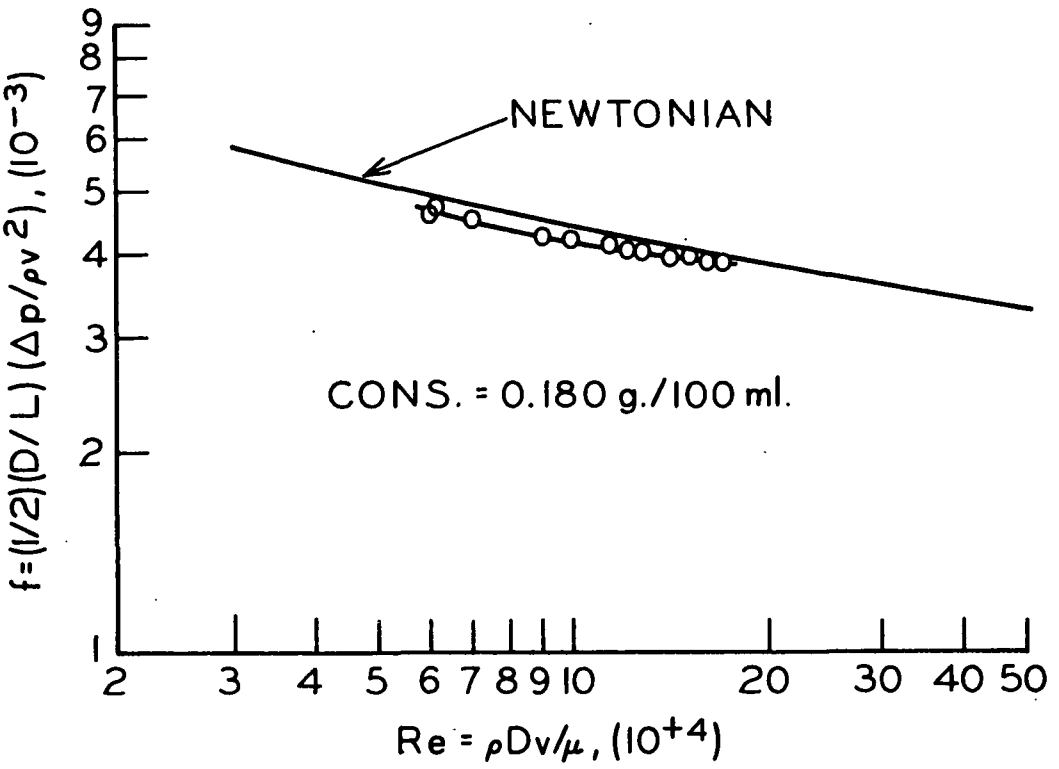

Figure 19. Friction-Factor vs. Reynolds Number

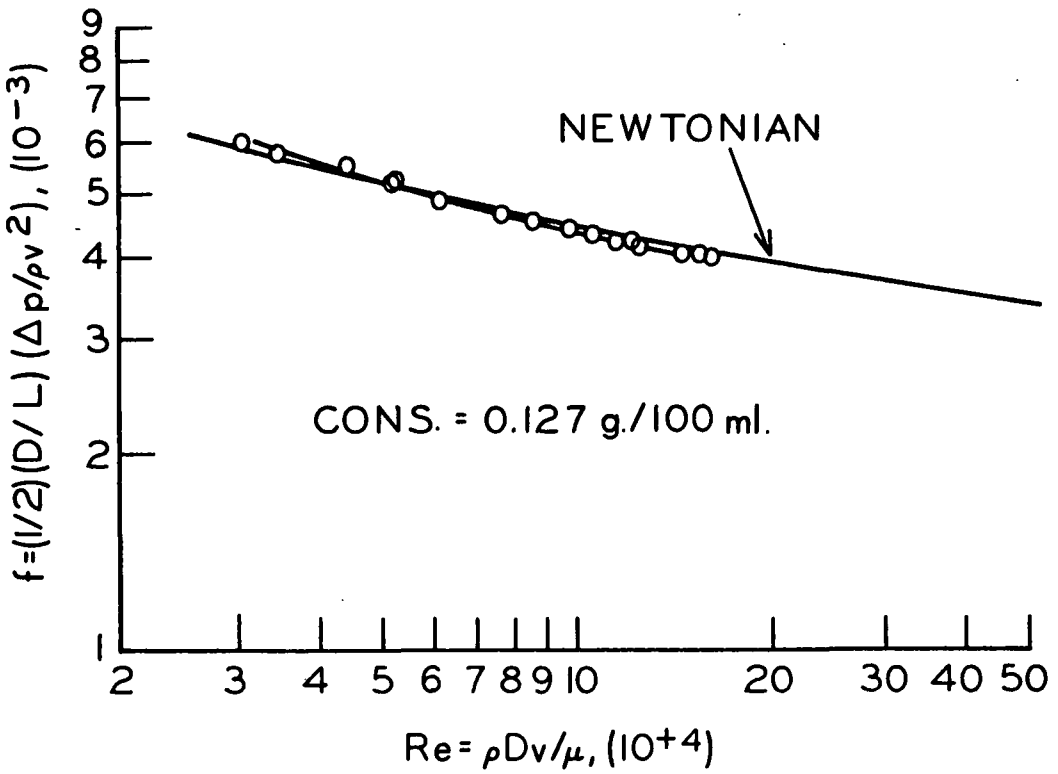

Figure 20. Friction-Factor vs. Reynolds Number

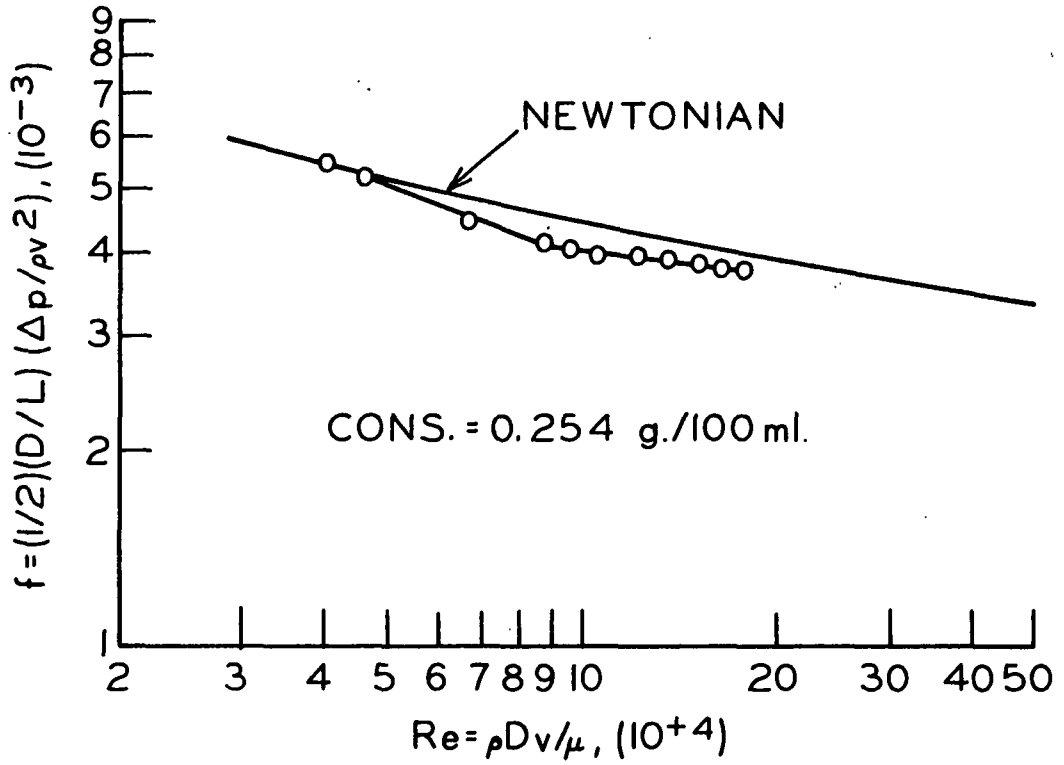

Figure 21. Friction-Factor vs. Reynolds Number

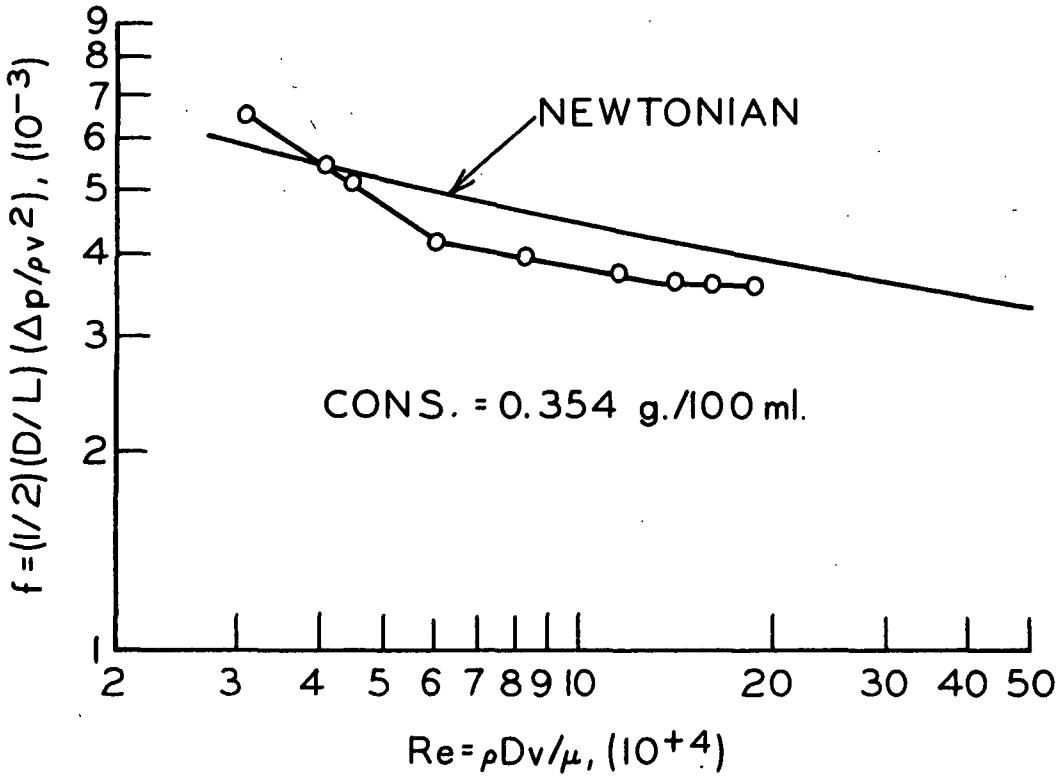

Figure 22. Friction-Factor vs. Reynolds Number

noted previously, for Newtonian fluids in turbulent tube flow, all data from the turbulent core fall on a single straight line regardless of flow rate, viscosity, or tube diameter, and may be represented by Equation (1).

Velocity profile data for water over a range of flow rates were shown in Fig. 8. All of the data for water are correlated by a single straight line function. The velocity profiles for fiber suspensions will be compared to this established velocity profile for water.

Representative samples of the velocity profiles for fiber suspensions are shown in Fig. 23 and 24. The velocity profile data are tabulated in Appendix II. These profiles show a linear correlation, according to Equation (1), for the turbulent flow portions of the profiles. As observed by Mih and Parker (16) and Seely (18), the slope and position of the reduced velocity profiles are different for suspensions than for Newtonian fluids, the slope indicating a lower von Karman constant. Figure 23 indicates that the apparent von Karman constant for suspensions decreases with increasing consistency as observed by these investigators. It will be remembered that these investigators disagreed about whether the von Karman constant is a function of flow rate. The results of this investigation, as shown in Fig. 24, indicate that the apparent von Karman constant increases with flow rate as reported by Seely (18). Also, the von Karman constant approaches the water value at high flow rates.

The velocity profiles will now be compared to the theoretical equations developed previously. It will be recalled that Equation (50) for the velocity profile has the following form:

$$\frac{dv^+}{d\ln s^+} = \sqrt{\frac{\varepsilon}{\kappa}} \sqrt{1 - \frac{\mu a \overline{\varepsilon v}_{rz} R}{\rho v_*^2}} = \frac{1}{\kappa_*} \qquad (50).$$

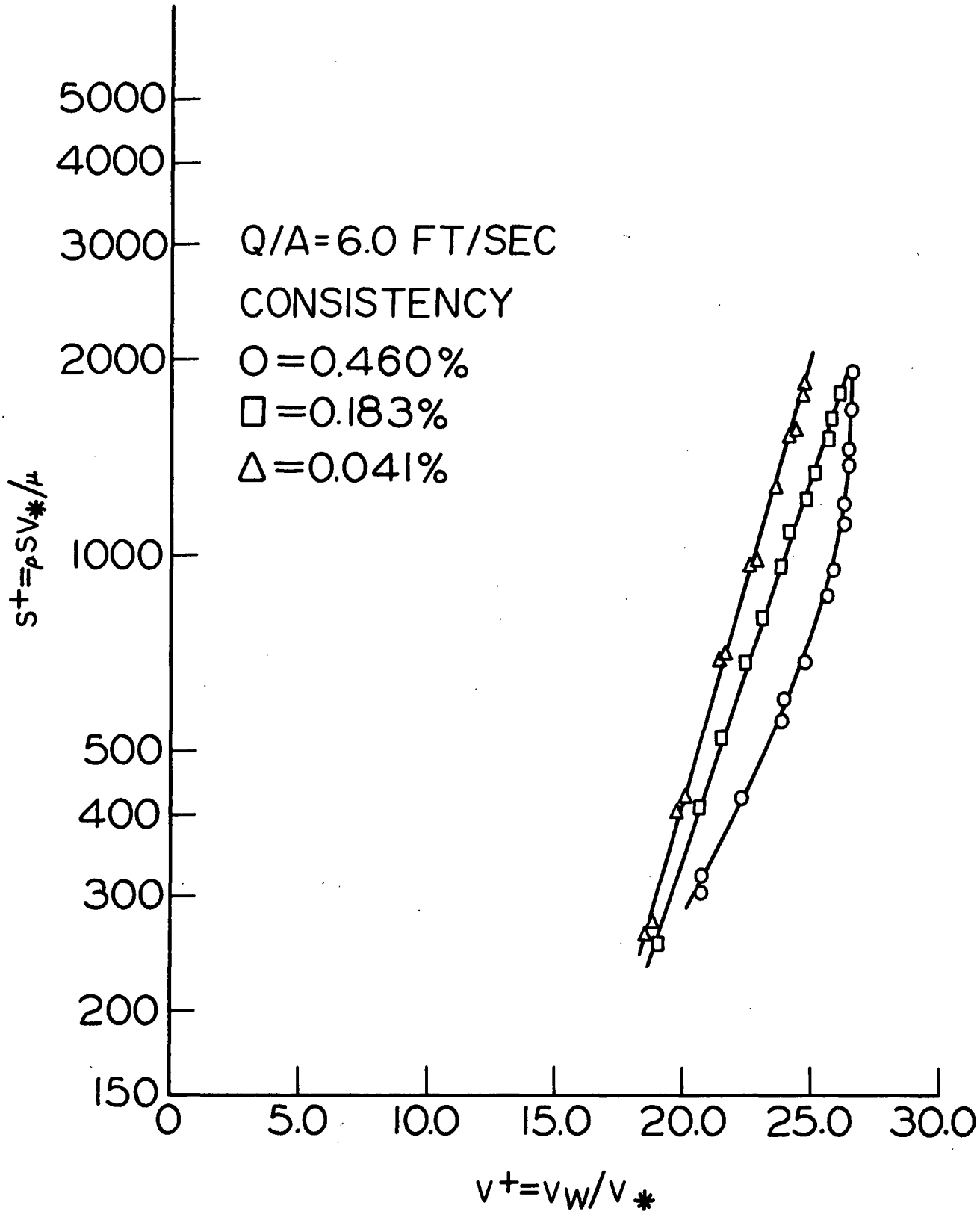

Figure 23. Reduced Velocity Profiles

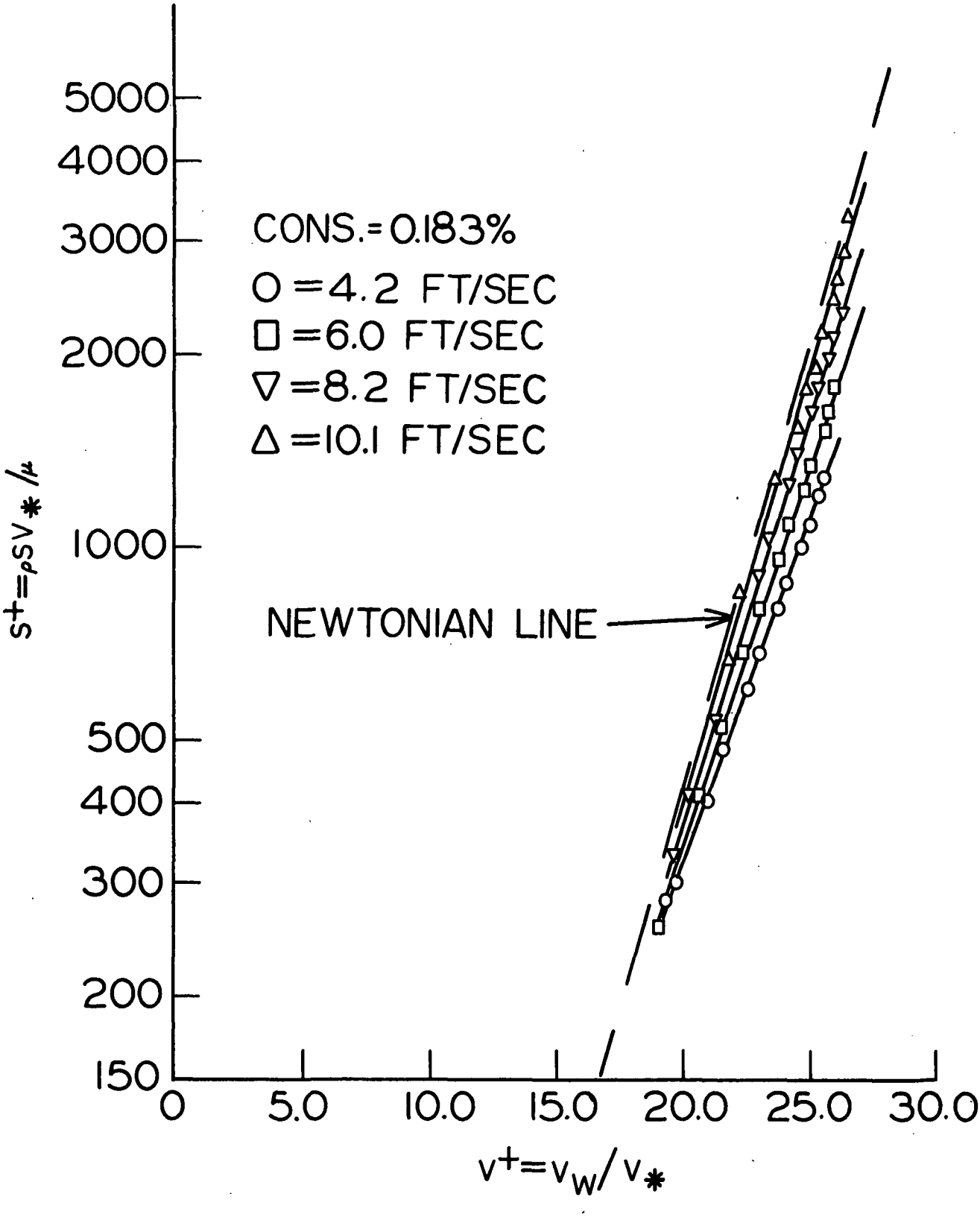

Figure 24. Reduced Velocity Profiles

Inspection of this equation reveals that all quantities are known except the specific resistance, $\bar{a}$, and the relative velocity, $\bar{v}_{rz}$. The specific resistance, which is equivalent to the reciprocal of the Kozeny-Carman expression for Darcy's permeability coefficient (41), may be expressed as follows:

$$\bar{a} = \frac{\bar{k}\left(\overline{\Gamma} V_{sp}\right)^2 S_{sp}^2}{\left(1-\overline{\Gamma} V_{sp}\right)^3} \qquad (51)$$

where:

$\bar{k}$ = Kozeny factor,

$\overline{\Gamma}$ = consistency, g./cc.,

V_{sp} = hydrodynamic specific volume of fibers, and

S_{sp} = hydrodynamic specific surface of fibers.

The Kozeny factor may be expressed by Carroll's correlation [(41), page 162, Equation XVIII-2] as a function of consistency in the following form:

$$\bar{k} = 5.0 + \exp\left[14\left(0.20 - \overline{\Gamma} V_{sp}\right)\right] \qquad (52).$$

The only quantity which remains unknown in Equation (50) is the relative velocity.

Therefore, the equation can be solved, using the experimental velocity profile data, to obtain the relative velocity. The results of these calculations are summarized in Table VI. It will be recalled that the assumptions used in the development of Equation (50) require that the relative velocity between the fiber and water phases be small so that Darcy's law applies. The calculations

indicate that the relative velocities are small, the average being approximately -0.05 cm./sec. The relative velocities are therefore of at least a reasonable order of magnitude. Also, for a given suspension, there appears to be a tendency for the relative velocity to decrease with increasing flow rate as shown in Fig. 25. This result is expected in view of the observation that suspensions approach Newtonian behavior at high flow rates.

TABLE VI

CALCULATED RELATIVE VELOCITY IN FIBER SUSPENSION FLOW

Flow Rate, $ft.^3/sec.$	Consistency, g./100 ml.	K_*	Specific Resistance, $cm.^{-2}$	Relative Velocity, cm./sec.	$\bar{v}_*$, cm./sec.
0.117	0.041	0.314	800	-0.081	8.98
0.198	0.041	0.309	800	-0.057	14.38
0.067	0.119	0.269	6646	-0.077	5.51
0.114	0.119	0.300	6646	-0.056	8.58
0.205	0.119	0.317	6646	-0.0	14.63
0.068	0.122	0.275	6982	-0.060	5.49
0.090	0.122	0.300	6982	-0.035	7.01
0.114	0.123	0.307	7095	-0.029	8.54
0.080	0.185	0.252	15,878	-0.061	6.22
0.114	0.182	0.280	15,375	-0.057	8.45
0.154	0.183	0.300	15,542	-0.040	11.20
0.192	0.184	0.312	15,710	-0.017	13.74
0.114	0.254	0.250	29,575	-0.061	8.25
0.195	0.254	0.299	29,575	-0.034	13.75
0.114	0.358	0.238	56,469	-0.038	8.07
0.194	0.358	0.266	56,469	-0.056	13.25

As noted previously, the negative sign of the relative velocity indicates that the fibers have a greater net velocity than the water. Although this relative velocity was originally introduced as a local mean difference, it is now important to realize that the calculated value is the integral mean value across

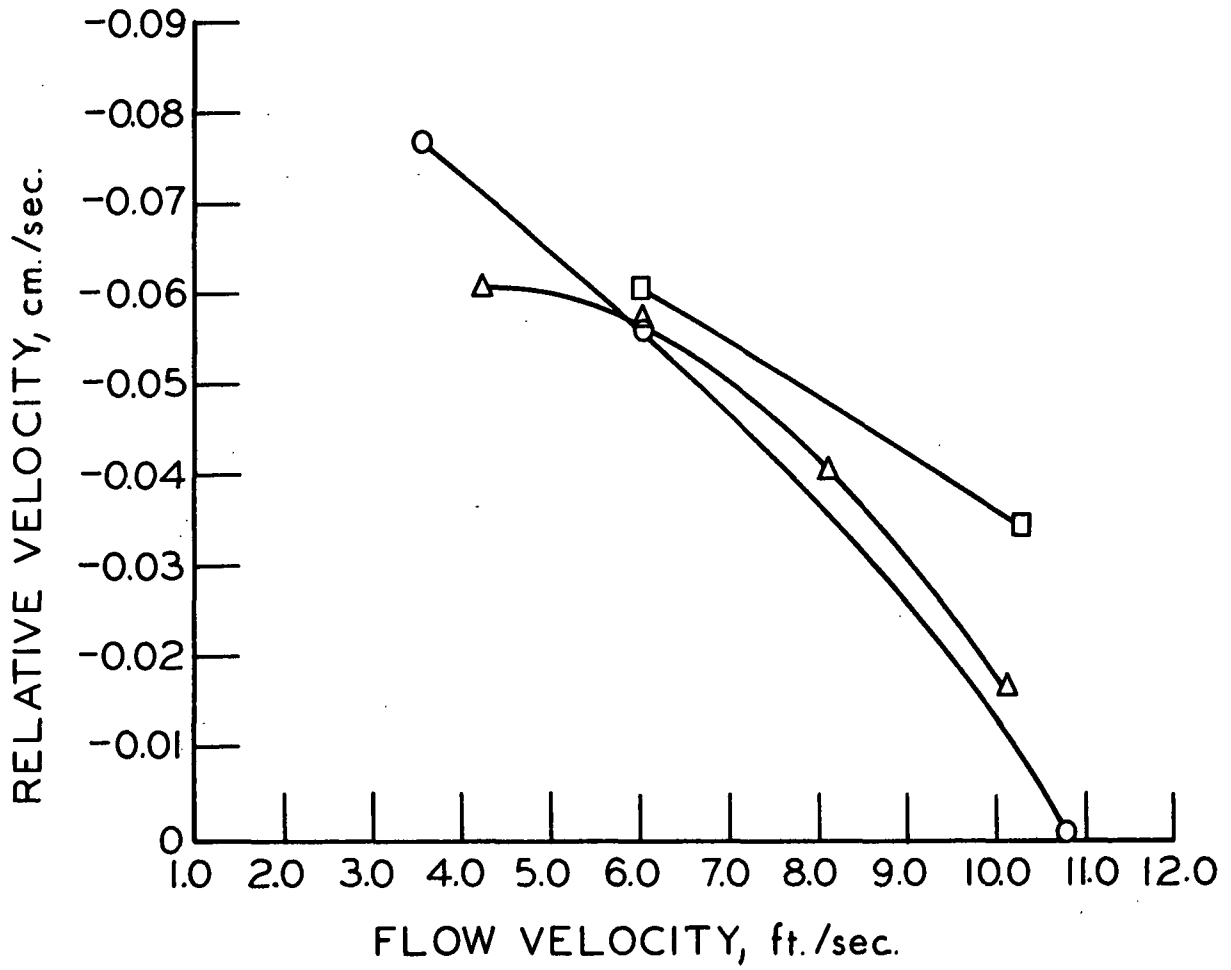

Figure 25. Relative Velocity vs. Flow Velocity

□ Cons., 0.254%

Δ Cons., 0.183%

O Cons., 0.122%

the pipe cross section as a consequence of the treatment in Equations (40) to (44). Therefore, a precise physical interpretation of this quantity is impossible at present. Several previous investigators (42,43) have measured the average velocity difference between particles and fluid for turbulent suspensions. These investigators found that the average particle velocity was greater than the average fluid velocity for suspensions of rigid, neutrally buoyant particles. These measurements were differences in discharge velocity and not differences in local mean velocity. In fact, the analysis used by these investigators included the assumptions that the local mean fluid and particle velocities were equal, and that the particle concentration was uniform across the pipe. Therefore, the results of these investigators do not clarify the physical interpretation of the local mean relative velocity found in this investigation. In fact, the particle concentration profiles reported in a later section cast some doubt on the validity of the assumption made by these investigators that the particle concentration was uniform across the pipe. Treatment of the local mean relative velocity will therefore have to be postponed until a reliable means of measurement of local particle and fluid velocities is developed. A recently developed laser doppler technique may be useful for particle velocity measurements (44).

It is now worthwhile to see how well Equation (50) predicts the shape of the velocity profile for fiber suspensions. Although it was shown that the relative velocity decreases with increasing flow rate, the exact relation between these quantities cannot be determined from the data. Therefore, an average value of -0.050 cm./sec. is used for calculations. This quantity, along with an experimentally determined friction velocity, can then be used in Equation (50) to

calculate the apparent von Karman constant for fiber suspensions. A comparison of the measured and calculated values of the apparent von Karman constant for fiber suspensions is presented in Table VII.

TABLE VII

COMPARISON OF CALCULATED AND MEASURED APPARENT VON KARMAN CONSTANTS

Flow Rate, $ft.^3/sec.$	Consistency, %	Measured K_*	Calculated K_*
0.117	0.041	0.314	0.315
0.198	0.041	0.309	0.316
0.067	0.119	0.269	0.280
0.114	0.119	0.300	0.300
0.205	0.119	0.317	0.311
0.068	0.122	0.275	0.278
0.090	0.122	0.300	0.292
0.114	0.123	0.307	0.299
0.080	0.185	0.252	0.257
0.114	0.182	0.280	0.281
0.154	0.183	0.300	0.294
0.192	0.184	0.312	0.301
0.114	0.254	0.250	0.254
0.195	0.254	0.299	0.289
0.114	0.354	0.238	0.217
0.194	0.354	0.266	0.267

These results indicate that the calculated apparent von Karman constants are in at least qualitative agreement with the measured values. The equation predicts that K_* decreases with increasing consistency and increases with increasing flow rate. The agreement between calculated and measured values of K_* is generally within about 5%.

It is now appropriate to make some general comments about Equation (50). The equation was developed from the equation of motion for a two-phase system in which each phase was assumed to be continuous. This assumption was necessary for the development of the equation of motion and for the application of Prandtl's mixing length concept. Another critical assumption was that only viscous drag forces were operating. It was assumed that the turbulent shear stresses exceeded any network tensile or shear strengths in order to omit consideration of the rheology of a fiber network. The assumptions inherent in using Prandtl's mixing length distribution were also included in the development of the velocity distribution expression. These assumptions were that the shear stress was constant; $\tau = \tau_o$ where τ_o = shear stress at the wall; and that the mixing length relationship at the wall could be applied to the entire turbulent core of the suspension. It is realized that some of the assumptions are rather far reaching and difficult to defend. However, they are necessary in order to determine a rational relationship between the Reynolds stresses and mean flow quantities. The primary support for this treatment is that it is very useful in the calculation of turbulent flows and allows one to deduce some of the fundamental physical ideas from the experimental measurements. The satisfactory agreement between theory and experimental results verifies the usefulness of this approach. Furthermore, it now appears that, under the conditions of this investigation, the viscous drag due to relative motion between the fibers and water accounts for most of the turbulence damping; hence, the lower von Karman constant for fiber suspensions.

CONSISTENCY PROFILES

Consistency profiles were measured over the same range of conditions as were the velocity profiles. Consistencies ranged from 0.041 to 0.470 g./100 ml.

and Reynolds numbers based on the water density and viscosity ranged from 5.2×10^4 to 1.6×10^5. As indicated previously, the profiles were time-mean measurements of the consistency at various radial positions across the pipe diameter.

Representative samples of the consistency profiles are presented in Fig. 26 and 27. All of the consistency profile data are tabulated in Appendix III. These profiles indicate that the fiber distribution in turbulent suspension flow is far from uniform across the pipe, and that the distribution varies with both flow rate and average consistency. Figure 26 shows that for a given flow rate the consistency profile becomes much sharper with increasing average consistency. Figure 27 demonstrates the change in consistency distribution with changes in flow rate. For a given suspension, the consistency profile becomes flatter with increasing flow rate. The tendency for the consistency distribution to become more uniform with increasing flow rate and decreasing average consistency was expected in view of the fact that the momentum transfer behavior of the suspension approaches the behavior of a Newtonian fluid at very high flow rates. The approach of the consistency profile to a constant and fairly uniform distribution at high flow rates is emphasized by the two profiles which are shown in Fig. 28. These two profiles at high but somewhat different flow rates are nearly identical. The velocity profile at this consistency and flow rate also approached a constant value, the apparent von Karman constant being essentially the same as the value for pure water. It therefore appears that at a high flow rate, depending on the consistency, both the consistency and normalized velocity distributions approach invariant values. This flow rate seems to be the minimum for uniformity of consistency distribution, and from then on the momentum transfer characteristics of the suspension become essentially the same as for a Newtonian fluid.

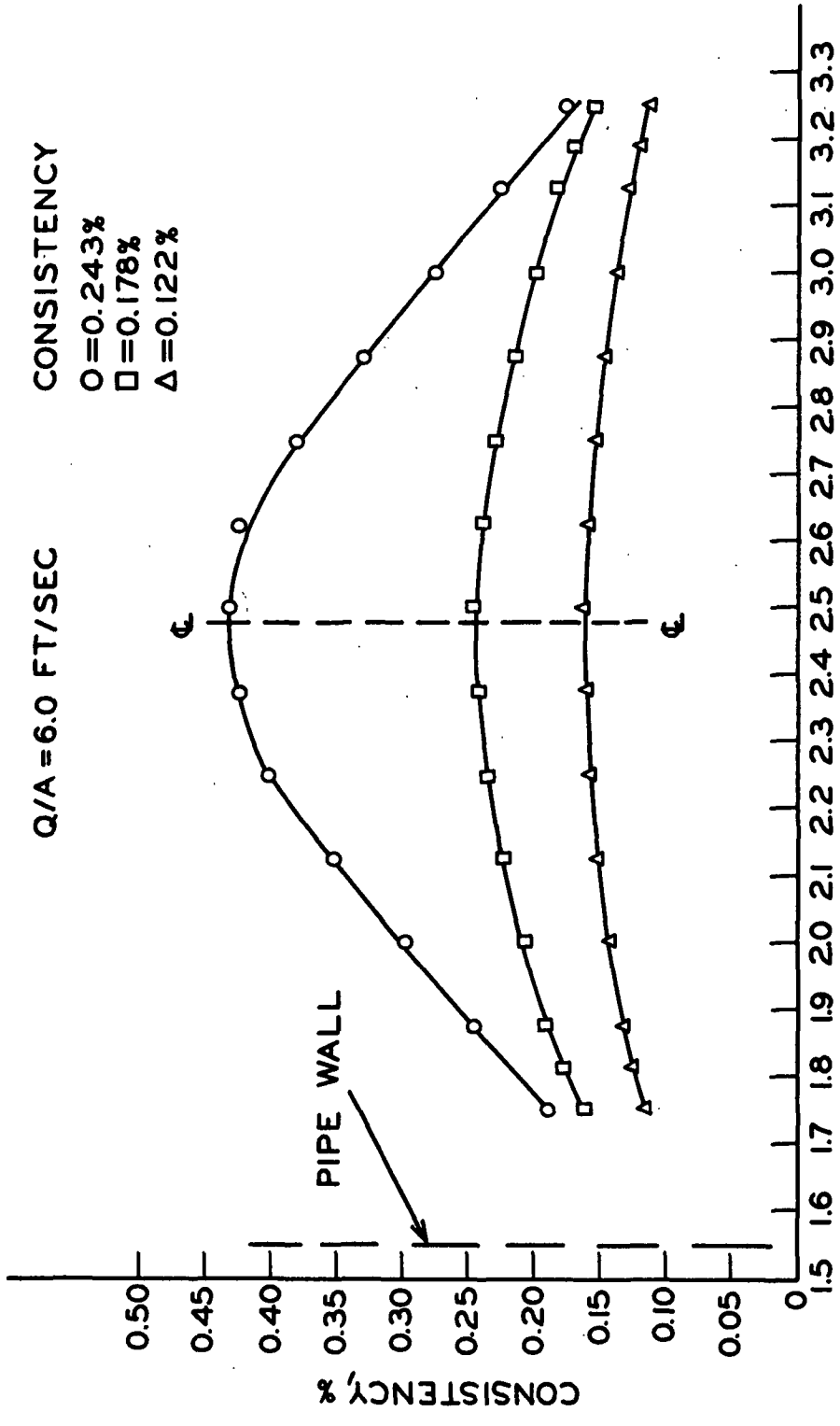

Figure 26. Consistency Profiles vs. Average Consistency

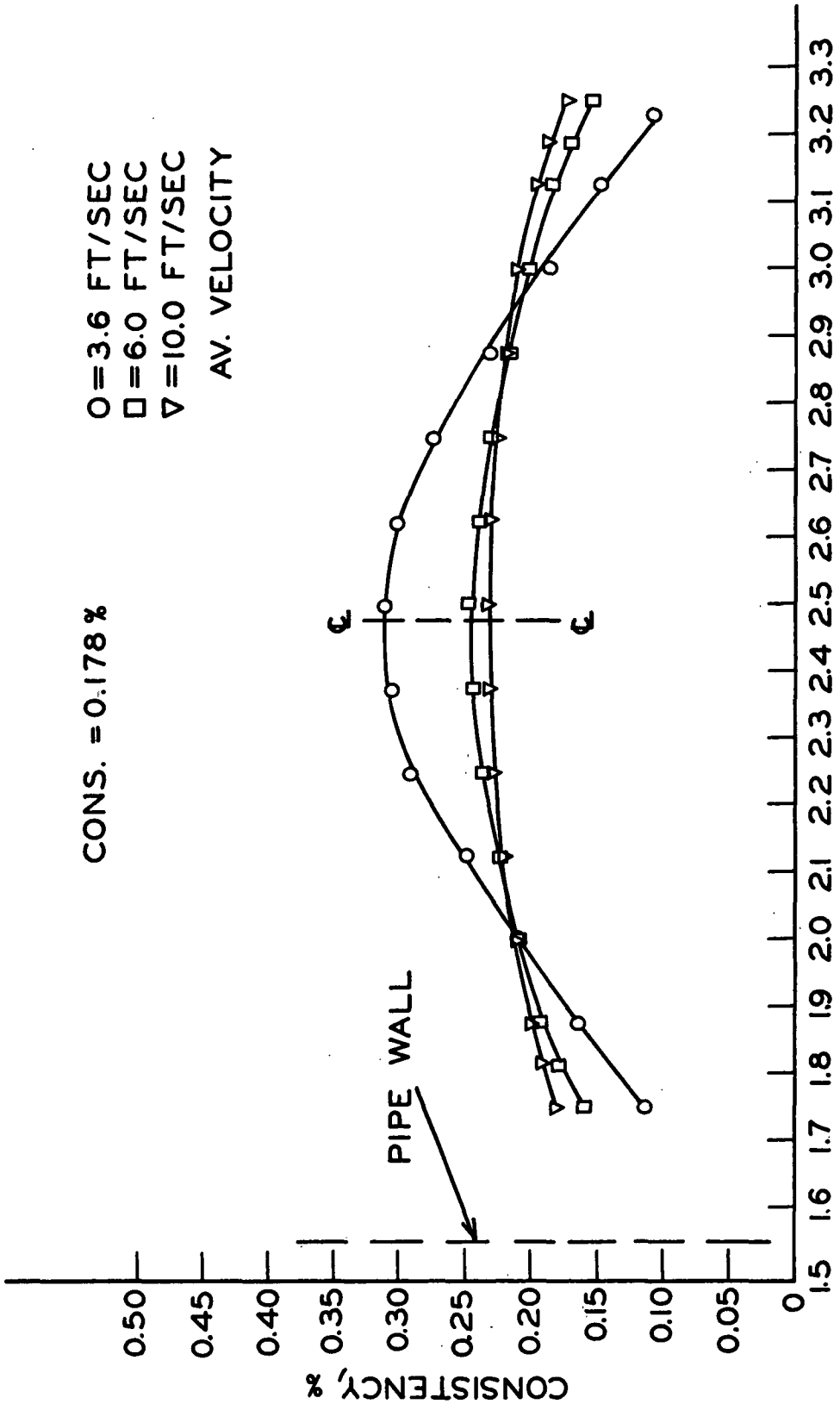

Figure 27. Consistency Profiles vs. Average Flow Rate

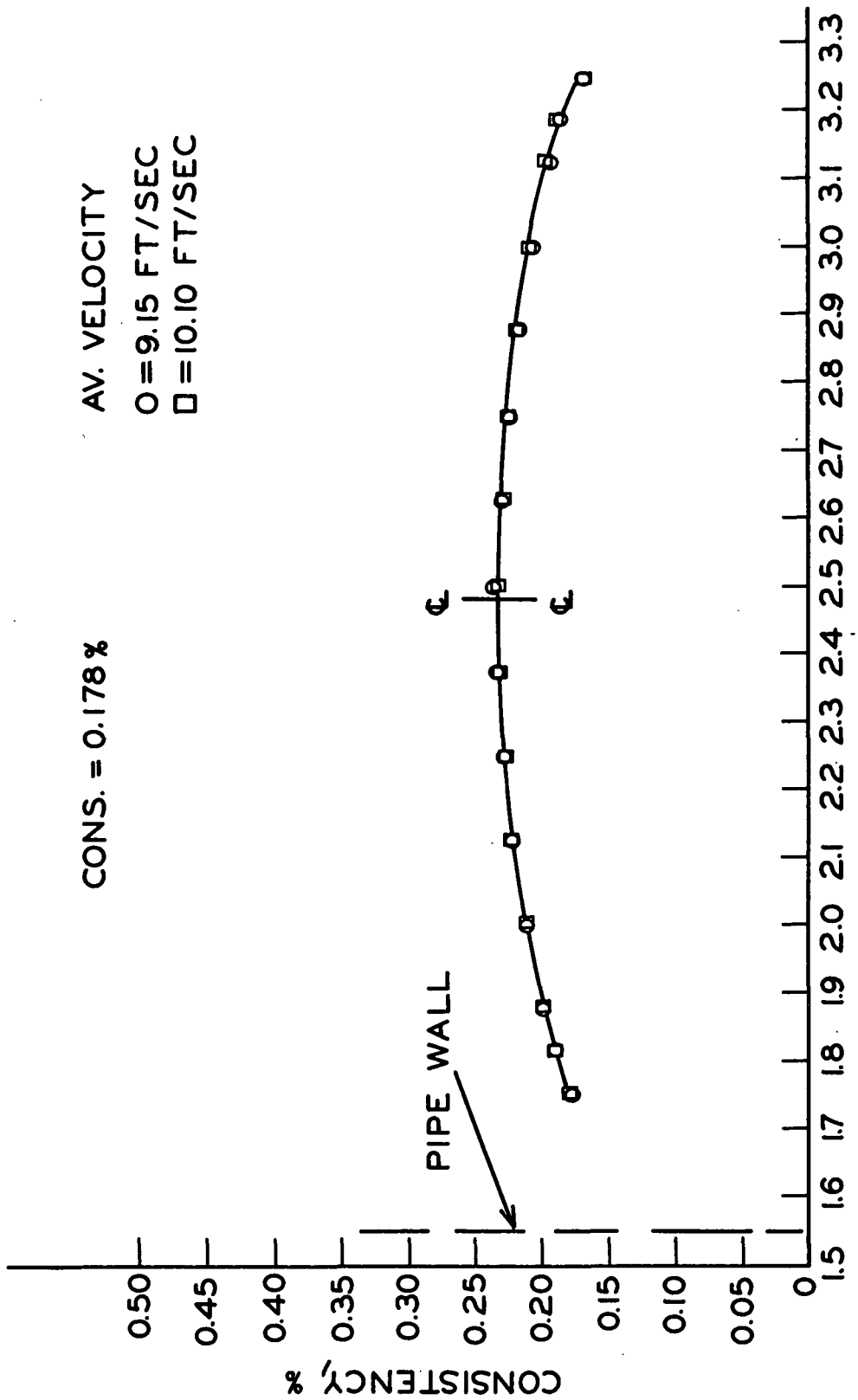

Figure 28. Approach of Consistency Profiles to an Equilibrium Value at High Flow Rates

The experimental consistency profiles can now be compared to Equation (34), which is shown below for convenience:

$$\ln\left(\frac{1-\bar{c}}{1-\bar{c}_o}\right) = -\frac{C_w}{\kappa_\varepsilon \kappa_w}\frac{\kappa_*}{v_*}\left(\ln s - \ln s_o\right) \tag{34}$$

Since the volume fraction of fibers at the boundary layer, $\bar{c}_o$, is very small, the term $1-\bar{c}_o$ will be taken as unity. Equation (34) then reduces to the following form, which is easily compared to the data:

$$\ln\left(1-\bar{c}\right) = -\frac{C_w}{\kappa_\varepsilon \kappa_w}\frac{\kappa_*}{v_*}\left(\ln s - \ln s_o\right) \tag{34a}$$

This equation predicts that $\ln(1-\bar{c})$ is a linear function of $\ln s$. The regression coefficient is a function of the velocity profile, characterized by κ_*; and a solid fraction exchange term, characterized by $C_w/\kappa_\varepsilon\kappa_w$. The validity of this equation was tested by correlating the experimental consistency profiles in the form $\ln(1-\bar{c})$ vs. $\ln s$. Representative examples of this type of consistency distribution correlation are shown in Fig. 29 through 33. The solid lines are the least squares best fit to the data, with the 95% confidence limits plotted as the broken lines. The agreement between the theory and data is excellent for most of the profiles. The profiles for "low" flow rates and "high" consistencies do deviate from the linear correlation to a significant extent. There are, however, several plausible explanations for the poorer agreement under these conditions. It should be recalled that the development of Equation (34) was simplified by neglecting a term containing the consistency gradient [Equations (27) to (29)]. This assumption is equivalent to stating that the consistency gradient across the pipe is small compared to the velocity gradient. Under most conditions, this

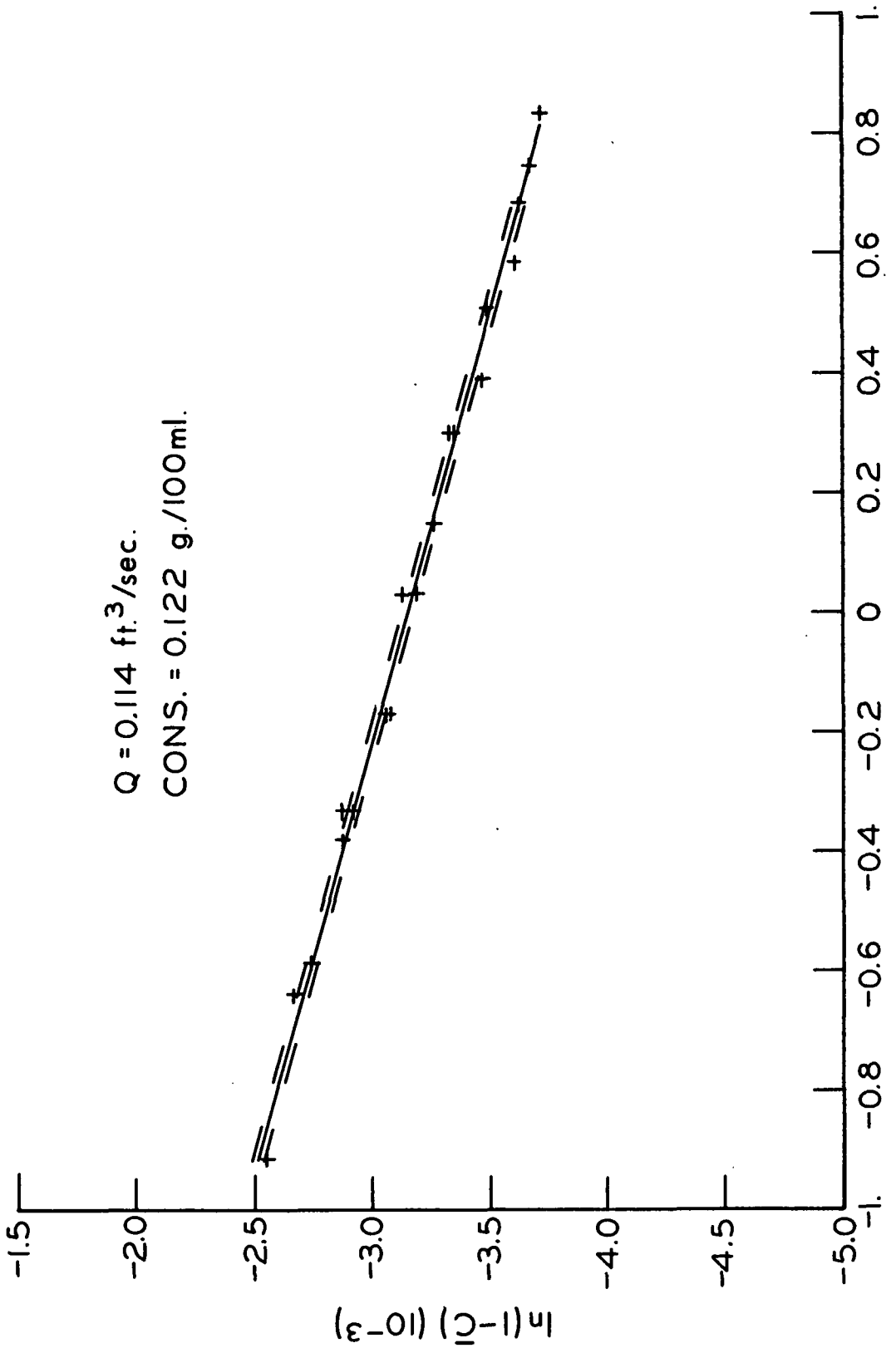

Figure 29. Logarithmic Consistency Distribution

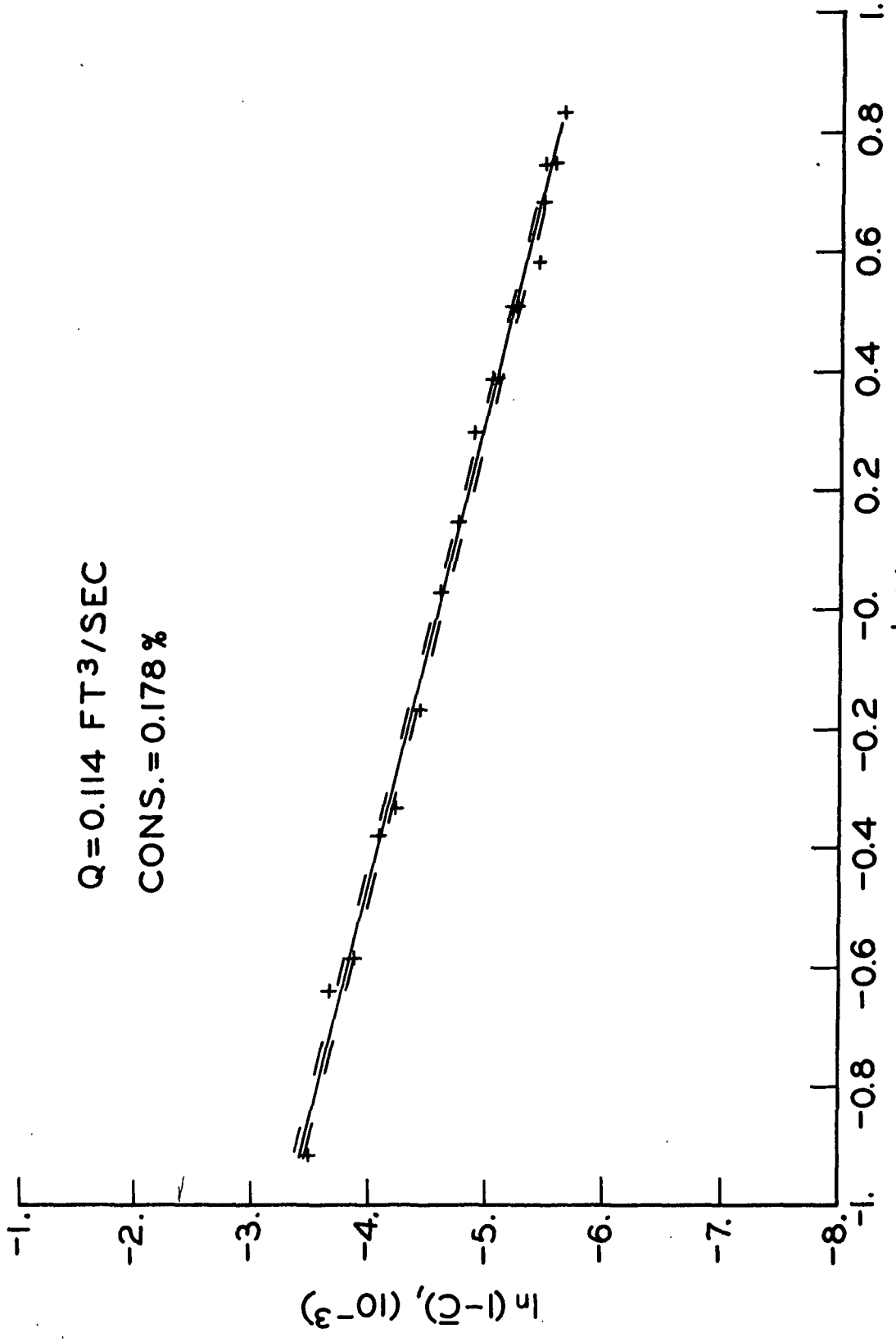

Figure 30. Logarithmic Consistency Distribution

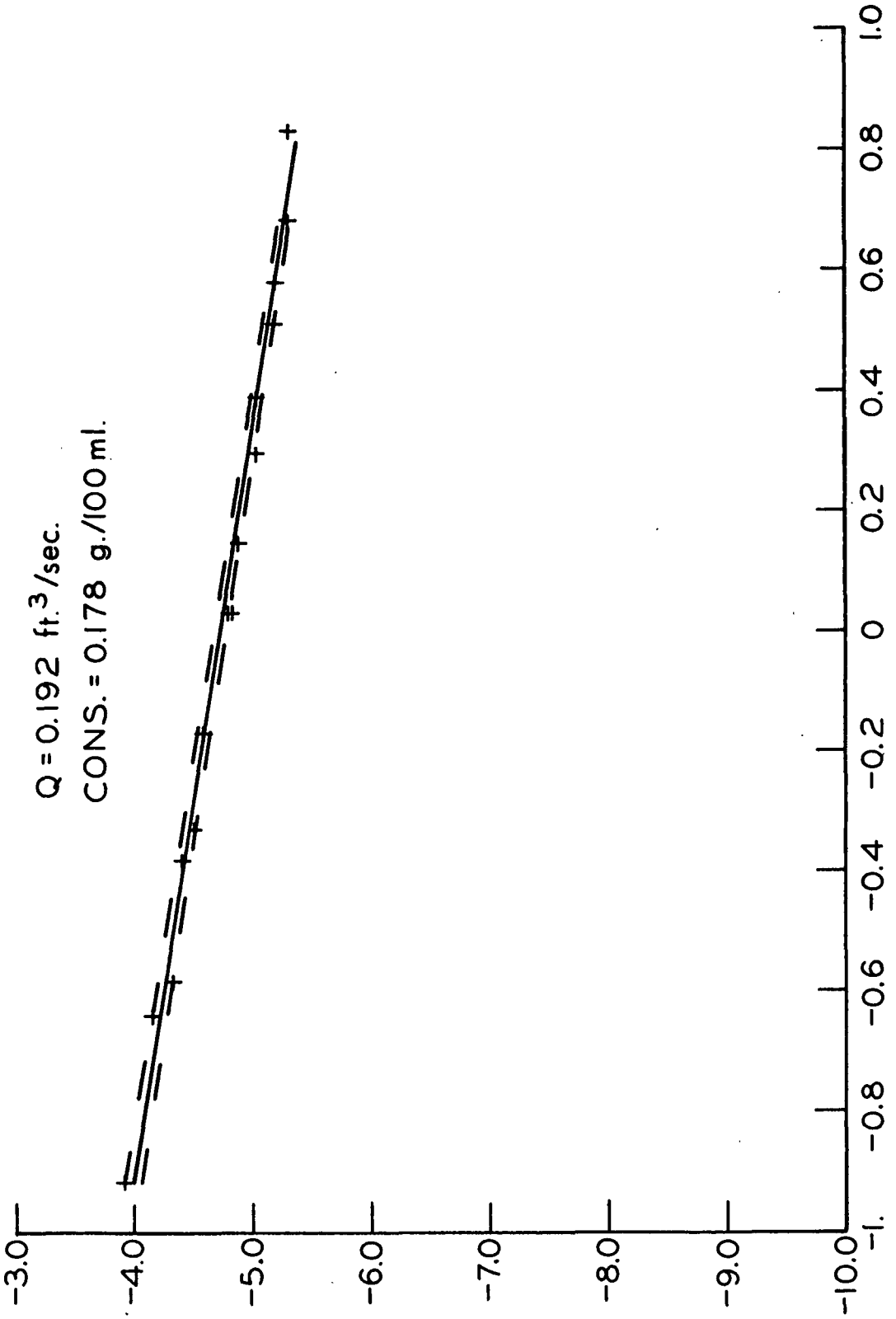

Figure 31. Logarithmic Consistency Distribution

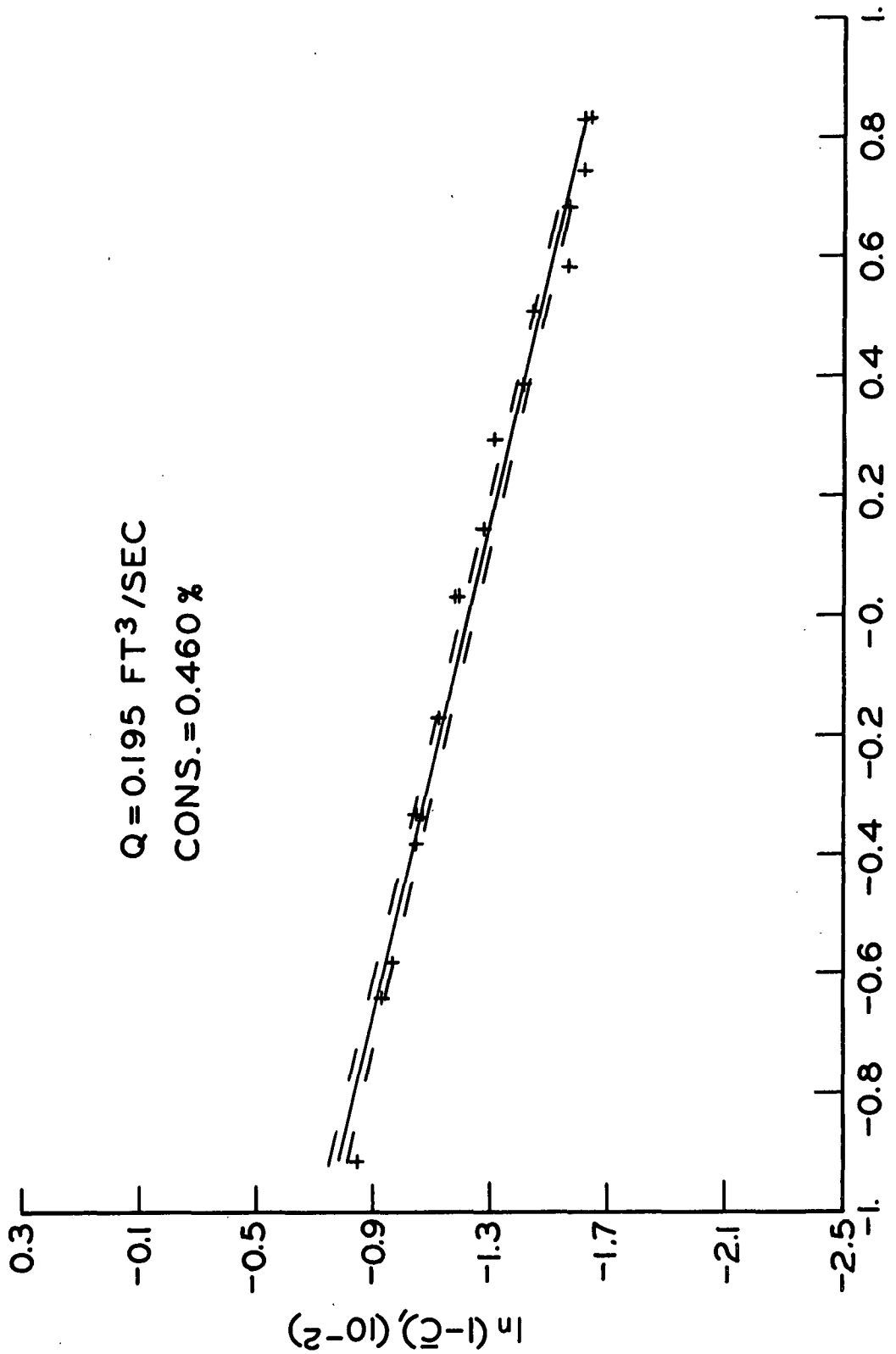

Figure 32. Logarithmic Consistency Distribution

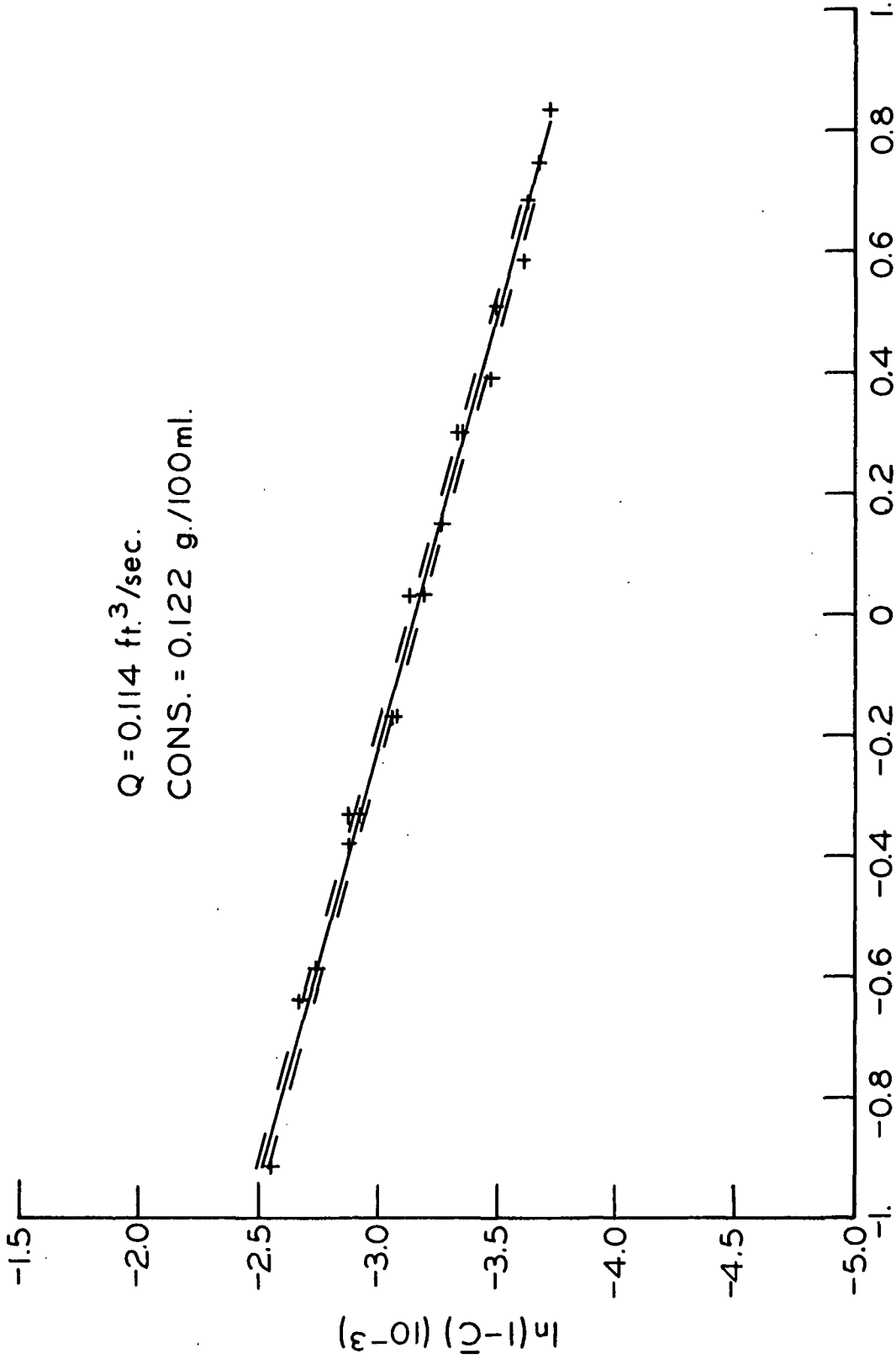

Figure 33. Logarithmic Consistency Distribution

assumption was apparently quite valid. However, at "low" flow rates and "high" consistencies, the consistency gradient is quite sharp as was shown in Fig. 26 and 27. Therefore, Equation (34) is not strictly valid under these conditions. Another possible reason for the poor fit at "low" flow rates and "high" consistencies is that the suspension is approaching the mixed or plug-turbulent flow regime.

Since both the apparent von Karman constant, κ_*, and the friction velocity, $\underline{v}_*$, are known for the suspensions, the solid fraction exchange term, $+ \underline{C}_w/\kappa_\varepsilon \underline{\kappa}_w$, and the fiber boundary-layer thickness, $\underline{s}_o$, may be evaluated from the slope and intercept of the consistency distribution correlations. Table VIII is a comparison of these parameters as a function of the flow rate and average consistency of the suspension. The data indicate that the solid fraction exchange term decreases with increasing flow rate and increases with increasing consistency. Because of the trends in the data, it is suggested that the solid fraction exchange term might be thought of as a flocculation index. However, an independent measure of the scale of flocculation as a function of position in the pipe would be necessary in order to determine the validity of this interpretation.

The data also indicate that the fiber boundary-layer thickness decreases with increasing flow rate and increases with increasing consistency. The trends in these data appear quite real. However, the exact numerical values should be viewed with some caution, especially the values for the "low" flow rates and "high" consistencies. The variation of $\underline{s}_o$ with flow rate and consistency appears quite reasonable in relation to the friction loss behavior if $\underline{s}_o$ may be assumed to be proportional to the thickness of the boundary layer of the water. With increasing flow rate, the boundary-layer thickness decreases, giving rise to a

higher velocity gradient at the wall, and thus a greater friction loss. With increasing consistency, the boundary-layer thickness increases, giving rise to a lower velocity gradient at the wall, and thus a smaller friction loss relative to pure water. These trends are reflected in the lower friction loss behavior of fiber suspensions as compared to water flow.

TABLE VIII

CONSISTENCY DISTRIBUTION PARAMETERS

Flow Rate, $ft.^3/sec.$	Consistency, g./100 ml.	κ_*	$\pm \underline{C}_w/\kappa\varepsilon\underline{K}_w$	$\underline{s}_o$, cm.
0.068	0.122	0.275	0.0303	0.124
0.090	0.122	0.300	0.0215	0.032
0.114	0.122	0.307	0.0196	0.011
0.205	0.122	0.317	0.0186	0.0001
0.068	0.178	--	--	0.243
0.114	0.178	0.280	0.0389	0.028
0.174	0.178	--	--	0.0048
0.192	0.178	0.312	0.0357	0.0029
0.114	0.243	0.250	0.126	0.174
0.196	0.243	0.299	0.0629	0.0084
0.114	0.358	0.238	0.210	0.227
0.193	0.358	0.266	0.121	0.0247
0.117	0.460	--	--	0.254
0.195	0.460	--	--	0.082

Although the consistency measurements used in this investigation were time-mean values, it is interesting to note that the consistency probe appears capable of measuring the fluctuating component of the consistency variations. An oscillogram of the measured light signal prior to time smoothing is shown in Fig. 34. This figure is included to indicate that the experimental technique and equipment described in this investigation may also be applicable to

a study of the time-dependent consistency variations. The limiting frequency response of the detection system was approximately 2100 c.p.s., which was more than adequate for accurate measurement of the approximately 100-c.p.s. signal.

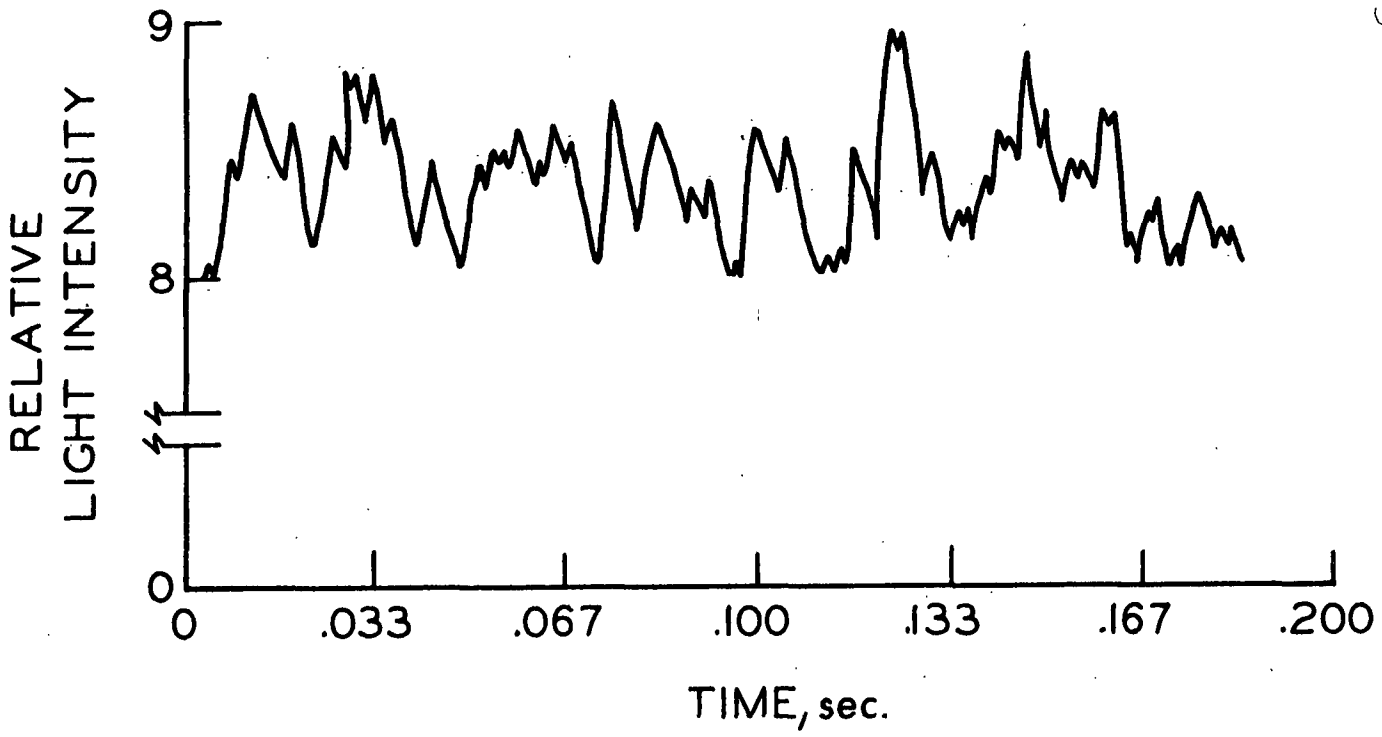

Figure 34. Oscillograph Trace of Undamped Signal from Consistency Probe (Probe at Center Line; Cons. = 0.365%; Chart Speed = 30 inches/sec.; Flow Velocity = 6.2 ft./sec.

SUMMARY OF RESULTS AND CONCLUSIONS

An experimental technique has been developed in this investigation for the measurement of fiber consistency distributions in a flowing suspension. The technique is applicable up to at least about 0.80 g./100 ml. consistency and appears to be the only method available for measuring local consistencies in a fiber suspension. The technique should be useful for concentration measurement in other dilute suspensions and slurries. There is also the possibility that the technique could be adapted for routine consistency measurements and control around the wet end of a paper machine.

The experimental results of this investigation represent the first successful attempt to measure time-mean consistency distributions in turbulent pipe flow of fiber suspensions. The consistency distribution, which in general increased from the wall to the center line, became more uniform with increasing flow rate and decreasing average consistency. The consistency distribution was found to be a strong function of both the flow rate and average consistency of the suspension. At a particular high flow rate dependent on the average consistency, the consistency distribution approaches an invariant profile. At these flow rates, the turbulent stresses apparently disperse the fibers to the point where the momentum transfer characteristics of the suspension are essentially the same as water.

The velocity distributions measured in this investigation indicate that the apparent von Karman constant for turbulent fiber suspensions is a function of both flow rate and average consistency. The von Karman constant increases systematically with increasing flow rate and at particular high flow rates dependent on the consistency approach the value for water flow. The flow rates

at which the apparent von Karman constant approaches the water value are also the minimum rates at which invariant consistency distribution profiles are obtained. At these flow rates the friction losses in suspension pipe flow also approach the water values.

The turbulent flow of fiber suspensions has been treated as a two-phase system by considering the coupled behavior of the fiber and water phases on the equations of continuity and motion. Each phase was treated as a quasi continuum. An equation which predicts the form of the consistency distribution [Equation (33)] was developed from one of the equations of continuity. This equation was derived by extending Prandtl's mixing length hypothesis in order to model the fluctuations in mass and velocity. The equation predicts a logarithmic relation between consistency and distance from the pipe wall. It also predicts that the consistency distribution is dependent on the velocity distribution. The equation fitted the experimental data very well. It can therefore be concluded that this analysis of the two-phase flow applying an extension of Prandtl's mixing length hypothesis is very useful in describing certain turbulent suspension flows.

Interpretation of the consistency distribution equation is primarily speculative. The local consistency fluctuations were assumed to be related via a mixing length to the consistency gradient across the channel as follows:

$$\left|\varepsilon'\right| = l_{\varepsilon} \left|\frac{d\bar{\varepsilon}}{ds}\right| \tag{53}$$

One might interpret the mixing length for mass exchange as follow: As the suspension moves in turbulent motion, fiber agglomerates are interchanged between lamina which are separated by a distance, l. This mixing length is the transverse distance a lump must travel in order to make the change in concentration equal to the mean transverse fluctuation in concentration. Based on

this interpretation and the observed trends in the data, it is suggested that the mass exchange term, $\underline{C}_{\underline{w}}/\kappa_{\varepsilon}\underline{\kappa}_{\underline{w}}$ (where $\kappa' = \underline{l}/\underline{s}$), may be useful as an index of the overall scale of flocculation for a turbulent suspension. The data showed that this term decreased with increasing flow rate and increased with increasing consistency.

An equation [Equation (50)] which relates the apparent von Karman constant to the average consistency, flow rate, fiber properties, and channel size was developed from one of the equations of motion for two-phase flow. The equation accounted for drag between the two phases arising from relative flow between the fibers and water by assuming only viscous resistance is important and applying Darcy's equation. The equation was found to correlate the data satisfactorily and predicted an increase in κ_* with increasing flow rate and a decrease in this constant with increasing average consistency.

This two-phase analysis of the turbulent flow of fiber suspensions emphasizes the need for understanding the behavior of each phase and their interrelation if one is to develop a more meaningful knowledge of suspension flow. Some suspensions may not be successfully treated as homogeneous mixtures or single-phase systems as has been assumed in the past. Suspensions in general are two-phase systems and should be treated as such. However, the particular type of two-phase treatment used in this investigation may not be applicable to all suspensions. The equations used in this investigation were developed assuming that <u>each</u> phase could be treated as a continuum. It is not at all certain under what conditions this assumption is valid. It seems probable that the solid phase of certain suspensions (such as dilute suspensions of rigid spheres) may not be treated as a continuum. Further work is necessary in order to understand the properties and treatment required for a description of most suspensions.

As a sidelight of the experimental program, it was found that the entrance or approach geometry of turbulent pipe flow systems is critical to the development of fully developed velocity profiles. Smoothly curved entrances to straight pipe flow sections apparently create stable secondary flow patterns which delay the development of velocity profiles. Sharp-angled entrances to a straight flow section do not create stable secondary flow patterns and are preferred for obtaining fully developed velocity profiles.

SUGGESTIONS FOR FUTURE WORK

There is opportunity and need for considerable additional work on the flow of fiber suspensions.

In particular, it would be most useful to investigate the time-dependent consistency variations in various specified fields of flow. This information would be very valuable in controlling the uniformity of the sheet-forming process. This information, along with local turbulence measurements, might also allow one to develop a reasonable understanding of the mechanism of turbulence damping.

Additional time-mean consistency measurements in the plug flow regime would be worthwhile. This might allow an explanation of why the shear stress at the plug boundary varies with the plug radius.

There is also the possibility of extending the consistency profile data to include different fiber types and different pipe sizes. An investigation of the consistency distribution under nonsteady-state conditions would also be a reasonable program.

No less important would be the study of both consistency and velocity profiles very close to the wall in pipe flow. The flow behavior in this region is what ultimately controls the pressure loss behavior.

NOMENCLATURE

$\underline{A}$ = cross-sectional area of pipe

$\underline{a}$ = viscous flow resistance coefficient

$\underline{\bar{a}}$ = time-mean viscous flow resistance coefficient

$\underline{B}$ = constant

$\underline{C_f}$, $\underline{C_w}$ = integration constants

$\underline{C'_w}$ = $\underline{C_w}/\underline{R}$

$\underline{c}$ = volume fraction of fibers

$\underline{\bar{c}}$ = time-mean volume fraction of fibers

$\underline{D_i}$ = drag force per unit volume of mixture

exp = exponential function

$\underline{F_i}$ = component of body force per unit volume of mixture

$\underline{f}$ = friction factor

$\underline{g_i}$ = gravitational acceleration in direction of $\underline{x_i}$ component

$\underline{h}$ = 1/2 channel thickness

$\underline{i}$, $\underline{j}$ = subscripts denoting Cartesian coordinates

$\underline{k}$ = Kozeny factor

$\underline{l_f}$ = mixing length for momentum transport of fibers

$\underline{l_w}$ = mixing length for momentum transport of water

$\underline{l_\varepsilon}$ = mixing length for mass exchange

$\underline{p}$ = total pressure

$\underline{p_F}$ = true fiber pressure

$\underline{p_f}$ = apparent fiber pressure

$\underline{p_W}$ = true water pressure

$\underline{p}_{\underline{w}}$ = apparent water pressure

$\underline{Q}$ = volumetric flow rate of suspension

$\underline{R}$ = pipe radius

$\underline{Re}$ = Reynolds number

$\underline{r}$ = radial position in pipe flow

$\underline{S}_{\underline{sp}}$ = hydrodynamic specific surface of fibers

$\underline{s}$ = wall distance

$\underline{s}^{+}$ = dimensionless wall distance, $\underline{s}\rho\underline{v}_{*}/\mu$

$\underline{s}_{o}$ = fiber-free boundary layer thickness

$\underline{t}$ = time

$\underline{V}^{+}$ = dimensionless velocity, $\underline{v}/\underline{v}_{*}$ or $\bar{\underline{V}}_{\underline{w}}/\underline{v}_{*}$

$\underline{V}_{\underline{sp}}$ = hydrodynamic specific volume of fibers

$\underline{V}_{\underline{w}}$, $\underline{V}_{\underline{f}}$ = superficial water and fiber velocities, respectively

$\underline{v}_{\underline{f}}$ = velocity of fiber phase

$\underline{v}_{\underline{rz}}$ = relative velocity between water and fiber phases, $\overline{\underline{v}_{\underline{w}}-\underline{v}_{\underline{f}}}$

$\underline{v}_{\underline{w}}$ = velocity of water phase

$\underline{v}_{*}$ = friction velocity, $\sqrt{\tau_{o}/\rho}$

$\underline{x},\underline{y},\underline{z}$ = Cartesian coordinates

Γ = weight percent of fibers in suspension

ε = volume fraction of water

κ = von Karman constant

$\kappa_{\varepsilon}\kappa_{\underline{w}}$ = mixing length distribution parameters for water and fiber, resp.

κ_{*} = apparent von Karman constant for fiber suspensions

μ = viscosity

ρ = density of mixture

$\rho_{\underline{F}}$ = true density of fibers

$\rho_{\underline{W}}$ = true density of water

$\tau_{\underline{ij}}$ = stress tensor

τ_o = shear stress at wall

ACKNOWLEDGMENTS

Sincere thanks are due to Mr. Heribert Meyer, Chairman of my Advisory Committee, for his guidance, encouragement, and criticism throughout the course of this investigation. I would especially like to acknowledge his major contributions to the theoretical portion of this study. The advice and encouragement of the other members of the committee, Dr. J. P. Brezinski and Dr. Thomas M. Grace, are also greatly appreciated.

I would also like to thank Dr. Joseph D. Parker of Beloit Corporation for generously sharing experiences with an annular-purge optical probe, which was the basis for the design used in this investigation.

The entire Institute staff has been most helpful. Special thanks are due Mr. Orlin Kuehl and Mr. Keith Hardacker for help in designing and building equipment. The continued help and advice of Mr. Bruce Andrews was also most valuable. Thanks to Mrs. E. A. Cary for the careful typing and proofreading of this manuscript.

Finally, sincere thanks to my wife, Linda, for her encouragement and patience through the course of this investigation.

LITERATURE CITED

1. Forrest, F. R., and Grierson, G. A. H., Tech. Assoc. Papers 14:259(1931).
2. Peterson, C. W., Svensk Papperstid. 52:371 (1949).
3. Brecht, W., and Heller, H., Tappi 33, no. 9:14A (1950).
4. Durst, R., and Jenness, L., Tappi 37:417 (1954).
5. Robertson, A. A., and Mason, S. G., Tappi 40:326 (1957).
6. Forgacs, O. L., Robertson, A. A., and Mason, S. G., Pulp Paper Mag. Can. 59:117 (1958).
7. De Roos, A. J., Tappi 41:354 (1958).
8. Guthrie, W. E., Tappi 42:232 (1959).
9. Baines, W. D., Tappi 40:407 (1957).
10. Baines, W. D., Svensk Papperstid. 62:823 (1959).
11. Daily, J., and Bugliarello, G., Tappi 44:497, 881 (1961).
12. Raij, U., and Wahren, D., Svensk Papperstid. 67:186 (1964).
13. Bobkowicz, A. J., and Gauvin, W. H., Can. J. Chem. Eng. 43:87 (1965).
14. Bobkowicz, A. J., and Gauvin, W. H., Chem. Eng. Sci. 22:229 (1967).
15. Maj, J., and Szwarcsztajn, E., Przeglad Papier. 22, no. 6:181 (1966).
16. Mih, W., and Parker, J., Tappi 50:237 (1967).
17. Giese, E., and Janke, H., Cellulose Chem. Technol. 1:471 (1967).
18. Seely, T. Turbulent tube flow of dilute fiber suspensions. Doctoral Dissertation. Appleton, Wis., The Institute of Paper Chemistry, 1968.
19. Meyer, H., Tappi 47, no. 2:78 (1964).
20. Wrist, P. E. Flow properties of fibrous suspensions. In Marchessault and Shaar's Surfaces and coatings related to paper and wood. New York, Syracuse University Press, 1967.
21. Van den Akker, J. A., Tappi 37:489 (1954).
22. Daily, J. W., Bugliarello, G., and Troutman, W. W. M.I.T. Hydrodynamics Laboratory Report No. 35. Cambridge, Mass., Massachusetts Institute of Technology, 1959.

23. Quarterly Progress Report No. 28 (Supplement), Post Graduate Research (Jan. 1, 1966-March 31, 1966), Pulp and Paper Research Institute of Canada, Pointe Claire, P.Q., April, 1966.

24. Schlichting, H. In Boundary layer theory. 4th ed. Chap. XIX. New York, McGraw-Hill, 1960.

25. Virk, P. S., Merrill,E. W., Mickley, H. S., Smith, K. A., and Mollo-Christensen, E. L., J. Fluid Mech. 30:305 (1967).

26. Ernst, W. D., A.I.Ch.E. Journal 12:581 (1966).

27. Shaver, R. G., and Merrill, E. W., A.I.Ch.E. Journal 5:181 (1959).

28. Hoyt, J. W., Chem. Soc. (London) Special Publ. 23:207 (1968).

29. Dodge, D. W., and Metzner, A. B., A.I.Ch.E. Journal 5:189 (1959).

30. Wells, C. S., A.I.Ch.E. Journal 3:1800 (1965).

31. Thomas, D. G., A.I.Ch.E. Journal 8:631 (1962).

32. Tesarik, I., Trans. Inst. Chem. Engrs. 43:317 (1965).

33. Daily, J. W., and Roberts, P. R., Tappi 49:115 (1966).

34. Hino, M., J. Hydraulics Div., Proc. Am. Soc. Civ. Engrs. 89, no. HY4 (July, 1963).

35. Bird, R. B., Stewart, W. E., and Lightfoot, E. N. Transport phenomena. New York, John Wiley and Sons, Inc., 1966.

36. Deissler, R. G., NACA Tech. Note 2138, 1950.

37. Segre, G., and Silberberg, A., J. Fluid Mech. 14:115 (1962).

38. Maude, A. D., and Yearn, J. A., J. Fluid Mech. 30:601 (1967).

39. du Plessis, M. P., Trans. Eng. Inst. Can., Paper no. E1C-66-Mech., 1966.

40. Parker, J. D. (Beloit Corp.). Private communication.

41. Han, S. T. The status of the sheet-forming process — a critical review. Chap. III, XVIII. Appleton, Wis., The Institute of Paper Chemistry, 1965.

42. Batchelor, G. K., Binnie, A. M., and Phillips, O. M., Proc. Phys. Soc. London B 68:1095-1104.

43. Roberts, C. P. R., Kennedy, J. F., and Ippen, A. T., M.I.T. Hydrodynamics Laboratory Report No. 102. Cambridge, Mass., Massachusetts Institute of Technology, 1967.

44. Angus, J. C., Morrow, D. L., Dunning, J. W., and French, M. J., Ind. Eng. Chem. 67, no. 2:8-20 (1969).

APPENDIX I

LIGHT SOURCE AND POWER SUPPLY

Investigations of consistency measurements based on light measurements require a stable light source and power supply. Figure 35 shows the light source designed and built for use with the light-guide consistency probe. A Model 1960 G. E. quartz-iodine lamp mounted on a heat-resistant lamp holder, C, is held in the lamp housing, D, by three set screws. A spacer sleeve, B, positions the cover plate containing the light-guide socket, A, a fixed distance from the lamp. The cover plate and spacer sleeve are spring loaded against the lamp holder by two externally mounted tension springs. This arrangement assures a fixed geometry between the lamp and tip of the light guide. The quartz-iodine lamp is stable and does not blacken provided the voltage is maintained at about 10.0 volts. The lamp temperature should be maintained between 250 and 750°C. However, the lamp base should not exceed 350°C.

Figure 36 is a schematic of the d.c. power supply. It is simply an RC-filtered supply with a rather large capacitance. There was no detectable ripple in the light source using this power supply. A Sorensen regulator was used to control the line voltage.

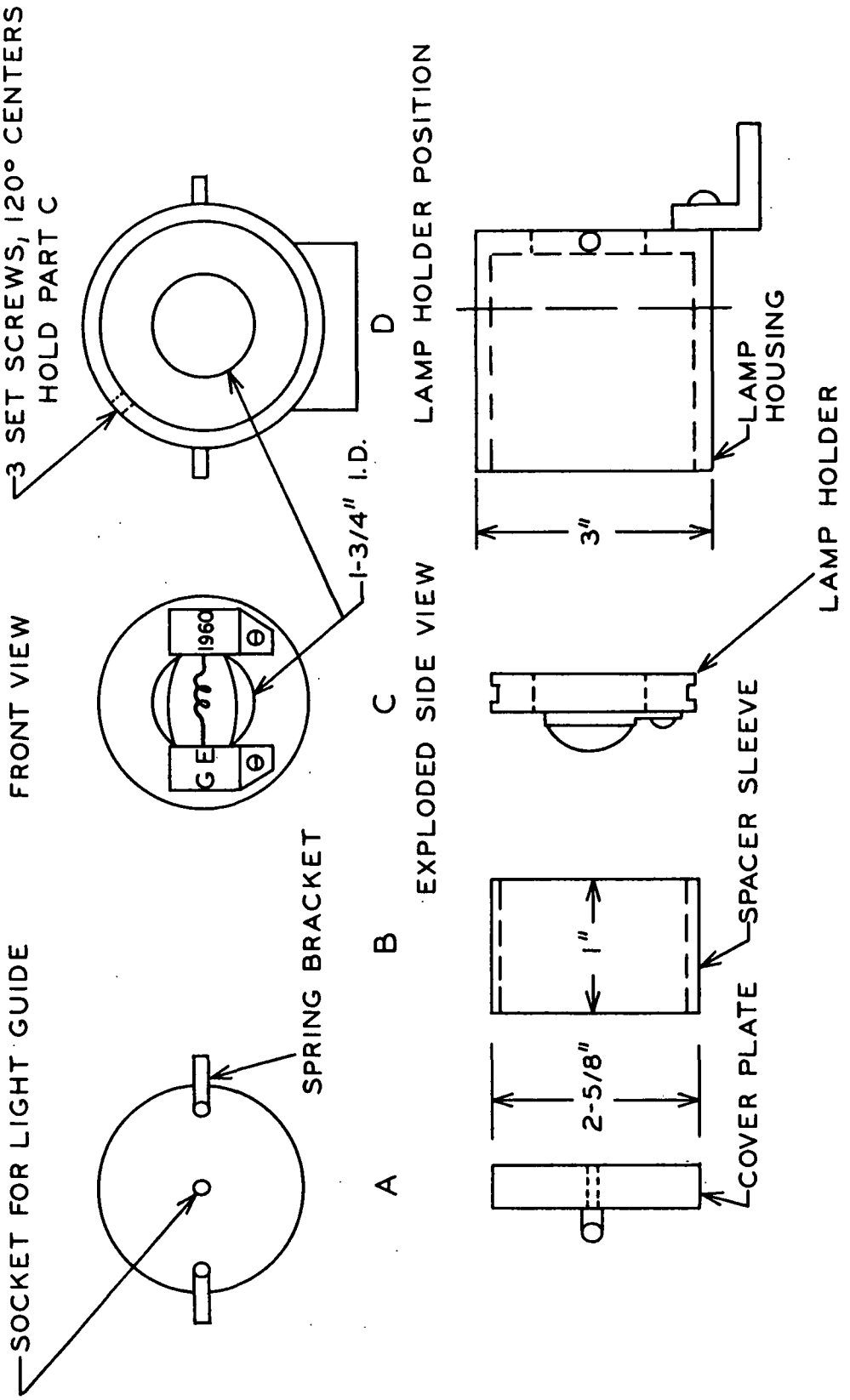

Figure 35. Light Source

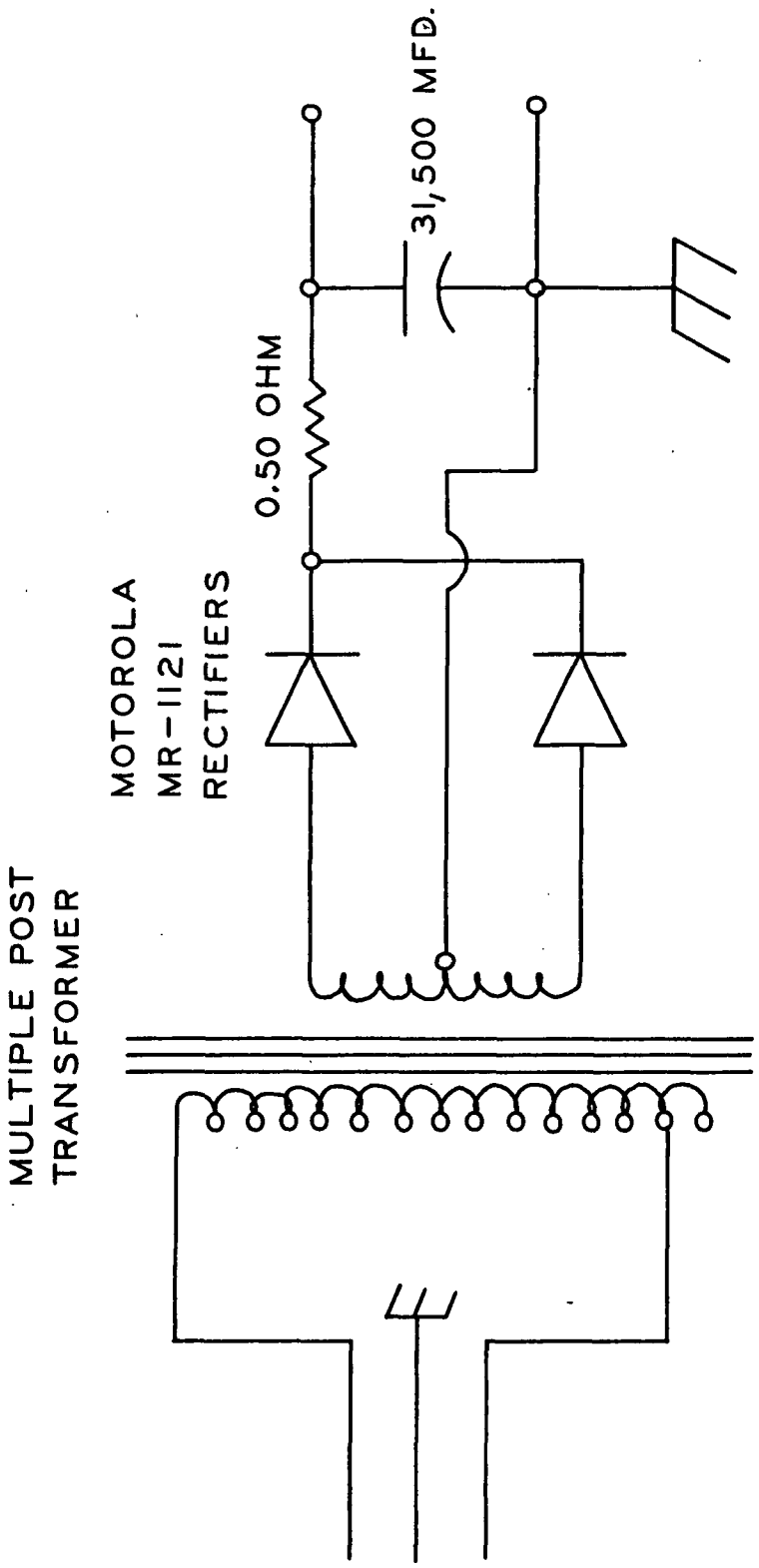

Figure 36. D.C. Power Supply (6 to 11 Volts, 7 Amperes)

APPENDIX II

VELOCITY PROFILE DATA

The velocity profile data are tabulated below in sufficient detail to allow the reader to perform all calculations used in the text. All data were taken in the 1.865-in. i.d. pipe loop. The consistency, Cons., is reported in percent for each profile as well as the flow rate, Q, The static pressure drop, DHP, is reported in cm. CCl_4/H_2O, and the viscosity of water at the temperature of operation is reported in centipoises. The distance between static pressure taps was 224 cm. The impact pressure, DHIP, is reported in cm. CCl_4/H_2O. The calculated values for the reduced position, SPLUS, and the reduced velocity, VPLUS, are included for convenience. The apparent von Karman constant, KAPPA, is also given for each velocity profile.

Run No. 012369

Cons. = 0.0 Q = 0.090 cu.ft./sec.
DHP = 16.55 cm. Visc. = 0.96 cp.

Radius, in.	DHIP, cm.	SPLUS	VPLUS
0.005	26.10	1745.6	24.3
0.120	25.75	1529.3	24.2
0.245	24.90	1294.2	23.8
0.370	23.50	1059.1	23.1
0.495	21.75	824.0	22.2
0.620	19.60	588.9	21.1
0.682	18.40	472.2	20.4
0.745	16.75	353.7	19.5
0.800	14.90	250.3	18.4
0.130	25.80	1510.5	24.2
0.380	23.40	1040.3	23.1
0.630	19.40	570.1	21.0
0.755	16.30	334.9	19.2
0.810	14.60	231.5	18.2

Kappa = 0.313

Run No. 012960

Cons. = 0.0 Q = 0.190 cu.ft./sec.
DHP = 61.70 cm. Visc. = 0.94 cp.

Radius, in.	DHIP, cm.	SPLUS	VPLUS
0.005	113.40	3442.2	26.3
0.120	112.25	3015.7	26.2
0.245	108.75	2552.1	25.7
0.370	103.55	2088.4	25.1
0.495	96.00	1624.8	24.2
0.620	87.15	1161.2	23.0
0.745	76.50	697.6	21.6
0.800	68.40	493.6	20.4
0.255	108.65	2515.0	25.7
0.380	102.95	2051.4	25.0
0.505	95.50	1587.7	24.1
0.630	86.50	1124.1	23.0
0.755	74.60	660.5	21.3
0.810	67.25	456.5	20.2

Kappa = 0.317

Run No. 012969

Cons. = 0.0 $\underline{Q}$ = 0.090 cu.ft./sec.
DHP = 17.15 cm. Visc. = 0.98 cp.

Radius, in.	DHIP, cm.	SPLUS	VPLUS
0.005	26.55	1740.7	24.1
0.120	26.25	1525.0	24.0
0.245	25.30	1290.6	23.6
0.370	23.80	1056.1	22.8
0.495	22.10	821.7	22.0
0.620	19.80	587.2	20.8
0.682	18.40	470.9	20.1
0.745	17.00	352.8	19.3
0.800	15.25	249.6	18.3

Kappa = 0.317

Run No. 020569

Cons. = 0.0 $\underline{Q}$ = 0.107 cu.ft./sec.
DHP = 22.60 cm. Visc. = 1.04 cp.

Radius, in.	DHIP, cm.	SPLUS	VPLUS
0.050	36.85	1791.7	24.8
0.175	36.00	1538.1	24.5
0.300	34.25	1284.5	23.9
0.425	32.05	1030.8	23.1
0.550	29.55	777.2	22.2
0.675	25.90	523.6	20.8
0.800	21.20	270.0	18.8
0.847	18.45	174.6	17.5
0.075	36.70	1741.0	24.7
0.200	35.60	1487.3	24.3
0.325	33.65	1233.7	23.7
0.575	28.45	726.5	21.8
0.700	24.85	472.9	20.3
0.841	18.90	186.8	17.7

Kappa = 0.313

Run No. 080769

Cons. = 0.0 $\underline{Q}$ = 0.180 cu.ft./sec.
DHP = 58.45 cm. Visc. = 1.00 cp.

Radius, in.	DHIP, cm.	SPLUS	VPLUS
0.115	103.80	2776.1	25.8
0.240	100.30	2351.9	25.4
0.365	94.85	1927.7	24.7
0.490	87.75	1503.5	23.8
0.615	79.70	1079.3	22.6
0.740	69.20	655.2	21.1
0.802	61.10	444.8	19.8
0.010	104.80	3132.4	26.0
0.135	103.40	2708.2	25.8
0.260	99.20	2284.0	25.3
0.385	93.60	1859.8	24.5
0.510	86.10	1435.7	23.5
0.635	77.80	1011.5	22.4
0.760	66.95	587.3	20.8
0.822	58.25	376.9	19.4

Kappa = 0.307

Run No. 081069

Cons. = 0.0 $\underline{Q}$ = 0.090 cu.ft./sec.
DHP = 17.40 cm. Visc. = 1.01 cp.

Radius, in.	DHIP, cm.	SPLUS	VPLUS
0.115	25.40	1499.6	23.4
0.240	24.50	1270.5	23.0
0.365	23.15	1041.4	22.4
0.490	21.40	812.2	21.5
0.615	19.05	583.1	20.3
0.740	16.55	353.9	18.9
0.802	14.35	240.3	17.6
0.010	25.70	1692.1	23.6
0.135	25.25	1463.0	23.4
0.260	24.10	1233.8	22.8
0.385	22.70	1004.7	22.1
0.510	20.65	775.6	21.1
0.635	18.40	546.4	19.9
0.760	15.35	317.3	18.2
0.822	13.30	203.6	17.0

Kappa = 0.310

Run No. 021969

Cons. = 0.190 $\underline{Q}$ = 0.096 cu.ft./sec.
DHP = 17.35 cm. Visc. = 1.01 cp.

Radius, in.	DHIP, cm.	SPLUS	VPLUS
0.030	29.65	1653.1	25.3
0.095	29.35	1534.1	25.2
0.220	28.65	1305.3	24.9
0.345	27.00	1076.5	24.2
0.470	25.10	847.7	23.3
0.595	22.65	618.8	22.2
0.720	19.40	390.0	20.5
0.840	14.50	170.4	17.7
0.155	29.15	1424.3	25.1
0.280	27.90	1195.5	24.6
0.405	26.30	966.6	23.9
0.530	23.90	737.8	22.8
0.655	21.40	509.0	21.5
0.780	17.75	280.2	19.6
0.811	15.90	223.5	18.6

Kappa = 0.289

Run No. 080769

Cons. = 0.0 $\underline{Q}$ = 0.090 cu.ft./sec.
DHP = 17.25 cm. Visc. = 1.00 cp.

Radius, in.	DHIP, cm.	SPLUS	VPLUS
0.010	25.25	1701.7	23.5
0.115	24.90	1508.1	23.3
0.240	24.10	1277.7	22.9
0.365	22.80	1047.2	22.3
0.490	20.80	816.8	21.3
0.615	18.60	586.4	20.1
0.677	17.35	472.1	19.4
0.740	15.80	355.9	18.6
0.802	14.15	241.6	17.6
0.833	12.65	184.5	16.6
0.135	24.85	1471.2	23.3
0.260	23.85	1240.8	22.8
0.385	22.30	1010.4	22.0
0.510	20.50	779.9	21.1
0.635	18.35	549.5	20.0
0.760	15.45	319.1	18.4
0.822	13.40	204.8	17.1

Kappa = 0.314

Run No. 092669

Cons. = 0.0 $\underline{Q}$ = 0.111 cu.ft./sec.
DHP = 25.20 cm. Visc. = 1.02 cp.

Radius, in.	DHIP, cm.	SPLUS	VPLUS
0.120	40.30	1776.1	24.5
0.245	38.85	1503.1	24.1
0.370	36.50	1230.0	23.3
0.495	33.95	957.0	22.5
0.620	30.60	683.9	21.4
0.745	26.15	410.8	19.8
0.839	20.95	205.5	17.7
0.005	40.95	2027.3	24.7
0.130	40.00	1754.3	24.4
0.255	38.50	1481.2	24.0
0.380	36.20	1208.2	23.2
0.505	33.50	935.1	22.4
0.630	30.00	662.0	21.2
0.755	25.65	389.0	19.6
0.130	40.10	1754.3	24.5

Kappa = 0.312

Run No. 092969

Cons. = 0.041 $\underline{Q}$ = 0.117 cu.ft./sec.
DHP = 26.40 cm. Visc. = 1.01 cp.

Radius, in.	DHIP, cm.	SPLUS	VPLUS
0.005	42.75	2095.6	24.7
0.120	42.55	1835.9	24.6
0.245	41.30	1553.7	24.3
0.370	39.15	1271.4	23.6
0.495	36.20	989.2	22.7
0.620	32.55	706.9	21.5
0.745	28.05	424.7	20.0
0.807	24.75	284.7	18.8
0.130	42.25	1813.3	24.5
0.255	40.85	1531.1	24.1
0.380	38.50	1248.8	23.4
0.505	35.50	966.6	22.5
0.630	31.95	684.3	21.3
0.755	26.95	402.1	19.6
0.817	23.65	262.1	18.4

Kappa = 0.314

Run No. 092969

Cons. = 0.041 Q = 0.198 cu.ft./sec.
DHP = 66.40 cm. Visc. = 1.00 cp.

Radius, in.	DHIP, cm.	SPLUS	VPLUS
0.005	121.90	3356.7	26.3
0.120	121.05	2940.7	26.2
0.245	116.85	2488.6	25.7
0.370	110.60	2036.5	25.0
0.495	103.00	1584.4	24.1
0.620	93.25	1132.3	23.0
0.745	81.65	680.2	21.5
0.807	72.35	456.0	20.2
0.130	121.25	2904.6	26.2
0.255	115.95	2452.5	25.6
0.380	109.35	2000.4	24.9
0.505	101.25	1548.3	23.9
0.630	91.70	1096.2	22.8
0.755	78.70	644.1	21.1
0.817	68.90	419.8	19.8

Kappa = 0.309

Run No. 093069

Cons. = 0.119 Q = 0.067 cu.ft./sec.
DHP = 9.95 cm. Visc. = 0.98 cp.

Radius, in.	DHIP, cm.	SPLUS	VPLUS
0.120	15.52	1161.6	24.2
0.245	14.95	983.0	23.8
0.370	14.05	804.4	23.0
0.495	12.55	625.9	21.8
0.620	11.20	447.3	20.6
0.745	9.20	268.7	18.6
0.005	15.60	1325.9	24.3
0.130	15.40	1147.3	24.1
0.255	14.80	968.7	23.6
0.443	13.20	700.1	22.3
0.568	11.75	521.6	21.1
0.693	10.20	343.0	19.6
0.755	8.95	254.4	18.4
0.817	7.70	165.8	17.1

Kappa = 0.269

Run No. 093069

Cons. = 0.119 Q = 0.114 cu.ft./sec.
DHP = 24.10 cm. Visc. = 0.98 cp.

Radius, in.	DHIP, cm.	SPLUS	VPLUS
0.245	39.35	1529.9	24.8
0.120	40.85	1807.8	25.2
0.370	37.20	1252.0	24.1
0.495	34.15	974.0	23.1
0.620	31.30	696.1	22.1
0.745	26.50	418.2	20.3
0.005	41.35	2063.5	25.4
0.193	40.30	1645.5	25.1
0.318	38.35	1367.6	24.5
0.443	36.00	1089.6	23.7
0.568	32.30	811.7	22.4
0.693	28.40	533.8	21.0
0.817	22.75	258.1	18.8

Kappa = 0.300

Run No. 093069

Cons. = 0.119 Q = 0.205 cu.ft./sec.
DHP = 70.35 cm. Visc. = 1.01 cp.

Radius, in.	DHIP, cm.	SPLUS	VPLUS
0.005	131.30	3420.9	26.5
0.120	129.80	2997.0	26.3
0.245	124.85	2536.2	25.8
0.370	118.30	2075.5	25.1
0.495	110.00	1614.7	24.2
0.620	100.10	1154.0	23.1
0.745	87.60	693.2	21.6
0.318	121.80	2267.2	25.5
0.443	113.40	1806.4	24.6
0.568	104.65	1345.7	23.6
0.693	93.60	884.9	22.4
0.817	76.15	427.8	20.2

Kappa = 0.317

Run No. 100669

Cons. = 0.122 Q = 0.068 cu.ft./sec.
DHP = 9.85 cm. Visc. = 1.00 cp.

Radius, in.	DHIP, cm.	SPLUS	VPLUS
0.005	15.55	1292.8	24.4
0.120	15.43	1132.6	24.3
0.245	14.95	958.5	23.9
0.370	13.95	784.4	23.1
0.495	12.77	610.3	22.1
0.620	11.35	436.1	20.8
0.745	9.40	262.0	18.9
0.193	14.95	1030.9	23.9
0.443	13.00	682.7	22.3
0.693	10.10	334.4	19.6
0.817	7.70	161.7	17.1

Kappa = 0.275

Run No. 100669

Cons. = 0.122 Q = 0.090 cu.ft./sec.
DHP = 16.10 cm. Visc. = 0.98 cp.

Radius, in.	DHIP, cm.	SPLUS	VPLUS
0.005	26.60	1686.6	24.9
0.120	26.30	1477.6	24.8
0.245	25.55	1250.4	24.4
0.370	23.95	1023.3	23.6
0.495	22.00	796.1	22.7
0.620	19.95	569.0	21.6
0.745	17.05	341.8	20.0
0.193	25.65	1344.9	24.5
0.318	24.35	1117.8	23.8
0.443	22.50	890.8	22.9
0.568	20.45	663.5	21.9
0.693	18.00	436.3	20.5
0.817	14.30	210.9	18.3

Kappa = 0.300

Run No. 100669

Cons. = 0.123 $\underline{Q}$ = 0.114 cu.ft./sec.
DHP = 23.70 cm. Visc. = 1.00 cp.

Radius, in.	DHIP, cm.	SPLUS	VPLUS
0.005	41.00	2005.4	25.5
0.120	40.55	1756.9	25.4
0.245	38.90	1486.8	24.8
0.620	30.40	676.5	22.0
0.745	26.60	406.4	20.5
0.318	37.75	1329.1	24.5
0.443	35.00	1059.0	23.6
0.568	32.00	788.9	22.5
0.693	28.35	518.8	21.2
0.817	22.80	250.8	19.0
0.495	33.80	946.6	23.2
0.370	36.75	1216.7	24.1
0.130	40.20	1735.3	25.3

Kappa = 0.307

Run No. 100769

Cons. = 0.185 $\underline{Q}$ = 0.080 cu.ft./sec.
DHP = 12.70 cm. Visc. = 0.99 cp.

Radius, in.	DHIP, cm.	SPLUS	VPLUS
0.630	15.40	484.2	21.4
0.755	12.45	284.5	19.2
0.255	20.90	1083.4	24.9
0.130	21.65	1283.1	25.3
0.005	21.90	1482.8	25.5
0.183	21.45	1198.4	25.2
0.307	20.65	1000.3	24.7
0.443	19.15	783.0	23.8
0.558	17.10	599.3	22.5
0.682	14.75	401.2	20.9
0.745	13.10	300.5	19.7
0.433	19.05	799.0	23.7
0.380	19.45	883.7	24.0
0.505	17.65	684.0	22.9

Kappa = 0.252

Run No. 100769

Cons. = 0.182 Q = 0.114 cu.ft./sec.
DHP = 23.30 cm. Visc. = 0.98 cp.

Radius, in.	DHIP, cm.	SPLUS	VPLUS
0.005	42.00	2029.0	26.0
0.120	41.60	1777.6	25.9
0.245	40.20	1504.8	25.5
0.370	37.90	1231.0	24.7
0.495	34.90	957.7	23.7
0.620	30.70	684.4	22.3
0.745	26.40	411.2	20.6
0.318	38.30	1344.7	24.9
0.433	35.65	1093.3	24.0
0.568	32.40	798.1	22.9
0.693	28.45	524.9	21.4
0.817	22.30	253.8	19.0
0.193	40.70	1618.0	25.6

Kappa = 0.280

Run No. 100769

Cons. = 0.183 Q = 0.174 cu.ft./sec.
DHP = 40.80 cm. Visc. = 0.99 cp.

Radius, in.	DHIP, cm.	SPLUS	VPLUS
0.120	74.35	2328.5	26.2
0.245	71.60	1970.5	25.7
0.370	67.80	1612.5	25.0
0.495	62.90	1254.5	24.1
0.620	56.85	896.6	22.9
0.745	49.30	538.6	21.3
0.005	74.90	2657.8	26.3
0.193	72.35	2119.4	25.8
0.318	68.85	1761.4	25.2
0.443	64.10	1403.5	24.3
0.568	58.50	1045.5	23.2
0.693	51.85	687.5	21.9
0.817	41.75	332.4	19.6

Kappa = 0.300

Run No. 100869

Cons. = 0.184 $\underline{Q}$ = 0.192 cu.ft./sec.
DHP = 61.65 cm. Visc. = 0.99 cp.

Radius, in.	DHIP, cm.	SPLUS	VPLUS
0.120	113.50	2862.2	26.3
0.245	110.30	2422.2	25.9
0.370	104.20	1982.2	25.2
0.495	97.60	1542.1	24.4
0.620	88.80	1102.1	23.3
0.745	77.60	662.1	21.8
0.193	110.90	2605.3	26.0
0.318	105.90	2165.2	25.4
0.568	90.80	1285.2	23.5
0.693	80.95	845.1	22.2
0.817	65.55	408.6	20.0
0.005	114.35	3267.1	26.4
0.432	101.55	1763.9	24.9

Kappa = 0.312

Run No. 101069

Cons. = 0.254 $\underline{Q}$ = 0.114 cu.ft./sec.
DHP - 22.30 cm. Visc. = 0.98 cp.

Radius, in.	DHIP, cm.	SPLUS	VPLUS
0.005	42.10	1985.0	26.6
0.120	42.00	1739.0	26.6
0.370	39.80	1204.3	25.9
0.495	35.95	936.9	24.6
0.620	31.65	669.6	23.1
0.745	26.35	402.2	21.1
0.433	36.90	1069.6	24.9
0.568	33.05	780.8	23.6
0.693	27.93	513.5	21.7
0.755	24.70	380.9	20.4
0.130	42.00	1717.6	26.6
0.245	41.70	1471.7	26.5
0.255	41.30	1450.3	26.4

Kappa = 0.250

Run No. 101069

Cons. = 0.254 Q = 0.195 cu.ft./sec.
DHP = 61.75 cm. Visc. = 0.98 cp.

Radius, in.	DHIP, cm.	SPLUS	VPLUS
0.443	104.90	1744.2	25.3
0.568	95.50	1299.3	24.1
0.698	85.40	854.4	22.8
0.755	78.30	633.8	21.8
0.193	116.70	2634.0	26.9
0.120	121.20	2893.8	27.2
0.370	110.95	2004.0	26.0
0.495	103.30	1559.1	25.1
0.620	92.00	1114.2	23.7
0.745	80.00	669.4	22.1
0.817	71.10	413.1	20.8
0.005	122.10	3303.1	27.3

Kappa = 0.299

Run No. 101469

Cons. = 0.354 Q = 0.114 cu.ft./sec.
DHP = 21.30 cm. Visc. = 1.01 cp.

Radius, in.	DHIP, cm.	SPLUS	VPLUS
0.380	38.05	1121.7	25.9
0.255	39.00	1375.3	26.2
0.505	35.60	868.2	25.1
0.630	30.90	614.7	23.4
0.724	26.60	424.0	21.7
0.786	22.70	298.3	20.0
0.370	38.85	1142.0	26.2
0.245	39.70	1395.6	26.5
0.495	36.75	888.5	25.5
0.620	32.45	635.0	23.9
0.682	29.45	509.2	22.8
0.776	23.90	318.6	20.5
0.745	76.00	381.4	21.4

Kappa = 0.238

Run No. 122268

Cons. = 0.356 $\underline{Q}$ = 0.113 cu.ft./sec.
DHP = 21.60 cm. Visc. = 1.04 cp.

Radius, in.	DHIP, cm.	SPLUS	VPLUS
0.020	39.60	1811.1	26.3
0.105	39.65	1642.5	26.3
0.230	39.40	1394.6	26.2
0.355	38.70	1146.6	26.0
0.480	36.40	898.7	25.2
0.605	32.15	650.7	23.7
0.668	29.40	525.8	22.6
0.730	25.85	402.8	21.2
0.855	17.50	154.9	17.5
0.020	39.90	1811.1	26.4
0.145	39.80	1563.2	26.3
0.270	39.35	1315.2	26.2
0.395	37.90	1067.3	25.7
0.520	34.85	819.3	24.6
0.645	29.90	571.4	22.8
0.708	26.80	446.4	21.6
0.801	21.20	262.0	19.2

Kappa = 0.263

Run No. 122269

Cons. = 0.356 $\underline{Q}$ = 0.194 cu.ft./sec.
DHP = 57.15 cm. Visc. = 0.98 cp.

Radius, in.	DHIP, cm.	SPLUS	VPLUS
0.395	105.70	1842.3	26.4
0.520	96.80	1414.3	25.2
0.645	86.50	986.3	23.9
0.708	79.90	770.6	22.9
0.270	112.45	2270.3	27.2
0.145	117.60	2698.3	27.8
0.020	119.45	3126.3	28.0
0.105	118.65	2835.3	27.8
0.230	115.60	2407.3	27.6
0.355	109.70	1979.3	26.9
0.480	101.30	1551.3	25.8
0.605	91.50	1123.3	24.5
0.668	84.85	907.6	23.6
0.730	78.40	695.3	22.7
0.605	91.40	1123.3	24.5

Kappa = 0.263

Run No. 101469

Cons. = 0.354 Q = 0.194 cu.ft./sec.
DHP = 57.40 cm. Visc. = 1.00 cp.

Radius, in.	DHIP, cm.	SPLUS	VPLUS
0.370	109.55	1893.5	26.8
0.495	101.30	1473.1	25.8
0.620	91.10	1052.8	24.4
0.745	78.20	632.4	22.6
0.068	119.95	2909.1	28.0
0.120	119.80	2734.2	28.0
0.495	101.00	1473.1	25.7
0.193	115.40	2488.7	27.5
0.443	103.30	1648.0	26.0
0.568	94.00	1227.7	24.8
0.693	82.10	807.3	23.2
0.755	75.00	598.8	22.2
0.068	120.00	2909.1	28.0
0.120	119.30	2734.2	28.0
0.245	115.95	2313.8	27.6
0.370	109.50	1893.5	26.8

Kappa = 0.266

Run No. 101769

Cons. = 0.473 Q = 0.198 cu.ft./sec.
DHP = 55.70 cm. Visc. = 0.98 cp.

Radius, in.	DHIP, cm.	SPLUS	VPLUS
0.495	92.60	1480.8	25.0
0.620	84.45	1058.3	23.9
0.682	78.65	848.7	23.0
0.745	70.90	635.7	21.9
0.120	104.30	2748.4	26.5
0.568	87.65	1234.0	24.3
0.693	78.00	811.5	22.9
0.755	69.80	601.9	21.7
0.443	95.90	1656.6	25.4
0.318	100.80	2079.1	26.1
0.193	104.00	2501.6	26.3
0.370	98.40	1903.3	25.8
0.245	103.20	2325.8	26.4

Kappa = 0.302

Run No. 122369

Cons. = 0.467 Q = 0.118 cu.ft./sec.
DHP = 21.70 cm. Visc. = 0.99 cp.

Radius, in.	DHIP, cm.	SPLUS	VPLUS
0.355	39.35	1207.3	26.1
0.480	38.15	946.3	25.7
0.480	38.40	946.3	25.8
0.605	35.35	685.2	24.7
0.668	32.70	553.6	23.8
0.730	28.35	424.1	22.2
0.230	40.00	1468.4	26.3
0.105	40.20	1729.4	26.4
0.020	40.30	1907.0	26.4
0.270	40.05	1384.8	26.3
0.520	37.45	862.7	25.5
0.645	32.70	601.6	23.8
0.395	39.55	1123.8	26.2

Kappa = 0.371

Run No. 122369

Cons. = 0.467 Q = 0.195 cu.ft./sec.
DHP = 56.20 cm. Visc. = 0.99 cp.

Radius, in.	DHIP, cm.	SPLUS	VPLUS
0.395	107.30	1808.5	26.8
0.270	112.55	2228.6	27.4
0.145	115.80	2648.8	27.8
0.020	117.35	3068.9	28.0
0.105	116.35	2783.2	27.9
0.230	114.35	2363.1	27.7
0.355	110.75	1942.9	27.2
0.480	102.20	1522.8	26.1
0.605	94.05	1102.7	25.1
0.668	87.80	890.9	24.2
0.730	80.90	682.5	23.3
0.355	110.85	1942.9	27.2
0.105	116.25	2783.2	27.9
0.020	117.10	3068.9	28.0
0.395	107.40	1808.5	26.8
0.520	98.90	1388.4	25.7
0.645	86.85	968.2	24.1
0.739	77.65	652.3	22.8

Kappa = 0.294

Run No. 101769

Cons. = 0.473 $\underline{Q}$ = 0.220 cu.ft./sec.
DHP = 69.00 cm. Visc. = 0.98 cp.

Radius, in.	DHIP, cm.	SPLUS	VPLUS
0.620	95.70	1177.8	22.8
0.745	86.00	707.6	21.6
0.495	103.60	1648.1	23.8
0.370	111.90	2118.4	24.7
0.005	121.60	3691.6	25.7
0.120	120.70	3058.9	25.6
0.245	118.00	2588.7	25.4
0.370	112.60	2118.4	24.6
0.193	118.90	2784.3	25.5
0.443	109.00	1843.8	24.4
0.693	92.90	903.2	22.5

Kappa = 0.370

Run No. 121969

Cons. = 0.0 $\underline{Q}$ = 0.112 cu.ft./sec.
DHP = 24.40 cm. Visc. = 1.00 cp.

Radius, in.	DHIP, cm.	SPLUS	VPLUS
0.020	40.30	2001.9	24.9
0.105	39.85	1815.5	24.8
0.230	38.45	1541.5	24.3
0.355	36.20	1267.4	23.6
0.480	33.70	993.4	22.8
0.605	30.20	719.3	21.6
0.730	25.90	445.2	20.0
0.793	23.00	307.1	18.8
0.855	18.90	171.2	17.1
0.020	40.10	2001.9	24.9
0.145	39.30	1727.8	24.6
0.145	39.20	1727.8	24.6
0.270	37.50	1453.8	24.0
0.395	35.20	1179.7	23.3
0.520	32.35	905.7	22.3
0.645	28.90	631.6	21.1
0.770	24.25	357.5	19.3
0.848	20.35	186.5	17.7

Kappa = 0.310

APPENDIX III

CONSISTENCY PROFILE DATA

The consistency profile data are tabulated below. These data were measured in the 1.865-in. i.d. pipe loop at 20°C. The average consistency, Cons., and the flow rate, Q, are given for each profile. The positions are reported as read from the scale on the traversing assembly. The pipe center line is given for each profile. Consistencies at each position are in g./100 ml.

Run No. 068122

Cons. = 0.122 g./100 ml. $\underline{Q}$ = 0.068 cu.ft./sec.

Position, in.	Cons., g./100 ml.
3.250	0.088
2.500	0.192
2.375	0.188
2.250	0.183
2.125	0.166
2.000	0.139
1.875	0.122
1.750	0.096
2.000	0.142
2.125	0.163
2.250	0.180
2.375	0.188
2.500	0.192
2.625	0.183
2.750	0.171
2.875	0.154
3.000	0.134
3.125	0.113
3.000	0.134
2.750	0.171
2.625	0.186
2.500	0.190

Center line = 2.480 in.

Run No. 090122

Cons. = 0.122 g./100 ml. $\underline{Q}$ = 0.090 cu.ft./sec.

Position, in.	Cons., g./100 ml.
3.250	0.102
2.500	0.171
2.375	0.168
2.250	0.162
2.125	0.154
2.000	0.142
1.875	0.130
1.750	0.111
2.000	0.145
2.125	0.154
2.250	0.162
2.375	0.168
2.500	0.168
2.625	0.168
2.750	0.157
2.875	0.148
3.000	0.136
3.125	0.125
2.875	0.148
2.500	0.168

Center line = 2.480 in.

Run No. 114122

Cons. = 0.122 g./100 ml. $\underline{Q}$ = 0.114 cu.ft./sec.

Position, in.	Cons., g./100 ml.
3.250	0.111
2.375	0.160
2.250	0.157
2.125	0.151
2.000	0.142
1.875	0.133
1.750	0.116
1.873	0.134
1.812	0.125
2.125	0.151
2.500	0.162
2.625	0.158
2.750	0.152
2.875	0.145
3.000	0.136
3.125	0.125
3.188	0.119
3.000	0.139
3.125	0.127
2.875	0.146
2.500	0.162

Center line = 2.480 in.

Run No. 205122

Cons. = 0.122 g./100 ml. $\underline{Q}$ = 0.205 cu.ft./sec.

Position, in.	Cons., g./100 ml.
3.250	0.121
2.375	0.151
2.250	0.148
2.125	0.144
2.000	0.139
1.875	0.134
1.812	0.130
1.750	0.125
2.000	0.140
2.125	0.144
2.250	0.148
2.625	0.150
2.750	0.146
2.875	0.142
3.000	0.139
3.125	0.132
3.188	0.128
3.125	0.133
2.875	0.143
2.625	0.150
2.500	0.151

Center line = 2.480 in.

Run No. 068178

Cons. = 0.178 g./100 ml. $\underline{Q}$ = 0.068 cu.ft./sec.

Position, in.	Cons., g./100 ml.
3.230	0.106
2.625	0.300
2.375	0.305
2.250	0.290
2.125	0.249
2.000	0.206
1.875	0.162
1.812	0.139
1.750	0.114
2.125	0.249
2.375	0.302
2.625	0.300
2.750	0.272
2.875	0.228
3.000	0.184
3.125	0.148
2.500	0.308

Center line = 2.480 in.

Run No. 114178

Cons. = 0.178 g./100 ml. $\underline{Q}$ = 0.114 cu.ft./sec.

Position, in.	Cons., g./100 ml.
3.250	0.148
2.500	0.246
2.375	0.242
2.250	0.236
2.125	0.222
2.125	0.219
2.000	0.206
1.875	0.192
1.812	0.177
1.750	0.159
2.125	0.222
2.375	0.238
2.375	0.242
2.500	0.246
2.625	0.238
2.750	0.226
2.750	0.228
2.875	0.212
3.000	0.199
3.125	0.183
3.188	0.168
3.250	0.151
3.000	0.201
2.750	0.228
2.500	0.246

Center line = 2.480 in.

Run No. 174178

Cons. = 0.178 g./100 ml. $\underline{Q}$ = 0.174 cu.ft./sec.

Position, in.	Cons., g./100 ml.
3.250	0.166
2.375	0.236
2.250	0.228
2.125	0.222
2.000	0.212
1.875	0.200
1.812	0.192
1.750	0.180
2.125	0.219
2.250	0.226
2.375	0.230
2.500	0.231
2.625	0.227
2.750	0.222
2.875	0.213
3.000	0.201
3.125	0.189
2.500	0.236

Center line = 2.480 in.

Run No. 192178

Cons. = 0.178 g./100 ml. $\underline{Q}$ = 0.192 cu.ft./sec.

Position, in.	Cons., g./100 ml.
3.250	0.170
3.000	0.208
3.125	0.196
3.188	0.188
3.000	0.210
2.875	0.219
2.750	0.226
2.625	0.231
2.500	0.231
2.250	0.226
2.125	0.219
2.000	0.212
1.875	0.199
1.812	0.191
1.750	0.180
2.500	0.231

Center line = 2.480 in.

Run No. 114243

Cons. = 0.243 g./100 ml. $\underline{Q}$ = 0.114 cu.ft./sec.

Position, in.	Cons., g./100 ml.
3.250	0.178
2.250	0.402
2.125	0.351
2.000	0.295
1.875	0.245
1.750	0.189
2.375	0.430
2.375	0.423
2.625	0.423
2.750	0.376
2.875	0.327
3.000	0.272
3.125	0.227
3.000	0.272
2.500	0.430

Center line = 2.480 in.

Run No. 196243

Cons. = 0.243 g./100 ml. $\underline{Q}$ = 0.196 cu.ft./sec.

Position, in.	Cons., g./100 ml.
3.250	0.227
2.500	0.332
2.375	0.332
2.250	0.320
2.125	0.308
2.000	0.296
1.875	0.276
1.812	0.260
1.750	0.237
2.000	0.296
2.250	0.320
2.500	0.326
2.750	0.315
2.875	0.301
3.000	0.288
3.125	0.266
3.188	0.249
2.625	0.320
2.500	0.326

Center line = 2.480 in.

Run No. 114360

Cons. = 0.360 g./100 ml. $\underline{Q}$ = 0.114 cu.ft./sec.

Position, in.	Cons., g./100 ml.
3.250	0.205
2.375	0.587
2.375	0.596
2.250	0.579
2.000	0.445
1.875	0.332
1.812	0.278
1.750	0.227
2.000	0.430
2.500	0.596
2.625	0.587
2.750	0.555
3.000	0.376
3.125	0.284
3.125	0.290
3.188	0.245
3.000	0.383
2.875	0.480
2.750	0.547
2.625	0.579
2.500	0.596
2.000	0.423
1.750	0.221
2.875	0.480
2.125	0.532
2.250	0.579
2.250	0.570
2.500	0.611

Center line = 2.480 in.

Run No. 193360

Cons. = 0.360 g./100 ml. $\underline{Q}$ = 0.193 cu.ft./sec.

Position, in.	Cons., g./100 ml.
3.250	0.290
2.000	0.402
2.250	0.465
2.625	0.465
2.750	0.445
2.875	0.416
3.000	0.390
3.125	0.357
3.188	0.329
3.000	0.392
2.750	0.445
2.500	0.473
2.375	0.465
2.250	0.458
2.125	0.437
2.000	0.409
1.875	0.383
1.812	0.357
1.750	0.326
2.500	0.480

Center line = 2.480 in.

Run No. 117460

Cons. = 0.460 g./100 ml. $\underline{Q}$ = 0.117 cu.ft./sec.

Position, in.	Cons., g./100 ml.
1.750	0.295
2.375	0.817
2.250	0.804
2.125	0.755
2.000	0.647
1.875	0.465
1.875	0.473
1.812	0.370
1.750	0.290
2.000	0.638
2.000	0.647
2.250	0.804
2.375	0.817
2.625	0.817
2.750	0.778
2.750	0.790
2.875	0.693
3.000	0.563
3.125	0.396
3.188	0.320
3.188	0.326
3.125	0.396
3.000	0.563
2.000	0.647
2.500	0.828

Center line = 2.480 in.

Run No. 195460

Cons. = 0.460 g./100 ml. $\underline{Q}$ = 0.195 cu.ft./sec.

Position, in.	Cons., g./100 ml.
3.250	0.366
2.500	0.704
2.375	0.704
2.250	0.680
2.125	0.611
2.000	0.555
1.875	0.487
1.875	0.495
1.812	0.451
1.750	0.402
2.000	0.555
2.250	0.680
2.500	0.714
2.500	0.708
2.625	0.680
2.750	0.626
2.875	0.570
3.000	0.510
3.125	0.452
3.125	0.459
3.188	0.417
3.125	0.459
2.750	0.626
3.000	0.516
2.500	0.708

Center line = 2.480 in.